

University of Louisville

ThinkIR: The University of Louisville's Institutional Repository

Electronic Theses and Dissertations

5-2018

Comparing stenotic blood flow in three- and two-dimensional arterial renderings using computational fluid dynamics and multiphase mean age theory.

Jacob S. Garza
University of Louisville

Follow this and additional works at: <https://ir.library.louisville.edu/etd>



Part of the [Biochemical and Biomolecular Engineering Commons](#), and the [Other Chemical Engineering Commons](#)

Recommended Citation

Garza, Jacob S., "Comparing stenotic blood flow in three- and two-dimensional arterial renderings using computational fluid dynamics and multiphase mean age theory." (2018). *Electronic Theses and Dissertations*. Paper 2888.
<https://doi.org/10.18297/etd/2888>

This Master's Thesis is brought to you for free and open access by ThinkIR: The University of Louisville's Institutional Repository. It has been accepted for inclusion in Electronic Theses and Dissertations by an authorized administrator of ThinkIR: The University of Louisville's Institutional Repository. This title appears here courtesy of the author, who has retained all other copyrights. For more information, please contact thinkir@louisville.edu.

COMPARING STENOTIC BLOOD FLOW IN THREE- AND TWO-DIMENSIONAL
ARTERIAL RENDERINGS USING COMPUTATIONAL FLUID DYNAMICS AND
MULTIPHASE MEAN AGE THEORY

By

Jacob S. Garza
B.S., University of Louisville, 2017

A Thesis
Submitted to the Faculty of the
University of Louisville
J. B. Speed School of Engineering
as Partial Fulfillment of the Requirements
for the Professional Degree

MASTER OF ENGINEERING

Department of Chemical Engineering

May 2018

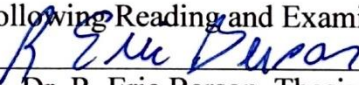
COMPARING STENOTIC BLOOD FLOW IN THREE- AND TWO-DIMENSIONAL
ARTERIAL RENDERINGS USING COMPUTATIONAL FLUID DYNAMICS AND
MULTIPHASE MEAN AGE THEORY


Submitted by: 
Jacob S. Garza

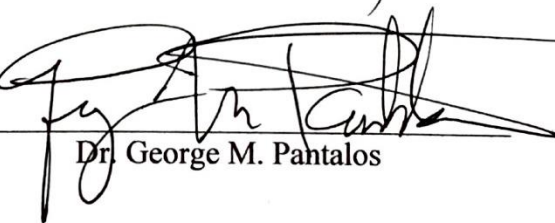
A Thesis Approved On

4/23/18
(Date)

by the Following Reading and Examination Committee:


Dr. R. Eric Berson, Thesis Director


Dr. Gerold A. Willing


Dr. George M. Pantalos

ACKNOWLEDGEMENTS

I have to thank Dr. Berson for his constant guidance and assistance through all of this.

I have to also thank Javad, Dr. Shahab, and Elmira for making most of this work possible. Our weekly meetings were always beneficial. I have to thank Dr. Willing for reviewing my writing and teaching me so much over the years. With this, I would like to also thank the other faculty members of the department for greatly furthering my education. Also, Dr. Pantalos gets a massive thank you for stepping in on such short notice to help as a member of the committee.

Lastly, my family and friends deserve special attention and recognition for supporting me, encouraging me, and improving me throughout this voyage. They ensured there was nothing to fear and nothing to doubt.

TABLE OF CONTENTS

	<u>Page</u>
APPROVAL PAGE	ii
ACKNOWLEDGEMENTS	iii
ABSTRACT	vi
NOMENCLATURE	viii
LIST OF TABLES	ix
LIST OF FIGURES	x
I. INTRODUCTION	1
II. LITERATURE REVIEW	4
A. Coronary Artery Disease (CAD)	4
1. General Information: Pathophysiology and Epidemiology	4
2. Current State of Diagnosis	6
B. Fractional Flow Reserve (<i>FFR</i>) in Angiography	9
1. Definition	9
2. Use in ICA and the Extension to Coronary CTA	11
3. Clinical Comparison of <i>FFR</i> and <i>FFR_{CT}</i>	13
C. Computational Fluid Dynamics (CFD)	15
1. General Information: Conservation and Discretization	15
2. Utilization in Multiphase Systems	20
D. Age Topics	21
1. Residence Time Distributions (RTDs) and Mean Age Theory	21
2. Deriving Mean Age Conservation and the Extension to Multiphase Systems	23
III. EXPERIMENTAL METHODS	28
A. Preliminaries	28
1. Purpose	28
2. Plan	28
B. Materials	29
C. Procedures for Processing Two Orthogonal Arterial Slices	30
1. Geometry Generation	30
2. Mesh Generation	44
3. Fluent Case Processing	51
IV. RESULTS AND DISCUSSION	69
A. Scope of Investigated Patient Numbers, Source Renderings, and Created Slices	69
B. Fluent Results of the Three-Dimensional Source Renderings	80
C. Fluent Results of the Two-Dimensional Arterial Slices	85
1. Plots of Scalar0 Mean Age and Nominal Mean Residence Time Comparison	85
2. Plots of Velocity Contours	91
D. Three- and Two-Dimensional Comparison of Mean Age	97

TABLE OF CONTENTS (CONT.)

	<u>Page</u>
V. CONCLUSIONS	105
VI. RECOMMENDATIONS	108
REFERENCES CITED.....	110
APPENDIX I. SAMPLE SOURCE CODE FOR A UDF FILE	113
APPENDIX II. PLOTS OF SCALAR1 MEAN AGE	115
VITA.....	119

ABSTRACT

Over one million invasive coronary angiography procedures are performed annually in patients who experience chest pain or are known to have coronary artery disease. The procedure is carried out to ascertain the degree of arterial blockage (stenosis) that hinders blood flow to the heart. A cardiologist performing the procedure determines the physiological degree of a stenosis by either visual estimation, which is routine practice, or by invasively measuring fractional flow reserve (*FFR*), which is the current gold standard that has been demonstrated to improve patient outcomes and temper the cost of healthcare. Nevertheless, *FFR* is performed in only 10–20% of patients because it is invasive, expensive, and requires more radiation exposure.

New computational methods utilizing three-dimensional renderings processed from coronary angiograms can provide an accurate, highly sensitive, non-invasive method to assess stenotic significance without using *FFR*. While beneficial, this technique requires intensive computer processing power and calculation runtimes on the order of several hours. An approach to reduce computational time involves alike computing of two-dimensional arterial slices cut from the three-dimensional source renderings.

The main objective was to determine if two-dimensional processing can also provide an accurate and highly sensitive method to assess stenotic significance at a fraction of the computational expense. Blood flow was analyzed in five patient cases below and five patient cases above the commonly accepted *FFR* threshold value for intervention of 0.80. Following the generation of two orthogonal slices from DICOM-derived three-dimensional renderings, pulsing blood flow was simulated with CFD, and

multiphase mean age theory was applied to calculate the mean age of red blood cells as a diagnostic metric.

Two-dimensional processing typically exhibited a correlation with *FFR* only in the geometries of vertically-oriented slices. This was ascribed to the possibility of uncaptured stenotic blood flow characteristics in the limited testing of only two angles of a full arterial segment. Mean ages for the three-dimensional cases were many orders of magnitude higher than those of the corresponding two-dimensional cases. This was attributed to red blood cell collisions and distal recirculatory eddies near a stenosis being less expressed in the simplicity of the two-dimensional slices when compared to the complexity of the three-dimensional source renderings.

A mean age threshold for determining stent intervention was estimated for the two-dimensional cases since limited sample size disallowed rigorous statistical analysis. The data suggested an arbitrary value equal to ~ 2.5 . Nine out of ten cases correlated with *FFR*, with just one false negative diagnosis. In published virtual *FFR* techniques, false diagnosis typically occurs in 10–13% of the cases.

Computational runtime for two-dimensional cases was less than 2% of the runtime for corresponding three-dimensional cases. Preliminary results indicate two-dimensional processing may efficiently detect and assess stenoses non-invasively, provided that it holds up to rigorous statistical analysis following testing of at least 80–100 more cases, plus several additional slice angles.

NOMENCLATURE

a	=	mean age
a_i, a_1, a_3	=	components $i, 1,$ and 3 of an imparting velocity vector
b_j, b_2, b_4	=	components $j, 2,$ and 4 of an imparting velocity vector
C	=	concentration of a passive scalar
$C(x, t)$	=	concentration of a passive scalar at a location x and time t
CFR	=	coronary flow reserve
C_{out}	=	flow-weighted average concentration across the exit plane
D	=	molecular diffusivity
D_e	=	effective turbulent diffusivity
FFR	=	fractional flow reserve
FFR_{CT}	=	fractional flow reserve derived from coronary CTA
\vec{g}	=	gravitational force per unit mass vector
\hat{i}	=	unit vector in the direction of i
\hat{j}	=	unit vector in the direction of j
\hat{n}	=	normal outward vector at the surface
p	=	pressure
p_a	=	pressure of an artery proximal to a stenosis
p_d	=	pressure of an artery distal to a stenosis
p_{outlet}	=	outlet pressure
p_v	=	pressure of associated vein
R	=	resistance
S	=	surface of a control volume
S_m	=	source mass added to the continuous phase from the dispersed second phase (or any user-defined sources)
t	=	time
\bar{t}	=	mean residence time
u	=	general dependent variable
u_i	=	discretized analog of u with values of i
u_{i-1}	=	previous term of the discretized analog of u with values of i dictated by a Taylor series expansion
\vec{v}	=	total velocity vector
v_{inlet}	=	inlet velocity
x	=	general independent variable
x_i	=	grid points with values of i
x_n	=	normal coordinate in the direction of flow
y	=	general independent variable
$\alpha(x, t)$	=	phasic volume fraction of an individual phase at a location x and time t
δ	=	unit tensor
μ	=	viscosity
ρ	=	density
τ	=	shear stress
$\varphi(x, t)$	=	passive scalar value at a location x and time t

LIST OF TABLES

		<u>Page</u>
TABLE 2.1 -	A COMPARISON OF TESTS USED FOR CAD DIAGNOSIS	8
TABLE 2.2 -	STUDIES COMPARING FFR_{CT} DIAGNOSTIC PERFORMANCE USING FFR AS THE REFERENCE STANDARD.....	14
TABLE 4.1 -	VALUES OF FFR AND COMPONENTS OF THE ARTERIAL TREE REPRESENTING THE PATIENT NUMBERS USED IN THIS INVESTIGATION.....	69
TABLE 4.2 -	A COMPARISON OF NOMINAL MEAN RESIDENCE TIMES AND MEAN AGE VALUES FOR THE TWO-DIMENSIONAL ARTERIAL SLICES	90
TABLE 4.3 -	A COMPARISON OF MEAN AGE VALUES FOR THE THREE- DIMENSIONAL SOURCE RENDERINGS AND THE TWO- DIMENSIONAL ARTERIAL SLICES.....	98
TABLE 4.4 -	TABULATION OF THE NUMBER OF OCCURRENCES OF PROPER DIAGNOSIS, FALSE POSITIVES, AND FALSE NEGATIVES OBSERVED IN THE QUADRANT PLOTS CORRELATING THE MEAN AGE OF RED BLOOD CELLS AND FFR	103

LIST OF FIGURES

	<u>Page</u>
FIGURE 2.1 - Iterative Schemes for the (a) Pressure-based and (b) Density-based Solvers.....	19
FIGURE 3.1 - STL File Opening Settings in SpaceClaim	31
FIGURE 3.2 - Line Options in SpaceClaim	32
FIGURE 3.3 - Major Axes Displayed on a Boundary Face in SpaceClaim	32
FIGURE 3.4 - Two Orthogonal Lines Extending Beyond a Boundary Face in SpaceClaim	33
FIGURE 3.5 - Two Orthogonal Lines Reduced to the Extent of a Boundary Face in SpaceClaim	33
FIGURE 3.6 - Line Name Distribution in SpaceClaim	34
FIGURE 3.7 - Initial Spline Creation in SpaceClaim.....	35
FIGURE 3.8 - Completed Spline (in Red) in SpaceClaim	35
FIGURE 3.9 - Spline Name Distribution in SpaceClaim	36
FIGURE 3.10 - Structure Pane (a) Before and (b) After Deletion of Slice 2 Components in SpaceClaim	37
FIGURE 3.11 - Components of Geometry Outlining Slice 1 After Deletion of Slice 2 Components in SpaceClaim	38
FIGURE 3.12 - Save As Window and Options for STEP File Creation in SpaceClaim	38
FIGURE 3.13 - Fill Surface Pane Magnified and the Three-Dimensional Outline Being Filled in SolidWorks	40
FIGURE 3.14 - Flatten Pane Magnified and the Three-Dimensional Surface Being Flattened in SolidWorks	41
FIGURE 3.15 - Move/Copy Body Pane Magnified and the Two-Dimensional Surface Being Aligned in SolidWorks.....	42
FIGURE 3.16 - Delete/Keep Body... Pane Magnified and the Three-Dimensional Surface Being Deleted in SolidWorks	43
FIGURE 3.17 - Project Schematic Pane with Geometry and Fluid Flow (Fluent) Modules in Workbench.....	44
FIGURE 3.18 - Details of “Mesh” Pane Preferences in Meshing.....	45
FIGURE 3.19 - Insert Controls in Meshing.....	46
FIGURE 3.20 - Details of “Body Sizing” - Sizing Pane in Meshing	46
FIGURE 3.21 - Details of “Inflation” - Inflation Pane in Meshing.....	47
FIGURE 3.22 - Creating a Named Selection for the Inlet in Meshing.....	48
FIGURE 3.23 - Named Selection Distribution in Meshing.....	49
FIGURE 3.24 - Checking Mesh Count in the Details of “Mesh” Pane in Meshing.....	50
FIGURE 3.25 - Fluent Launcher Window in Workbench.....	51
FIGURE 3.26 - General Pane in Fluent.....	52
FIGURE 3.27 - Multiphase Model Window in Fluent.....	52
FIGURE 3.28 - Create/Edit Materials Window for Plasma in Fluent.....	53
FIGURE 3.29 - User-Defined Functions Window with car_yas_visc Viscosity Selection for Red Blood Cells in Fluent	54
FIGURE 3.30 - Phases Window in Fluent.....	54

LIST OF FIGURES (CONT.)

	<u>Page</u>
FIGURE 3.31 - Secondary Phase Window in (a) General and with the (b) Granular Properties Magnified in Fluent	55
FIGURE 3.32 - Phase Interaction Window in (a) General and with the (b) Drag Coefficient Settings Magnified in Fluent.....	56
FIGURE 3.33 - Interpreted UDFs Window in Fluent	56
FIGURE 3.34 - User-Defined Scalars Window for (a) Red Blood Cells and (b) Plasma in Fluent.....	57
FIGURE 3.35 - Updated Create/Edit Materials Window for Scalar0 in Fluent.....	58
FIGURE 3.36 - UDS Diffusion Coefficients Window for Scalar0 in Fluent.....	58
FIGURE 3.37 - Fluid and User Scalar 0 Sources Windows for Scalar0 in Fluent.....	59
FIGURE 3.38 - Velocity Inlet Window for Scalar0 Displaying (a) Momentum, (b) Multiphase, and (c) UDS Settings in Fluent	60
FIGURE 3.39 - Pressure Outlet Window for Scalar0 Displaying (a) Multiphase and (b) UDS Settings in Fluent.....	61
FIGURE 3.40 - Updated Create/Edit Materials Window for Scalar1 in Fluent.....	62
FIGURE 3.41 - UDS Diffusion Coefficients Window for Scalar1 in Fluent.....	62
FIGURE 3.42 - Fluid and User Scalar 1 Sources Windows for Scalar1 in Fluent.....	62
FIGURE 3.43 - Velocity Inlet Window for Scalar1 Displaying (a) Momentum and (b) UDS Settings in Fluent.....	63
FIGURE 3.44 - Pressure Outlet Window for Scalar1 Displaying UDS Settings in Fluent	63
FIGURE 3.45 - Solution Methods Pane in Fluent.....	64
FIGURE 3.46 - Solution Controls Pane in (a) General and with the (b) Under-Relaxation Factors Magnified in Fluent	65
FIGURE 3.47 - Residual Monitors Window in (a) General and with the (b) Equations Magnified in Fluent.....	66
FIGURE 3.48 - Solution Initialization Pane in (a) General and with the (b) Initial Values Magnified in Fluent	67
FIGURE 3.49 - Run Calculation Pane in Fluent	68
FIGURE 4.1 - Depictions of the (a) Three-Dimensional Source Rendering and Two-Dimensional (b) Slice 1 and (c) Slice 2 for the Artery of Patient 004	70
FIGURE 4.2 - Depictions of the (a) Three-Dimensional Source Rendering and Two-Dimensional (b) Slice 1 and (c) Slice 2 for the Artery of Patient 005	71
FIGURE 4.3 - Depictions of the (a) Three-Dimensional Source Rendering and Two-Dimensional (b) Slice 1 and (c) Slice 2 for the Artery of Patient 017	72
FIGURE 4.4 - Depictions of the (a) Three-Dimensional Source Rendering and Two-Dimensional (b) Slice 1 and (c) Slice 2 for the Artery of Patient 019	73

LIST OF FIGURES (CONT.)

	<u>Page</u>
FIGURE 4.5 - Depictions of the (a) Three-Dimensional Source Rendering and Two-Dimensional (b) Slice 1 and (c) Slice 2 for the Artery of Patient 041	74
FIGURE 4.6 - Depictions of the (a) Three-Dimensional Source Rendering and Two-Dimensional (b) Slice 1 and (c) Slice 2 for the Artery of Patient 045	75
FIGURE 4.7 - Depictions of the (a) Three-Dimensional Source Rendering and Two-Dimensional (b) Slice 1 and (c) Slice 2 for the Artery of Patient 046	76
FIGURE 4.8 - Depictions of the (a) Three-Dimensional Source Rendering and Two-Dimensional (b) Slice 1 and (c) Slice 2 for the Artery of Patient 058	77
FIGURE 4.9 - Depictions of the (a) Three-Dimensional Source Rendering and Two-Dimensional (b) Slice 1 and (c) Slice 2 for the Artery of Patient 061	78
FIGURE 4.10 - Depictions of the (a) Three-Dimensional Source Rendering and Two-Dimensional (b) Slice 1 and (c) Slice 2 for the Artery of Patient 075	79
FIGURE 4.11 - Area-Weighted Average of Scalar0 for the Three-Dimensional Source Rendering of Patient 004	81
FIGURE 4.12 - Area-Weighted Average of Scalar0 for the Three-Dimensional Source Rendering of Patient 005	81
FIGURE 4.13 - Area-Weighted Average of Scalar0 for the Three-Dimensional Source Rendering of Patient 017	81
FIGURE 4.14 - Area-Weighted Average of Scalar0 for the Three-Dimensional Source Rendering of Patient 019	82
FIGURE 4.15 - Area-Weighted Average of Scalar0 for the Three-Dimensional Source Rendering of Patient 041	82
FIGURE 4.16 - Area-Weighted Average of Scalar0 for the Three-Dimensional Source Rendering of Patient 045	83
FIGURE 4.17 - Area-Weighted Average of Scalar0 for the Three-Dimensional Source Rendering of Patient 046	83
FIGURE 4.18 - Area-Weighted Average of Scalar0 for the Three-Dimensional Source Rendering of Patient 058	83
FIGURE 4.19 - Area-Weighted Average of Scalar0 for the Three-Dimensional Source Rendering of Patient 061	84
FIGURE 4.20 - Area-Weighted Average of Scalar0 for the Three-Dimensional Source Rendering of Patient 075	84
FIGURE 4.21 - Area-Weighted Average of Scalar0 for (a) Slice 1 and (b) Slice 2 of Patient 004	85
FIGURE 4.22 - Area-Weighted Average of Scalar0 for (a) Slice 1 and (b) Slice 2 of Patient 005	86

LIST OF FIGURES (CONT.)

	<u>Page</u>
FIGURE 4.23 - Area-Weighted Average of Scalar0 for (a) Slice 1 and (b) Slice 2 of Patient 017	86
FIGURE 4.24 - Area-Weighted Average of Scalar0 for (a) Slice 1 and (b) Slice 2 of Patient 019	86
FIGURE 4.25 - Area-Weighted Average of Scalar0 for (a) Slice 1 and (b) Slice 2 of Patient 041	87
FIGURE 4.26 - Area-Weighted Average of Scalar0 for (a) Slice 1 and (b) Slice 2 of Patient 045	88
FIGURE 4.27 - Area-Weighted Average of Scalar0 for (a) Slice 1 and (b) Slice 2 of Patient 046	88
FIGURE 4.28 - Area-Weighted Average of Scalar0 for (a) Slice 1 and (b) Slice 2 of Patient 058	88
FIGURE 4.29 - Area-Weighted Average of Scalar0 for (a) Slice 1 and (b) Slice 2 of Patient 061	89
FIGURE 4.30 - Area-Weighted Average of Scalar0 for (a) Slice 1 and (b) Slice 2 of Patient 075	89
FIGURE 4.31 - Velocity Contours for (a) Slice 1 and (b) Slice 2 of Patient 004	92
FIGURE 4.32 - Velocity Contours for (a) Slice 1 and (b) Slice 2 of Patient 005	92
FIGURE 4.33 - Velocity Contours for (a) Slice 1 and (b) Slice 2 of Patient 017	93
FIGURE 4.34 - Velocity Contours for (a) Slice 1 and (b) Slice 2 of Patient 019	93
FIGURE 4.35 - Velocity Contours for (a) Slice 1 and (b) Slice 2 of Patient 041	94
FIGURE 4.36 - Velocity Contours for (a) Slice 1 and (b) Slice 2 of Patient 045	94
FIGURE 4.37 - Velocity Contours for (a) Slice 1 and (b) Slice 2 of Patient 046	95
FIGURE 4.38 - Velocity Contours for (a) Slice 1 and (b) Slice 2 of Patient 058	95
FIGURE 4.39 - Velocity Contours for (a) Slice 1 and (b) Slice 2 of Patient 061	96
FIGURE 4.40 - Velocity Contours for (a) Slice 1 and (b) Slice 2 of Patient 075	96
FIGURE 4.41 - Quadrant Plot Correlating the Mean Age of Red Blood Cells with <i>FFR</i> for the Three-Dimensional Source Rendering.....	100
FIGURE 4.42 - Quadrant Plot Correlating the Mean Age of Red Blood Cells with <i>FFR</i> for the Two-Dimensional Geometry of Slice 1	102
FIGURE A.1 - Area-Weighted Average of Scalar1 for (a) Slice 1 and (b) Slice 2 of Patient 004	115
FIGURE A.2 - Area-Weighted Average of Scalar1 for (a) Slice 1 and (b) Slice 2 of Patient 005	115
FIGURE A.3 - Area-Weighted Average of Scalar1 for (a) Slice 1 and (b) Slice 2 of Patient 017	116
FIGURE A.4 - Area-Weighted Average of Scalar1 for (a) Slice 1 and (b) Slice 2 of Patient 019	116
FIGURE A.5 - Area-Weighted Average of Scalar1 for (a) Slice 1 and (b) Slice 2 of Patient 041	116
FIGURE A.6 - Area-Weighted Average of Scalar1 for (a) Slice 1 and (b) Slice 2 of Patient 045	117

LIST OF FIGURES (CONT.)

	<u>Page</u>
FIGURE A.7 - Area-Weighted Average of Scalar1 for (a) Slice 1 and (b) Slice 2 of Patient 046	117
FIGURE A.8 - Area-Weighted Average of Scalar1 for (a) Slice 1 and (b) Slice 2 of Patient 058	117
FIGURE A.9 - Area-Weighted Average of Scalar1 for (a) Slice 1 and (b) Slice 2 of Patient 061	118
FIGURE A.10 - Area-Weighted Average of Scalar1 for (a) Slice 1 and (b) Slice 2 of Patient 075	118

I. INTRODUCTION

Cardiovascular diseases are a frequent aggressor of health in today's society, and they remain pervasive as a result of easily disregarded risk factors such as poor diet and sedentary lifestyles. Coronary artery disease (CAD) is the most prominent type of cardiovascular disease, and it is the leading cause of mortality worldwide. CAD signifies the existence of inflammatory atherosclerosis affecting the inner wall of coronary arteries in an occlusive manner. Directly, plaques may accrete in response to fibrosis and calcification, leading to the thickening of the inner wall of arteries and advancing the constriction of arterial lumina to cause a stenosis.

The predominance of cardiovascular diseases such as CAD has generated significant interest in the areas of associated risk factor analysis, prevention, and the development of uncomplicated diagnosis. Presently, invasive coronary angiography (ICA) employs catheterization to obtain a moving picture of the coronary system, but a limitation of this utility arises from its incapacity to enumerate the physiological extent of stenoses. As a result, the metric of fractional flow reserve (*FFR*) was developed to assess the fraction of maximal blood flow that may be achieved in a stenotic artery by invasively measuring a ratio of pressures distal and proximal to a stenosis. A measured *FFR* value less than 0.80 is the threshold below which a cardiologist intervenes with stent placement to prevent ischemia. The invasive determination of *FFR* has risen to represent the current gold standard for decision making on stent placement.

Current research has extended the topic of *FFR* to its use in non-invasive, computationally-derived techniques such as coronary computed tomography angiography (coronary CTA). Specifically, fractional flow reserve derived from coronary CTA

(FFR_{CT}) has emerged to become an innovative and non-invasive technique for evaluation of stenoses. FFR_{CT} is calculated from hyperemic blood flow simulated in arterial renderings using computational fluid dynamics (CFD) to determine the possibility of CAD and the extent of stenoses. Its adoption, however, is largely dependent on the monumentally challenging prospect of the medical industry's acceptance of coronary CTA as a successor to ICA.

This thesis investigates a presently competing approach that utilizes CFD and multiphase mean age theory to unite angiography with a non-invasive stenotic evaluator. Multiphase mean age theory is a concept founded on principles of residence time distributions (RTDs) and mean age distributions developed by Danckwerts in the 1950s. Mean age distributions overcome the limitation of discrete sampling at the system exit typically associated with RTDs, thereby providing full insight into the spatial distribution of mixing throughout an entire system volume. Nevertheless, mean age distributions are largely impractical to develop experimentally due to the contingency of measuring an applied passive tracer throughout an entire system volume. CFD, however, is an ideal tool for spatially resolved mixing. Mean age theory and its extension to multiphase systems, in conjunction with CFD, redefines time as a passive scalar in the transient advection-diffusion equation, allowing conventionally time-based variables to be analyzed with a steady-state solution.

The objectives of the work presented in this thesis were to simulate blood flow through arterial renderings, apply multiphase mean age theory using CFD, and compare a novel mean age metric determined from two-dimensional arterial slices with those that are used to detect and assess a stenotic artery determined from corresponding three-

dimensional arterial renderings. The most significant outcome if similar results were obtained between three- and two-dimensional processing would be reduced computational runtime. A shortcoming of CFD processing of three-dimensional flow arises from considerably lengthy calculation runtimes. Even with parallel computing on up to 20 processors, calculations can approach a total duration on the order of several hours to simulate multiphase flow in a typical three-dimensional segment of an artery. Simulating flow in a two-dimensional slice of the same segment takes on the order of about 60 minutes.

With the motivation of the content of this thesis considered, the specific objectives are:

- 1) generate two-dimensional arterial slices from three-dimensional source renderings using computer-aided design software packages;
- 2) use multiphase mean age theory in conjunction with CFD modeling to simulate blood flow in five two-dimensional cases above and five two-dimensional cases below the 0.80 *FFR* threshold value; and
- 3) compare the mean age metric determined from the two-dimensional arterial slices to those determined from the corresponding three-dimensional source renderings.

II. LITERATURE REVIEW

A. Coronary Artery Disease (CAD)

1. General Information: Pathophysiology and Epidemiology

Coronary artery disease (CAD) is a cardiovascular disease typified by plaque buildup in the walls of the arteries that supply blood to the heart and other parts of the body. CAD refers to the process of atherosclerosis pathologically affecting coronary arteries, and the disease includes a spectrum of consequential diagnoses including angina pectoris, myocardial infarction, silent myocardial ischemia, and sudden cardiac death (Hanson et al., 2013). CAD may be more descriptively defined as an inflammatory disease with lipid and macrophage collection on arterial walls as a result of developing atherosclerosis (Sun and Xu, 2014).

Atherosclerosis is an inflammatory disease of the inner wall of coronary arteries that is hastened by the commonly known risk factors of high blood pressure, high cholesterol, tobacco use, and diabetes. Atherosclerosis is slowly progressive, however, and it silently develops through fibrosis and calcification (Gerber, 2007). The gradual accretion of plaques leads to the thickening of the inner wall of arteries, permitting, over time, the considerable constriction of arterial lumina (Ambrose and Singh, 2015). Defined as stenosis, the narrowing of arterial passageways is the foundational point of concern for CAD and its resultant diagnoses. When plaques hinder a coronary lumen and create a stenosis, blood flow is obstructed, occasionally establishing stable angina pectoris, a condition characterized by discomfort and pain in the chest. In other cases, the initiation of platelets and blood coagulation factors may occur if the thinned endothelium covering non-occlusive, lipid-rich plaques unexpectedly ruptures and exposes thrombotic

components to blood (Gerber, 2007). As a result, coronary lumen occlusion may occur, instigating ischemia and imparting the substantially more critical issues of unstable angina pectoris, myocardial infarction, silent myocardial ischemia, or sudden cardiac death.

Since CAD develops slowly, strikes unexpectedly, and proliferates through easily unheeded risk factors (e.g., poor diet and sedentary lifestyles), it is predictably the leading cause of death worldwide (Finegold et al., 2012), and it is responsible for nearly 7.3 million annual deaths and 58 million disability-adjusted life years lost worldwide (Sun and Xu, 2014). In the United States, CAD is estimated to affect 16.8 million people alone (Cassar et al., 2009). With this, an American will have a coronary-related event approximately every 25 seconds, and someone will die of one every minute (Hanson et al., 2013). While CAD is the leading cause of morbidity and mortality in advanced countries, its pervasiveness is amply rising in developing countries as well (Sun and Xu, 2014). This is attributable to the broader issue of cardiovascular disease becoming widespread as developing countries transition epidemiologically from pestilence and famine to pandemics and progressive diseases (Cassar et al., 2009). In 2002, out of a worldwide total of 57 million deaths, around 17 million were due to cardiovascular disease, and CAD was responsible for nearly half of these cardiovascular deaths (Cassar et al., 2009). While high income countries have recently seen declines in deaths from CAD, continued high CAD mortality is persistent elsewhere (Finegold et al., 2012), with the mortality rate from cardiovascular disease predicted to reach 23.4 million in 2030 (Cassar et al., 2009).

2. Current State of Diagnosis

The predominance of CAD has sparked widespread interest in risk factor analysis, prevention, and the development of uncomplicated diagnosis. While risk factors may be moderated by proper diet and lifestyle, testing, when needed, is sought to become uncomplicated and non-invasive in pursuance of enabling routine checkup and fulfilling time-sensitive constraints incumbent upon the disease. The tests currently available for CAD differ in modality and utility, and they serve to stand in comparison to the gold standard of invasive coronary angiography. The following list from Hanson et al. (2013) summarizes the current state of available tests for CAD diagnosis:

- a. Electrocardiography (ECG). ECG is the most common test for CAD, and it serves to map the heart rate rhythm over a duration of time. ECG may show changes in electrical activity that designate ischemia or indicate previous complications of mild myocardial infarction. Despite this, ECG is inadequate for full diagnosis since some patients with CAD may produce ordinary results if the heart is not under any stress.
- b. Stress Test. Stress tests involve heart evaluation during concentrated exercise usually on a treadmill. Since some signs of CAD may only surface if the heart is under exertion, ECG and blood pressure monitoring are utilized in parallel while a patient exercises. A patient may experience angina pectoris, and possible changes in electrical activity or blood pressure could designate ischemia. During the test, patients may also face exertional hypotension or hypertension. Exertional hypotension occurs when the blood pressure decreases to values lower than the resting systolic pressure, and it regularly signifies severe heart failure or multivessel CAD. With this, exertional hypertension may

also arise, but it is usually not as troublesome as exertional hypotension and is simply evidence of long-term high blood pressure.

- c. Myocardial Perfusion Imaging. Myocardial perfusion imaging utilizes radioactive tracers such as thallium and sestamibi to show how well blood perfuses several areas of the heart. These tests are typically performed with a stress test. The radioactive substance is injected intravenously, and a special camera takes images around the heart. Typical myocardium receives more thallium/sestamibi than myocardium being supplied by an occlusive coronary artery, so this test can provide partial evidence to the extent of possible CAD.
- d. Coronary Artery Calcium Computed Tomography (CT). Coronary artery calcium CT exploits the presence of calcium-rich components in the plaques created by atherosclerosis. A cardiac CT scan may be performed and placed in context of measured levels of calcium deposits. The supposition is that there is a higher chance of CAD if there is a considerable sum of measured calcium. The Agatston score quantifies the extent of coronary artery calcification, and it is ultimately used to strengthen claims of CAD diagnosis.
- e. Coronary Computed Tomography Angiography (CTA). Coronary CTA scans the coronary arteries following the intravenous injection of a radioactive substance. An X-ray source is used to irradiate the area of pertinence to permit scans and images of the coronary arteries. Using computer software, algorithms may construct three-dimensional arterial renderings by linking images together. As a result, the capacity of coronary occlusion may be seen visually, enabling informed judgments on CAD diagnosis.

f. Invasive Coronary Angiography (ICA). Invasive coronary angiography is the gold standard for CAD diagnosis due to its effectiveness. For this test, a catheter is threaded to the heart by initial insertion into vessels through the groin, arm, or neck. The heart receives an injection of a radioactive substance while angiographs are continually acquired. As a result, a moving picture of the coronary system is obtained, providing specific information about the valves and arterial function. Important details such as wall motion abnormalities and left ventricle ejection fraction may be easily evaluated from the angiograms to provide supportive consensus of CAD diagnosis.

The current state of available tests for CAD diagnosis may be tabulated with additional metrics. Hanson et al. (2013) provide the comparison of test sensitivity, specificity, advantages, and disadvantages shown in TABLE 2.1:

TABLE 2.1

A COMPARISON OF TESTS USED FOR CAD DIAGNOSIS

Test	Sensitivity [%]	Specificity [%]	Advantages	Disadvantages
ECG	68	97	Inexpensive	–
Stress Test	Females: 31–33 Males: 68	Females: 52–76 Males: 77	Well validated, inexpensive, readily available	Less useful for those with atypical CAD presentation
Myocardial Perfusion Imaging	90	70	High sensitivity	Expensive
Coronary Artery Calcium CT	91	46	Adds prognostic value to intermediate risk group	Low specificity
Coronary CTA	94	82	Non-invasive	New modality, expensive, radiation exposure
ICA	–	–	Gold standard	Invasive, expensive, radiation exposure

Test sensitivity and specificity refer, respectively, to the ability of a test to correctly identify those with the disease and the ability of the test to correctly identify those

without the disease. Using these metrics, the two angiographic techniques shown in TABLE 2.1 represent the best methods of examination yet simply differ in procedural ideation and execution.

B. Fractional Flow Reserve (*FFR*) in Angiography

1. Definition

While coronary angiographic techniques represent the preferred forms of diagnostics, a shortcoming of their value stems from their inability to characterize the physiological magnitude of stenoses. For hearts with normal myocardium and arteries, blood flow may increase three to five times in response to hyperemia induced by temporary occlusion (Lederman et al., 1997). For hearts with normal myocardium and a stenosis, the hyperemic myocardial flow gradually dampens with increasing percentages of stenosis, beginning at about 50% (Lederman et al., 1997). At that percentage, a stenosis is considered to impede full flow capability, thereby substantiating physiological impact. Importantly, angiographic techniques are unreliable in predicting functional flow consequences of a stenosis, meaning other approaches must be applied to further develop the physiological merit of angiographic diagnoses of CAD.

Various methods have been used in an attempt to physiologically assess coronary stenoses, but the concept of fractional flow reserve (*FFR*) has gained the most attention for clinical utility due to its emergence as a quick and accurate physiological appraisal technique (Lederman et al., 1997). *FFR* is defined as the ratio of flow across a stenosis to putative flow in the absence of stenosis (Nørgaard et al., 2015). As a result, *FFR* enumerates the fraction of maximal blood flow that may be achieved in a stenotic artery.

Pijls et al. (1996) utilized the research on coronary flow reserve (*CFR*) from Gould et al. (1974) to develop a model using translational pressure gradients to mathematically describe *FFR*. While *CFR* is similar in its definition to *FFR*, its gauging relies on direct flow measurement. Pijls et al. (1996) overcame direct flow measurement reliance by modifying Poiseuille's law, permitting the establishment of the concept of *FFR*. Under Poiseuille's law, the volumetric flow rate of a fluid is proportional to the pressure drop across the associated zone of interest and inversely proportional to flow resistance in that same zone. As such, the pressure drop across the resistance governs the volumetric flow rate through a resistant artery (Lederman et al., 1997). Supposing the myocardium is supplied by an artery with a stenosis, the pressure drop is obtained by subtracting the venous pressure from the pressure distal to the stenosis (i.e., $p_d - p_v$) (Lederman et al., 1997). With this, supposing the same artery were not stenotic, the pressure drop calculation shifts to a difference in arterial and venous pressures (i.e., $p_a - p_v$) (Lederman et al., 1997). Volumetric flow rates are obtained by dividing each pressure drop by resistance R , and a ratio of these volumetric flow rates gives:

$$FFR = \frac{(p_d - p_v)/R}{(p_a - p_v)/R} = \frac{p_d - p_v}{p_a - p_v} \quad (2.1)$$

If, as in many circumstances, venous pressure is not elevated, Lederman et al. (1997) suggest p_v may be excluded to give a simpler ratio:

$$FFR = \frac{p_d}{p_a} \quad (2.2)$$

For normal arteries, *FFR* is unity since p_d equals p_a . For stenotic arteries, however, the pressure drop increases as occlusion increases, meaning p_d and *FFR* decrease.

2. Use in ICA and the Extension to Coronary CTA

The use of *FFR* in ICA procedures represents the current gold standard for determining whether an arterial stenosis causes ischemia (Min et al., 2015). *FFR* calculation begins with the induction of hyperemia with intravenous adenosine to collect physiological data on the flow resistance a stenosis is causing (Lederman et al., 1997). Using a catheter, a sensor collects the required pressures at the necessary locations across the suspected stenosis, calculating a value of *FFR*. An *FFR* less than or equal to 0.80 is usually recognized as the limit below which a stenosis is considered to cause ischemia (Min et al., 2015). Knowing this threshold value, clinical strategies regarding subsequent procedural actions may be targeted appropriately. Specifically, coronary intervention may be safely deferred for vessels with an *FFR* greater than 0.80, while coronary revascularization is recommended for vessels with a measured *FFR* less than or equal to 0.80 (Min et al., 2015). In establishing a decisive threshold value of *FFR*, improved clinical outcomes and reduced costs have been seen when compared to an ICA only, non-*FFR* examination (Min et al., 2015). Ultimately, the addition of the physiological component of *FFR* to ICA's anatomically-based evaluations of stenosis severity facilitate proper coronary actions that are enduring and cost-effective (Min et al., 2012). As of yet, however, this methodology unifying physiological and anatomical components has not been available through non-invasive techniques.

In an attempt to establish a non-invasive test that quantifies both coronary stenosis severity and the associated ischemia, research has increased in the topic of *FFR* to extend its use in non-invasive coronary CTA. As a result, fractional flow reserve derived from coronary CTA (*FFR_{CT}*) has emerged to become an innovative and non-invasive method

for precise analysis of coronary ischemia caused by a stenosis. FFR_{CT} utilizes computational fluid dynamics (CFD) to assess the physiological extent of CAD. Importantly, CFD may be used to calculate a value of FFR_{CT} from previously acquired coronary CTA images without the need for further tomographic steps (Min et al., 2015).

Computing FFR_{CT} from coronary CTA images necessitates the generation of a physiological model of coronary blood flow, and Nørgaard et al. (2015) describe the principles on which the model is established. Specifically, the first principle maintains that the sum of resting coronary blood flow may be computed relative to the mass of myocardium assessed by CT. The second principle asserts that the resting vascular resistance is inversely proportional to the size of the coronary arteries supplying the myocardium. Finally, the third principle states that the vasodilatory response to adenosine introduction is predictable, allowing computational modeling of hyperemia. With these principles established, Min et al. (2015) outline the five required steps for FFR_{CT} calculation:

- 1) create patient-specific anatomical models from coronary CTA;
- 2) quantify the coronary artery flow in the hypothetical case in which the supplying vessels are normal;
- 3) determine the baseline resistance for the arteries supplying the myocardium;
- 4) quantify the changes in coronary resistance as a result of hyperemia; and
- 5) apply CFD methods for calculation of coronary flow, pressure, and velocity at hyperemia.

The grouping of the principles into three-dimensional computational models and the execution of the five steps permit the calculation of metrics at every point in the coronary

system under normal and hyperemic conditions. In doing so, FFR_{CT} is thusly determined in an analogous manner to its invasive form in ICA.

The utilization of CFD to evaluate coronary CTA images enables the computation of arterial blood flow and the calculation of stenosis-specific FFR_{CT} without the need for an invasive procedure. This is to say the computation of FFR_{CT} enables the identification of patients with physiologically significant stenoses prior to invasive cardiac catheterization. Moreover, the utility of FFR_{CT} is underscored by its investigative potential in modeling innocuous revascularization procedures. Kim et al. (2014) show that the same CFD technology could be used to modify stenoses of existing flow models to visualize virtual stenting of a pertinent coronary area. In doing so, coronary blood flow and FFR_{CT} could be recalculated from the new model and be used to validate the circulatory effect of the stent on a stenosis-specific basis. Ultimately, the prediction of revascularization benefit via virtual approaches extends the continual non-invasive value of coronary CTA and its associated FFR_{CT} .

3. Clinical Comparison of FFR and FFR_{CT}

While FFR_{CT} calculation is proven beneficial with regards to characterizing arterial blood flow and identifying physiologically significant coronary stenoses, its comparison to FFR from a clinical perspective is principal in efficacy and applicability determination. Since its incipience of viability within the past decade, FFR_{CT} has gained clinical evidence that may be compared to the diagnostic performance of an invasive FFR reference standard (Min et al., 2015). Using a blinded comparison of FFR_{CT} to FFR , trials involving over 600 patients and 1000 vessels assessing the diagnostic functionality of FFR_{CT} in recognizing ischemia caused by stenosis in CAD-related

instances have been executed (Nørgaard et al., 2015). Using prospective designs with demarcations of obstructive CAD at stenoses greater than 50% and ischemia at FFR or FFR_{CT} values less than or equal to 0.80, Nørgaard et al. (2015) provide the comparison of design, population, test accuracy, sensitivity, and specificity of the studies shown in TABLE 2.2:

TABLE 2.2
STUDIES COMPARING FFR_{CT} DIAGNOSTIC PERFORMANCE USING FFR AS
THE REFERENCE STANDARD

Study	Design	Population	Accuracy [%]	Sensitivity [%]	Specificity [%]
DISCOVER-FLOW	Statistically powered on a per-vessel basis, 4 centers	<ul style="list-style-type: none"> • Patients with suspected or known CAD who underwent coronary CTA, ICA, and FFR. All patients had at least one stenosis $\geq 50\%$ in a major vessel at coronary CTA. • 103 patients (159 vessels) • Mean age: 63 years • 26% female, 74% male • Proportion of vessels with $FFR \leq 0.80$: 56% 	84	88	82
De-FACTO	Statistically powered on a per-patient basis, 17 centers	<ul style="list-style-type: none"> • Patients with suspected or known CAD who underwent clinically indicated non-emergent ICA after coronary CTA (< 60 days), and with at least one ICA stenosis 30–90% • 252 patients (408 vessels) • Mean age: 63 years • 29% female, 71% male • Proportion of patients with $FFR \leq 0.80$: 53 % 	73	90	54
NXT	Statistically powered on a per-patient basis, 10 centers	<ul style="list-style-type: none"> • Patients suspected of CAD who underwent coronary CTA and ICA within < 60 days • 254 patients (484 vessels) • Mean age: 64 years • 36% female, 64% male • Proportion of patients with $FFR \leq 0.80$: 32 % 	81	86	79

The values listed in TABLE 2.2 represent per-vessel and per-patient diagnostic metrics for FFR_{CT} all greater than or equal to respective percentages for coronary CTA alone. For example, Nørgaard et al. (2015) report that the DISCOVER-FLOW study was concluded by obtaining per-vessel diagnostic accuracy of 84% for FFR_{CT} compared to 59% for coronary CTA alone, and this arose by specificity increasing from 40% for coronary CTA alone to 82% for FFR_{CT} . This shows the aptitude of FFR_{CT} in diagnosing CAD when compared to using coronary CTA on its own. With this, Nørgaard et al. (2015) also report an increased capacity to discern ischemia on a per-vessel and per-patient basis. This is due to consistent increases in respective area under receiver operating characteristics curves—a measure of how well a parameter can distinguish between two diagnostic groups (i.e., having and not having ischemia)—for each percentage entry in TABLE 2.2. As a result, FFR_{CT} derived from coronary CTA images using FFR as the reference standard provides high diagnostic performance in patients with supposed CAD, thereby encouraging its use as an efficacious tool capable of delivering increased analytical sensitivity for anatomical evaluation of the disease and high specificity for physiological detection of accompanying ischemia. Ultimately, however, the widespread adoption of FFR_{CT} is dependent on the exigent prospect of the medical industry accepting coronary CTA as a successor to ICA.

C. Computational Fluid Dynamics (CFD)

1. General Information: Conservation and Discretization

Computational fluid dynamics (CFD) is a segment of fluid mechanics that solves fluid flow problems by employing numerical methods and data processing techniques. CFD is based on transport phenomena, where the conservations of mass, momentum, and

energy are of distinct importance. CFD programs offer the ability to solve these otherwise impractical conservation equations effectively and simultaneously. By solving the conservation equations using a discretized version of a geometric domain, ANSYS programs such as Fluent and CFX can simulate fluid flow and calculate relevant fluid metrics of user-based preference. In general, these programs have become ubiquitous in modeling, permitting the simulation of flow, heat transfer, and reactions for industrial applications—ranging from air flow over an aircraft wing to combustion in a furnace, from bubble columns to oil platforms, and from blood flow to wastewater treatment plants (Software: CFD Simulation, 2017).

The combination of governing conservation equations used to solve CFD cases depend on the individual system to be modeled. While the equation for energy conservation is only necessary for problems involving energy transfer, all systems must solve the conservation equations of mass and momentum. For the conservation equation of mass, continuity is described by:

$$\frac{\partial \rho}{\partial t} + (\nabla \cdot \rho \vec{v}) = S_m \quad (2.3)$$

The conservation equation of momentum is:

$$\frac{\partial}{\partial t} (\rho \vec{v}) + \nabla \cdot \rho \vec{v} \vec{v} = -\nabla p - [\nabla \cdot \boldsymbol{\tau}] + \rho \vec{g} \quad (2.4)$$

The viscous momentum flux tensor $\boldsymbol{\tau}$ represents shear stress and is given by:

$$\boldsymbol{\tau} = -\mu[\nabla \vec{v} + (\nabla \vec{v})^T] + \frac{2}{3}\mu(\nabla \cdot \vec{v})\boldsymbol{\delta} \quad (2.5)$$

Assuming constant fluid density and viscosity, substitution of $\boldsymbol{\tau}$ in the conservation equation of momentum and rearrangement gives the Navier-Stokes equation:

$$\rho \left(\frac{\partial \vec{v}}{\partial t} + \vec{v} \cdot \nabla \vec{v} \right) = -\nabla p + \mu \nabla^2 \vec{v} + \rho \vec{g} \quad (2.6)$$

The conservation of mass and Navier-Stokes equations are solved in CFD software by approximating the continuous variables in the partial differentials by discrete analogs and utilizing a discretized domain of a geometric mesh or grid. While continuous domains have flow variables defined at every point on the domain, discrete ones have flow variables defined only at the grid nodes. If each node interacts with adjacent nodes predictably, an accurate solution may be obtained. If the grid resolution (i.e., mesh count) is sufficient, discretized results approach analytical ones.

The simplest technique of discretization comes from the finite-difference method. For illustration of this method, Bhaskaran and Collins (2002) utilize a linear one-dimensional differential equation:

$$\frac{du}{dx} + u = 0; 0 \leq x \leq 1; u(0) = 1 \quad (2.7)$$

The domain may be discretized into equally-spaced points on a grid, with general grid points labeled x_i . Since the governing equation is valid for all x_i , the discretized form of Equation (2.7) is:

$$\left(\frac{du}{dx} \right)_i + u_i = 0 \quad (2.8)$$

To get an equation for the differential term in terms of u at the grid points, a Taylor series expansion may be used to give:

$$\left(\frac{du}{dx} \right)_i = \frac{u_i - u_{i-1}}{\Delta x} + O(\Delta x) \quad (2.9)$$

Excluding higher-order terms in the Taylor series, an algebraic equation is produced:

$$\frac{u_i - u_{i-1}}{\Delta x} + u_i = 0 \quad (2.10)$$

While the finite-difference method is simple, it illustrates the foundational discretization process. An extension to this technique that Fluent coding uses is the finite-volume method. In this method, integral forms of the conservation equations are applied to a cell of control volume to obtain discrete equations for each cell. The adjacency of control volumes creates a network of cells (i.e., a mesh), and the cells may be represented by a wide range of geometries, including those of quadrilaterals, triangles, hexahedra, tetrahedra, or prisms. An example of this method is illustrated by the integral form of the conservation equation of mass:

$$\int_S (\vec{v} \cdot \hat{n}) dS = 0 \quad (2.11)$$

Using an example square cell of length Δx , height Δy , and an imparting velocity vector of $a_i \hat{i} + b_j \hat{j}$, the discretized form of the integral equation is:

$$-a_1 \Delta y - b_2 \Delta x + a_3 \Delta y + b_4 \Delta x = 0 \quad (2.12)$$

Markedly, this equation sums the net mass flow into the control volume of the example square cell and sets it equal to zero. By similar treatment, discrete equations for remaining conservation equations for the cell may be achieved. Moreover, the finite-volume method is readily extendable to any other general cell shapes in two or three dimensions.

After discretization, equations are solved simultaneously and iteratively. Fluent permits choices between pressure-based and density-based solvers for iteration. Historically speaking, the pressure-based approach was developed for low-speed incompressible flows, while the density-based approach was mainly used for high-speed

compressible flows (Overview of Flow Solvers, 2009). Recently, however, both methods have been extended to solve and operate for a wide range of flow conditions beyond their traditional intent. In both methods, the velocity field is obtained from the conservation of momentum equation. For the pressure-based solver, the pressure field is extracted by solving a pressure equation obtained by manipulating conservation of mass and momentum equations. In the density-based approach, the conservation of mass equation is used to obtain the density field while the pressure field is determined from the equation of state. Several steps in the chosen iteration scheme must occur to advance the system to solution convergence. The two approaches of iteration schemes and the steps used to solve fluid flow problems are shown in FIGURE 2.1:

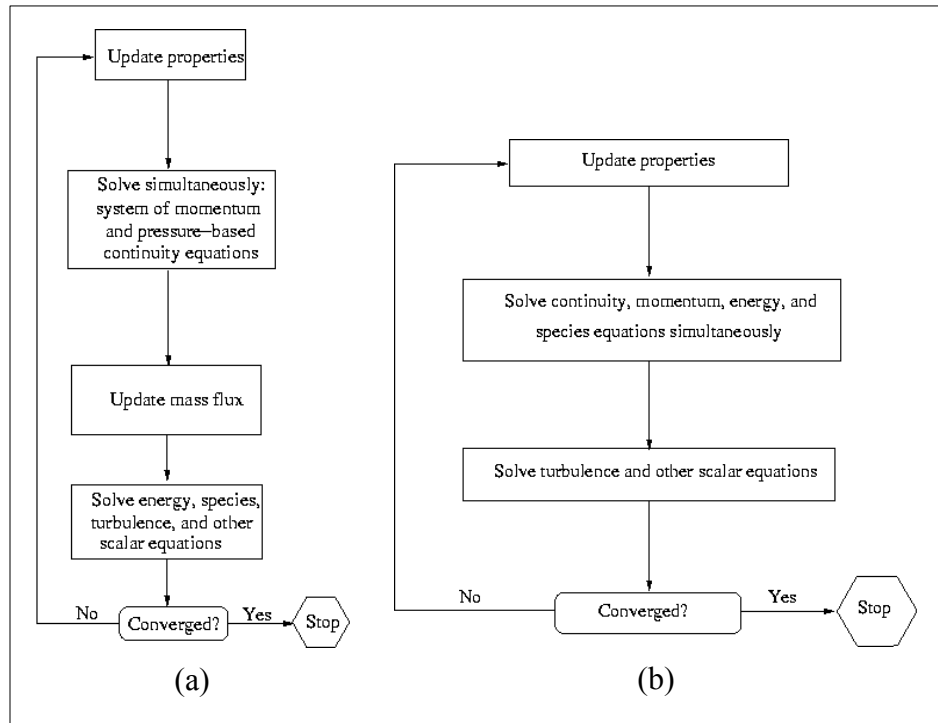


FIGURE 2.1 - Iteration Schemes for the (a) Pressure-based and (b) Density-based Solvers
(Overview of Flow Solvers, 2009)

Importantly, regardless of the solver used, convergence is checked by evaluating how much fluid properties have changed from the previous iteration to the current one. If the change (i.e., residual) is sufficiently small, the solution is converged. If not, the fluid properties are used as initial values for the next iteration, and the scheme repeats.

2. Utilization in Multiphase Systems

Recent advances in CFD have provided the basis for mathematically modeling the dynamics of multiphase systems. These systems are characterized by coexisting flow of materials with different phases (e.g., a liquid-gas system) or materials with differing chemical properties in the same phase (e.g., a water-oil system). The Euler-Lagrange and Euler-Euler methods are the two current approaches used for modeling these multiphase systems. The Euler-Lagrange approach treats the fluid phase as a continuum by solving the time-averaged Navier-Stokes equations and solves the dispersed phase by tracking many particles, bubbles, or droplets through the calculated flow field (Overview, 2006). While the dispersed phase can exchange momentum, mass, and energy with the fluid phase, the Euler-Lagrange approach relies on the fundamental assumption that the dispersed phase occupies a low volume fraction. The particle, bubble, or droplet trajectories are computed individually at specified intervals during the fluid phase calculation, meaning intensive computational processing requirements are needed.

The Euler-Euler approach is dissimilar by its treatment of both phases as interpenetrating continua (Approaches to Multiphase Modeling, 2006). Since both phases are considered continuous, the concept of phasic volume fraction is used. These volume fractions are assumed to be continuous functions of space and time and their sum equal to one. Conservation equations for each phase are implemented to obtain a set of similarly

structured equations for all phases. In Fluent, three different Euler-Euler multiphase models are available: volume of fluid, mixture, and Eulerian.

The volume of fluid method is a surface-tracking technique applied to a fixed Eulerian mesh (Approaches to Multiphase Modeling, 2006). It is used for two or more immiscible fluids, with the interface between the fluids being of most interest. In this model, the fluids share a single set of momentum equations, and the volume fraction of each of the fluids in each discretized cell is tracked across the domain. Applications of the volume of fluid method include the modeling of spray dryers and coal and liquid fuel combustion. Alternatively, the mixture model solves for the mixture momentum equation and assigns relative velocities to describe the dispersed phases, making it appropriate for modeling systems of sedimentation or cyclone operators that are rich with particles. Finally, the Eulerian model is the most complex of the multiphase models in Fluent, and it solves a large set of continuity and momentum equations for each phase and couples the pressure and interphase exchange coefficients as a way to link solutions for each phase (Approaches to Multiphase Modeling, 2006). Momentum exchange between the phases is dependent upon the type of mixture being modeled (e.g., granular or non-granular). Fluent's user-defined functions permit customization of the calculation of momentum exchange. Applications of the Eulerian method include bubble columns and arterial blood flow.

D. Age Topics

1. Residence Time Distributions (RTDs) and Mean Age Theory

Extensive analysis of residence time distribution (RTD) and age concepts began in the 1950s with Danckwerts. Before his research, the ideal mixing absolutes of none

(i.e., plug flow) or perfect (i.e., CSTR) were only considered and characterized, leaving a void in portraying real processes between these extrema. In 1953, Danckwerts modeled non-ideal mixing by measuring the residence time of fluid elements spent inside a system. Defining RTD, it is specifically a probability distribution function that expresses the amount of time a fluid element could spend inside a system, providing partial insight into non-ideal system mixing and dispersion properties. Danckwerts studied the probability distribution functions in a variety of vessel types and piping, establishing RTDs to be an operative quantifier of non-ideal mixing in real systems. While useful, a drawback to RTDs is that the produced function is typically limited to discrete sampling at the system exit, thus incognizant of characterizing internal happenings (Russ and Berson, 2016). In effect, an RTD provides no information regarding the spatial distribution of mixing along the length of a system. While the shape of the produced RTD function may imply the presence of dead zones in the mixing system, the location of such vessel areas cannot be determined from an RTD (Liu and Tilton, 2010). This prompts the desire to understand the spatial distribution of mixing beyond the area of exit and more internally.

In hopes of extending the topic, Danckwerts reclassified the term “residence time” for molecules exiting the system as a way to describe the elapsed time since they entered and developed the concept of “age” to describe the elapsed time since entrance of molecules still in the system (Liu and Tilton, 2010). Consequently, when a molecule reaches the exit, its age equals the residence time. As suggested, complete spatial distributions of age are most valuable, but they are generally unfeasible to develop experimentally since measurement is required across an entire system volume and

necessitate tracking the movement of a passive tracer (Russ and Berson, 2016). As a solution, in recent years, the application of mean age theory has provided an innovative approach in research associated with spatially resolved mixing. Mean age theory permits redefining time as a passive scalar in the transient advection-diffusion equation, facilitating analysis of traditionally time-based variables (e.g., mean residence time) while using a steady-state solution (Russ and Berson, 2016). Passive scalars may be thought of as virtual tracers that do not impact flow but are transported by the system as a way to track flow. While mean age theory was originally proposed by Danckwerts in 1958, technological restraints withheld the topic as strictly theoretical. With the rise of computational fluid dynamics (CFD), however, spatially resolved solutions for mean age theory purposes are now possible. While conventional solutions to the advection-diffusion equation require a time-demanding transient solution for modeling the time-dependent tracer behavior, CFD provides robust computing of the transient solution and the ability to report spatial and temporal resolution within the flow field (Russ and Berson, 2016).

2. Deriving Mean Age Conservation and the Extension to Multiphase Systems

Mean age theory as an approach to modeling the time-dependent behavior of a passive scalar in steady-state CFD simulations has been used to determine the mean age conservation equation plentifully in literature for a single-phase system (Liu and Tilton, 2010; Sandberg, 1981; Spalding, 1958). Russ and Berson (2016) extend the theory for multiphase systems by defining the passive scalar concentration independently for individual phases, permitting mean age to be solved at steady-state for each phase independently within a multiphase system. Liu and Tilton (2010) begin their derivation

by defining a spatially resolved concentration $C(x, t)$ for the passive scalar at a location x and time t . This concentration function is limited in utility for application, so Russ and Berson (2016) extend the definition by assuming:

$$C(x, t) = \rho\varphi(x, t) \quad (2.13)$$

Here, ρ is the density of the single phase and $\varphi(x, t)$ is the passive scalar value at a location x and time t . It follows that the concentration of a passive scalar value for an individual phase in a multiphase system is:

$$C(x, t) = \rho\varphi(x, t)\alpha(x, t) \quad (2.14)$$

Now, ρ is the density of an individual phase and $\alpha(x, t)$ is the phasic volume fraction of an individual phase at a location x and time t . Using these definitions of passive scalar concentration, the derivation for the mean age conservation equation follows directly from Liu and Tilton (2010).

Mean residence time for either definition of passive scalar concentration may be defined as:

$$\bar{t} = \frac{\int_0^{\infty} tC_{out}dt}{\int_0^{\infty} C_{out}dt} \quad (2.15)$$

This may then be extended for the spatial distribution of internal happenings by defining mean age as:

$$a = \frac{\int_0^{\infty} tC(x,t)dt}{\int_0^{\infty} C(x,t)dt} \quad (2.16)$$

To solve the mean age equation, the transient passive scalar advection-diffusion equation is used:

$$\frac{\partial C}{\partial t} + \nabla \cdot (\vec{v}C) = \nabla \cdot (D\nabla C) \quad (2.17)$$

In this equation, D is the molecular diffusivity. Equation (2.17) and the remaining derivation steps apply to laminar flow systems. In the case of turbulent flow systems, Equation (2.17) becomes the Reynolds averaged equation and D is replaced by the effective turbulent diffusivity D_e , provided that the time scale of turbulence is much smaller than the scale of mean residence time. If that criterion is met, the remaining derivation steps for laminar flow systems may be altered for turbulent flow systems by replacing D with D_e . Multiplication of Equation (2.17) by t and integration gives:

$$\int_0^\infty t \frac{\partial C}{\partial t} dt + \int_0^\infty \nabla \cdot (t\vec{v}C) dt = \int_0^\infty \nabla \cdot (D\nabla(tC)) dt \quad (2.18)$$

Here, t is independent of position and has been brought inside the spatial derivatives. The first term on the left-hand side of Equation (2.18) may be integrated by parts to give:

$$\int_0^\infty t \frac{\partial C}{\partial t} dt = tC|_0^\infty - \int_0^\infty C dt \quad (2.19)$$

The first term on the right-hand side of Equation (2.19) will be zero if tC is zero in the limit $t \rightarrow \infty$. That is, C must approach zero faster than t approaches infinity, indicating that the mean age a can exist only if $tC \rightarrow 0$ as $t \rightarrow \infty$. As such, the first term on the right-hand side of Equation (2.19) must equal zero so that:

$$\int_0^\infty t \frac{\partial C}{\partial t} dt = - \int_0^\infty C dt \quad (2.20)$$

Substitution of Equation (2.20) into Equation (2.18) and division by $\int_0^\infty C dt$ gives:

$$-1 + \nabla \cdot \left\{ \vec{v} \left[\frac{\int_0^\infty tC dt}{\int_0^\infty C dt} \right] \right\} = \nabla \cdot \left\{ D\nabla \left[\frac{\int_0^\infty tC dt}{\int_0^\infty C dt} \right] \right\} \quad (2.21)$$

Lastly, substituting the definition of a (Equation (2.16)), the general conservation equation for mean age is:

$$\nabla \cdot (\vec{v}a) = \nabla \cdot (D\nabla a) + 1 \quad (2.22)$$

Equation (2.22) may be simplified for incompressible flow in single-phase systems to give:

$$\vec{v} \cdot \nabla a = \nabla \cdot (D\nabla a) + 1 \quad (2.23)$$

Equation (2.22) mirrors the same form as the conservation equations of mass and momentum, enabling solution by the same CFD solver. It is noted that both definitions of $C(x, t)$ produce the same conservation equation, so mean age theory is now presently extended from single-phase to multiphase systems. Liu and Tilton (2010) derive boundary conditions for the conservation equation for mean age and are based on tracer concentration. Utilizing Equation (2.16) and the normal coordinate in the flow direction x_n , Liu and Tilton (2010) show that suitable boundary conditions for Equations (2.22) and (2.23) are:

$$a = 0, \text{ at inlet} \quad (2.24)$$

$$\hat{n} \cdot \nabla a = \frac{\partial a}{\partial x_n} = 0, \text{ on solid walls} \quad (2.25)$$

$$\hat{n} \cdot \nabla a = \frac{\partial a}{\partial x_n} = 0, \text{ at outlet} \quad (2.26)$$

Russ and Berson (2016) show that multiphase mean age theory is well validated by comparing experimental RTDs obtained from spatial mean age distributions to ones found computationally at two locations in the same water-oil flow system. Mean RTD

values and variances from multiphase mean age theory were within 1–3% and 3–11%, respectively, of experimental values. With this, mean RTD values and variances derived from multiphase mean age theory neared experimental values more closely than respective values derived from conventional transient solutions, indicating the innate steady-state solution associated with the theory increased the accuracy (Russ and Berson, 2016). Multiphase mean age theory is applicable to systems of any phase type, and since steady-state solutions are utilized, the theory is valuable for systems with lengthy residence times or ages.

III. EXPERIMENTAL METHODS

A. Preliminaries

1. Purpose

The purpose of this investigation was to utilize CFD and multiphase mean age theory as a way to compare a novel mean age metric determined from two-dimensional arterial slices with those that are used to detect and assess a stenotic artery determined from corresponding three-dimensional arterial renderings. Using supercomputing, calculations can approach a total duration on the order of days to simulate multiphase flow in a typical three-dimensional segment of an artery. Comparatively, simulating flow in a two-dimensional slice of the same segment takes on the order of about 60 minutes. If two-dimensional slicing can produce a similar mean age metric to its three-dimensional source, the more easily-processed, two-dimensional slices may be preferentially chosen to aid in long-term three-dimensional correlative approaches to *FFR*.

2. Plan

Two-dimensional arterial slices were generated from the three-dimensional source arteries using the computer-aided design software packages of ANSYS SpaceClaim and Dassault Systèmes SolidWorks. To better capture a wider range of the three-dimensional geometries, two orthogonal slices were created within each artery, giving two sets of ten (or 20 slices in total) to process. SpaceClaim was used to create two separate STEP files representing the three-dimensional arterial outlines, while SolidWorks was used to convert the outlines to two-dimensional surface entities via filling, flattening, and aligning. ANSYS Meshing was then used to create a discretized domain of a geometric mesh of at least 20,000 elements on the slices. Following this, ANSYS Fluent was used

to simulate pulsing blood flow and to calculate the mean ages of the plasma and red blood cell phases using user-defined scalars. From this, the mean ages of the two-dimensional slices were compared to nominal mean residence times to characterize the age impact of an occurring stenosis. Finally, the mean ages of the two-dimensional slices were then compared to respective three-dimensional mean age values of the source renderings for final assessment.

B. Materials

A Lenovo ThinkPad with an Intel Core i5-3320M CPU @ 2.60 GHz was used to run the ANSYS 17.1 software packages of Workbench, SpaceClaim, Meshing, and Fluent on Windows 7. With this, a MacBook Pro with an Intel Core i5-6267U CPU @ 2.90 GHz was used in conjunction with Parallels Desktop for Mac to run Dassault Systèmes SolidWorks on Windows 10.

DICOM-derived, three-dimensional STL files of arteries rendered by coronary angiograms were provided for slicing treatment. User-defined function (UDF) files were used to generate pulsing at the boundaries. Each UDF differs by multiplicative constants on the piecewise functions of Equations 3.1 and 3.2:

$$v_{inlet} = \begin{cases} 0.1, & 0 < t \leq 0.42 \\ 0.26 \sin(1.58\pi(t + 0.92)), & 0.42 < t \leq 0.9 \end{cases} \quad (3.1)$$

$$p_{outlet} = \begin{cases} 18665.13 \sin(1.4\pi(0.8t + 0.1305)), & 0 < t \leq 0.42 \\ -13400t + 22700, & 0.42 < t \leq 0.9 \end{cases} \quad (3.2)$$

Sample source code for a UDF file may be seen in APPENDIX I.

C. Procedures for Processing Two Orthogonal Arterial Slices

1. Geometry Generation

Arterial slice geometry was generated using ANSYS Workbench and the two computer-aided design software packages of ANSYS SpaceClaim and Dassault Systèmes SolidWorks. The following steps describe how to create arterial slices from three-dimensional arteries:

a. SpaceClaim. SpaceClaim was used to create two separate STEP files representing the three-dimensional arterial outlines.

i. New Geometry Module and SpaceClaim File. Open Workbench and drag a new Geometry module from the Toolbox pane to the Project Schematic pane. Right-click the Geometry module and click “New SpaceClaim Geometry...” to open SpaceClaim.

ii. Opening the STL File. Click File → Open and navigate to the three-dimensional STL file. Before opening the file, click “Options...” in the Open window and ensure the settings highlighted in FIGURE 3.1 are followed:

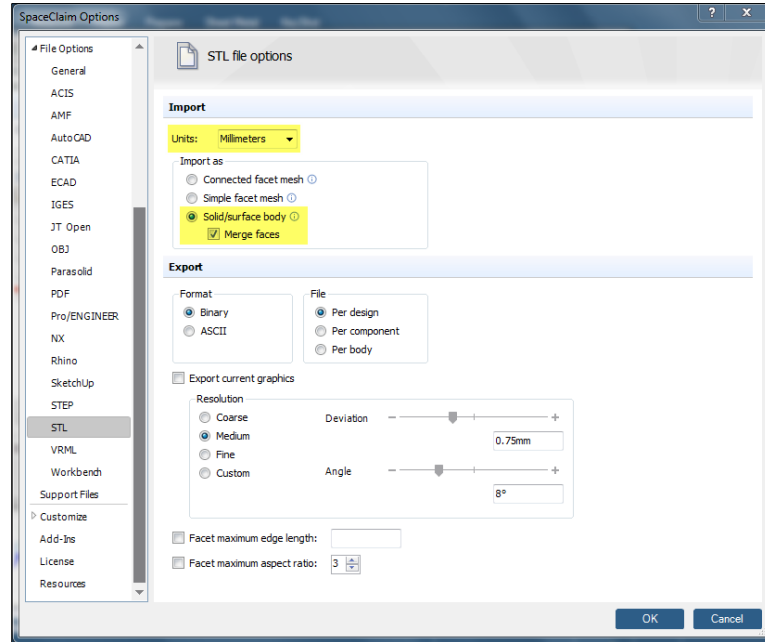


FIGURE 3.1 - STL File Opening Settings in SpaceClaim

Click “OK” in the SpaceClaim Options window and click “Open” in the Open window to import the three-dimensional geometry. Importantly, the geometry will have boundaries of a single face nearly circular in shape, while the wall will be composed of hundreds of faces of various shape.

- iii. Line Creation. Orthogonal markers are needed on both boundary faces to guide slice creation. To create orthogonal markers, choose Line from the ribbon. Under the Options - Sketch pane on the left, ensure the options highlighted in FIGURE 3.2 are followed:

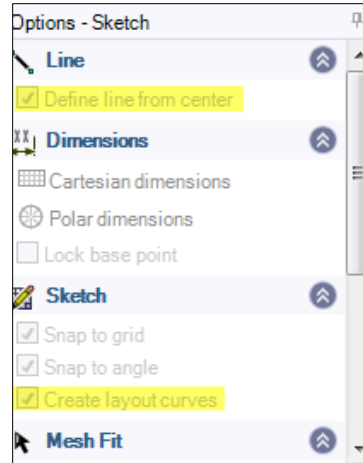


FIGURE 3.2 - Line Options in SpaceClaim

With Line selected from the ribbon, a grid will display on the drawing space. Move the cursor to a boundary face so that the grid displays major axes on it. FIGURE 3.3 displays this:

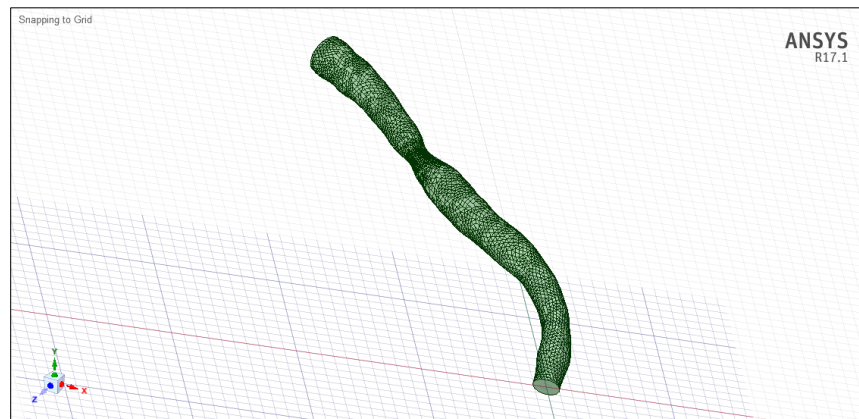


FIGURE 3.3 - Major Axes Displayed on a Boundary Face in SpaceClaim

Zooming in, draw two orthogonal lines on a boundary face that extend beyond the length of the face. The grid should be used to snap the lines and ensure orthogonality. FIGURE 3.4 displays this:

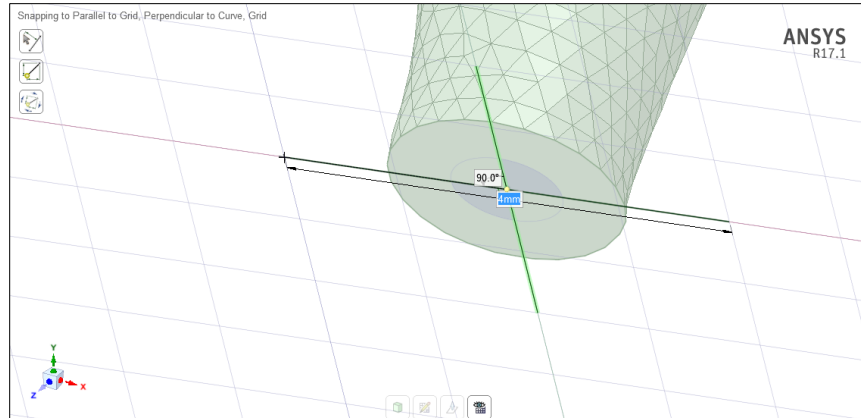


FIGURE 3.4 - Two Orthogonal Lines Extending Beyond a Boundary Face in SpaceClaim

With the two lines now extending beyond a boundary face, the lines must be reduced to the constraints of the face itself. Click Select from the ribbon and choose one of the four line endpoints. Using a combination of zooming and panning, hold the Shift key and drag the endpoint to the extent of the associated boundary face. Repeat this process for the remaining three endpoints so that the lines match that of FIGURE 3.5:

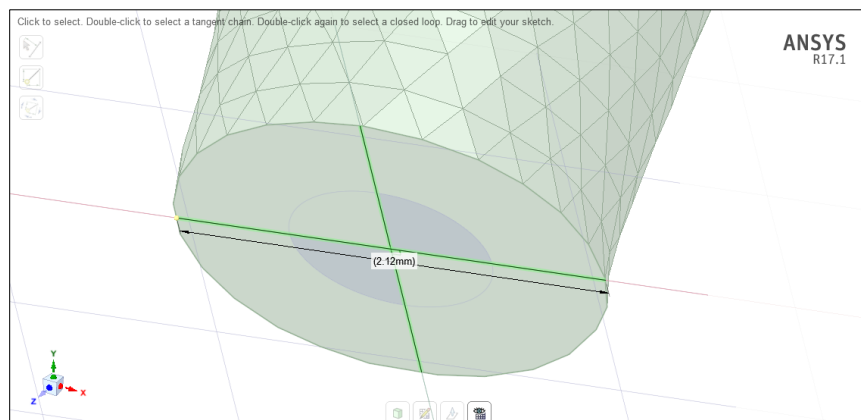


FIGURE 3.5 - Two Orthogonal Lines Reduced to the Extent of a Boundary Face in SpaceClaim

Rotating the object so that the other boundary face is visible, repeat this process of line creation on it. It is noted that the major axes used for the first face will be presented by default on the second face, and this ensures respective “horizontal” and “vertical” lines are kept similar. In total, four lines should be created. Alike lines from both faces serve as the boundary lines for the arterial slices. For organizational purposes, right-click the lines in the Structure pane and rename alike lines as Line1_1 and Line1_2 for Slice 1 and as Line2_1 and Line2_2 for Slice 2. The distribution of names is shown in FIGURE 3.6, where the three-dimensional object has been suppressed from visibility to make line discernment easier:

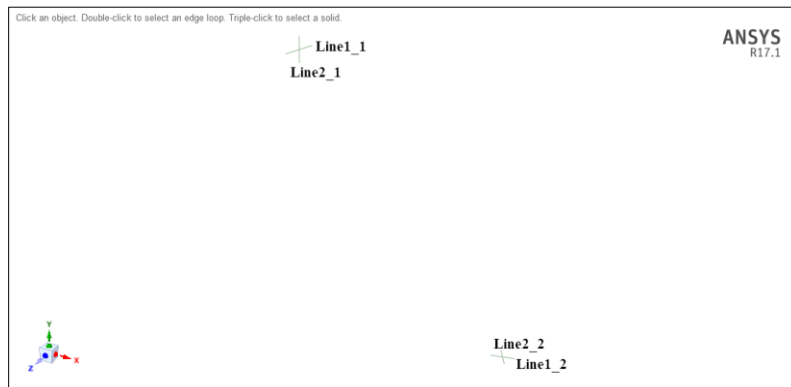


FIGURE 3.6 - Line Name Distribution in SpaceClaim

It is also noted here that the lines ending in “_1” denote what will eventually become inlet boundaries. The designation of inlet and outlet boundaries stems from choosing the face with the larger surface area to be the inlet.

- iv. Spline Creation. Splines are needed on the wall of the artery to create an outline for both slices. To create splines, choose Spline from the ribbon.

SpaceClaim defaults to two-dimensional creation, so type the D key to activate three-dimensional space control. Begin a spline creation by clicking the intersection point between a line created in iii and the perimeter of a boundary face. Using a combination of rotating, zooming, and panning, click points along the length of the wall of the artery until a connection is made to the alike line/boundary intersection. The initial creation of a spline is shown in FIGURE 3.7:

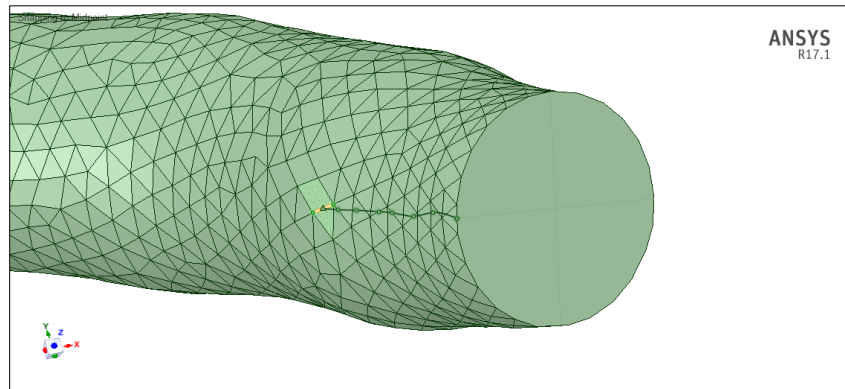


FIGURE 3.7 - Initial Spline Creation in SpaceClaim

The completed spline extending the length of the artery is shown in red in FIGURE 3.8:

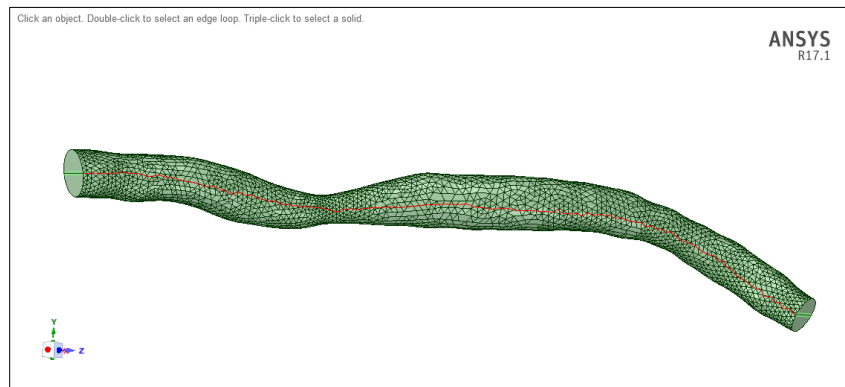


FIGURE 3.8 - Completed Spline (in Red) in SpaceClaim

Again, connection must be made to the respective line on the other end of the artery. Viewing FIGURE 3.7, it is clear that the arterial wall is composed of numerous faces. Splines snapping to the edges of these faces provides a difficulty in creating connections that stay consistent with the curvature of the geometry. Special care in guaranteeing acceptable spacing between clicked points must be taken to ensure an adequate connection between boundary lines is made. Rotating the object so that the other line/boundary intersections are visible, repeat this process of spline creation. In total, four splines should be created that are nearly equally spaced and form a frame of the artery. Alike splines from the same axis serve as the wall for the arterial slices. For organizational purposes, right-click the splines in the Structure pane and rename alike splines as Spline1_1 and Spline1_2 for Slice 1 and as Spline2_1 and Spline2_2 for Slice 2. Using red and green, the distribution of names is shown in FIGURE 3.9, where the three-dimensional object has been suppressed from visibility to make spline discernment easier:

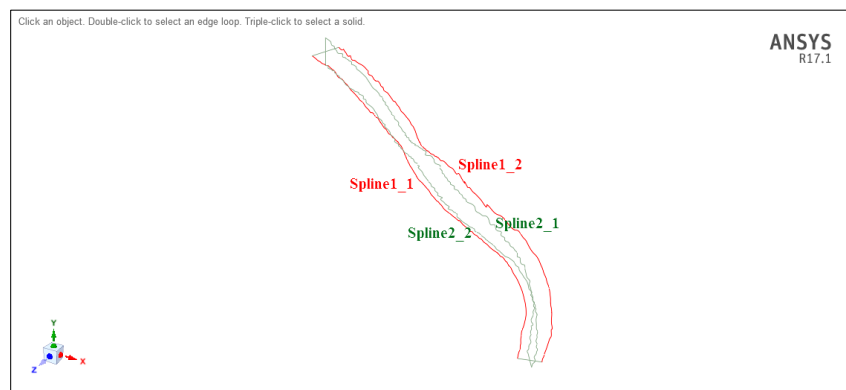


FIGURE 3.9 - Spline Name Distribution in SpaceClaim

It is noted that the outlines for each slice are now created. It is recommended to click File → Save As and save as a SpaceClaim file to create a file checkpoint to start from should downstream issues arise.

- v. Saving As a STEP File. The outlines of the two slices must be saved individually for proper analysis hereafter. To begin the process of saving the first slice outline, delete all geometry in the Structure pane aside from the first slice outline, delete all geometry in the Structure pane aside from the two lines and two splines outlining a slice. For example, to isolate the outline of Slice 1, right-click and delete the arterial body denoted as Solid, Line2_1, Line2_2, Spline2_1, and Spline2_2 in the Structure pane. In doing so, the outline for Slice 1 should be solely present. FIGURE 3.10 displays the Structure pane (a) before and (b) after deletion of Slice 2 components:

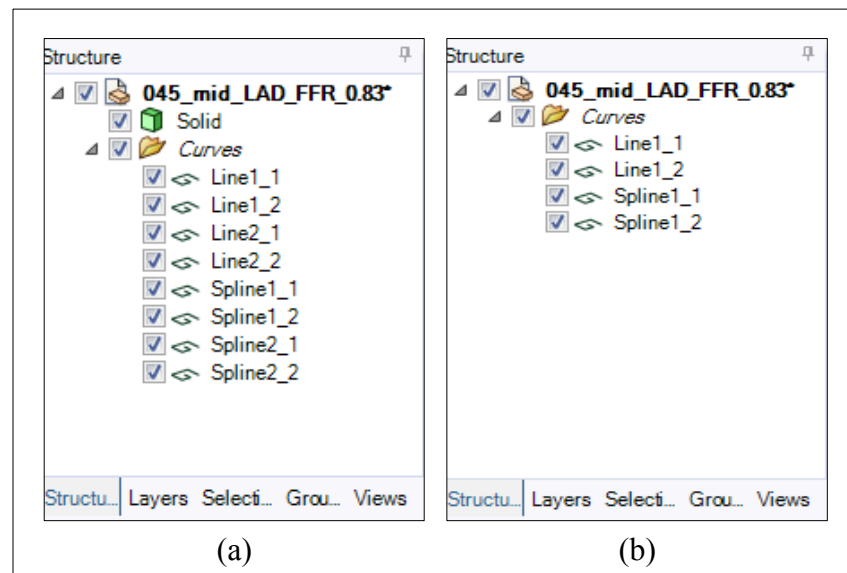


FIGURE 3.10 - Structure Pane (a) Before and (b) After Deletion of Slice 2 Components in SpaceClaim

In performing the above deletions, the only remaining components of geometry are those which outline Slice 1, and this is shown in FIGURE 3.11:

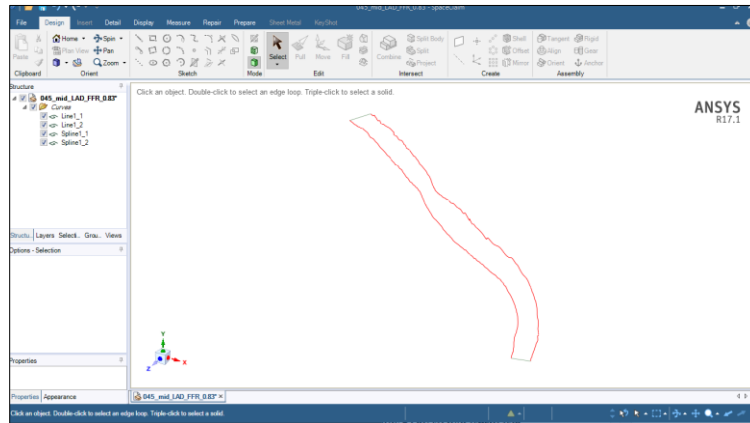


FIGURE 3.11 - Components of Geometry Outlining Slice 1 After Deletion of Slice 2 Components in SpaceClaim

With only the outline of Slice 1 present, click File → Save As. In the Save As window, ensure the options highlighted in FIGURE 3.12 are followed:

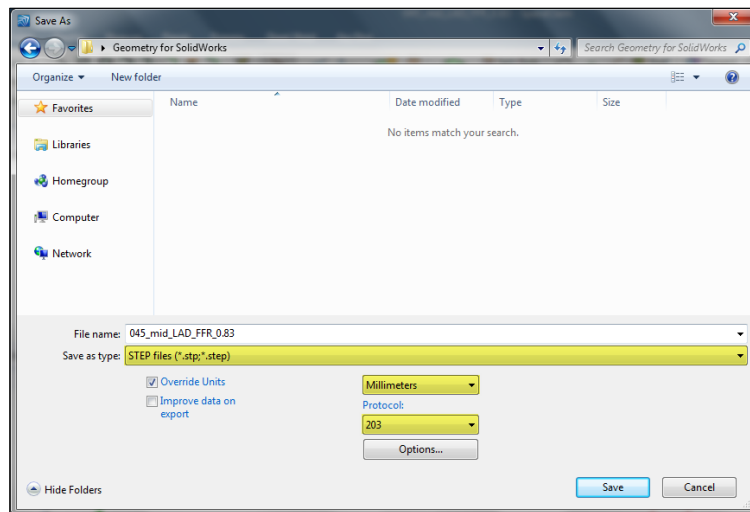


FIGURE 3.12 - Save As Window and Options for STEP File Creation in SpaceClaim

Click “Save” in the Save As window to create a three-dimensional STEP file for Slice 1. Finally, the saving process must be repeated for Slice 2. With SpaceClaim still open, undo the previous deletion of Slice 2 geometry (returning to file checkpoint) and invert the components to be deleted and delete them. Accordingly, to isolate the outline of Slice 2, right-click and delete the arterial body denoted as Solid, Line1_1, Line1_2, Spline1_1, and Spline1_2 in the Structure pane. In doing so, the outline for Slice 2 should be solely present. Repeat the Save As steps represented by FIGURE 3.12 to create a STEP file for Slice 2. Two separate STEP files representing the three-dimensional arterial outlines have been created and are in position for SolidWorks treatment.

- b. SolidWorks. SolidWorks was used to convert the three-dimensional arterial outlines to two-dimensional surface entities via filling, flattening, and aligning.
 - i. New SolidWorks File. Open SolidWorks. Click File → Open and navigate to one of the three-dimensional arterial outline STEP files created in SpaceClaim. Click “Open” in the Open window to import the three-dimensional geometry. Importantly, the geometry is a three-dimensional outline in position for two-dimensional surface conversion via filling, flattening, and aligning.
 - ii. Filling the Outline. Choose Filled Surface from the ribbon. With the blue Patch Boundary box highlighted in blue, select the geometric outline. The three-dimensional outline will fill to create a surface, which is shown in process in FIGURE 3.13:

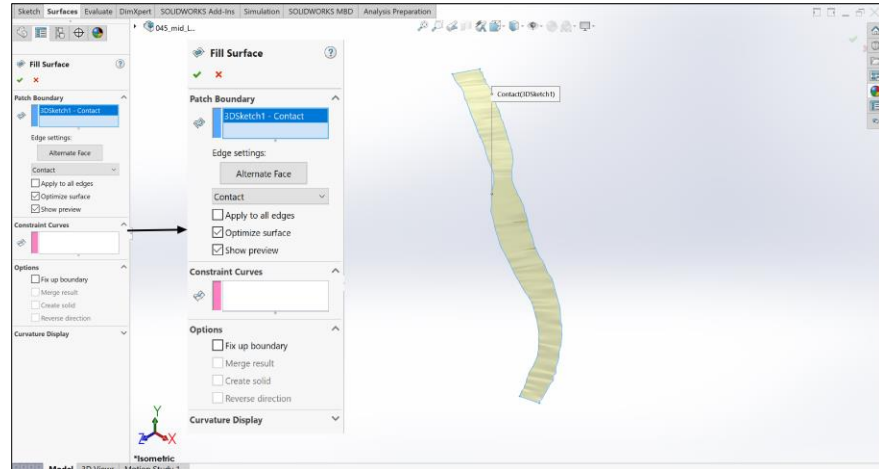


FIGURE 3.13 - Fill Surface Pane Magnified and the Three-Dimensional Outline Being Filled in SolidWorks

Click the green checkmark under the Fill Surface pane on the left to confirm the filling.

- iii. Flattening the Three-Dimensional Surface. Choose Surface Flatten from the ribbon. With the blue Face/Surface to Flatten box highlighted blue, select the surface. With the pink Vertex or Point on Edge to Flatten From box highlighted blue, select one of two boundary lines. Finally, click and drag the Accuracy handle to High. The three-dimensional surface will flatten to create a two-dimensional surface, which is shown in process in FIGURE 3.14:

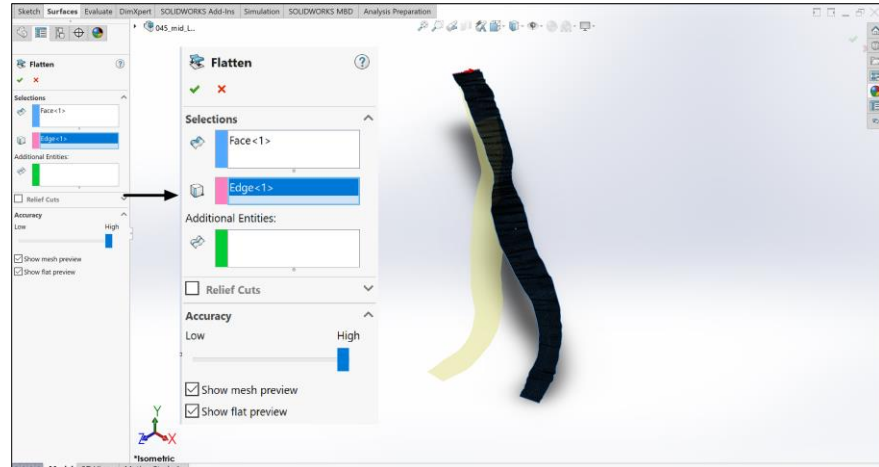


FIGURE 3.14 - Flatten Pane Magnified and the Three-Dimensional Surface Being Flattened in SolidWorks

Click the green checkmark under the Flatten pane on the left to confirm the flattening.

- iv. Aligning the Surface. Click Insert → Surface → Move/Copy... to initiate the aligning process. With the Bodies to Move box highlighted in blue, select the flattened surface. With Mate Settings box highlighted in blue, select the flattened surface and the default Front Plane. Ensure Coincident is chosen below the Mate Settings box. The flattened surface will align to the XY-plane, which is shown in process in FIGURE 3.15:

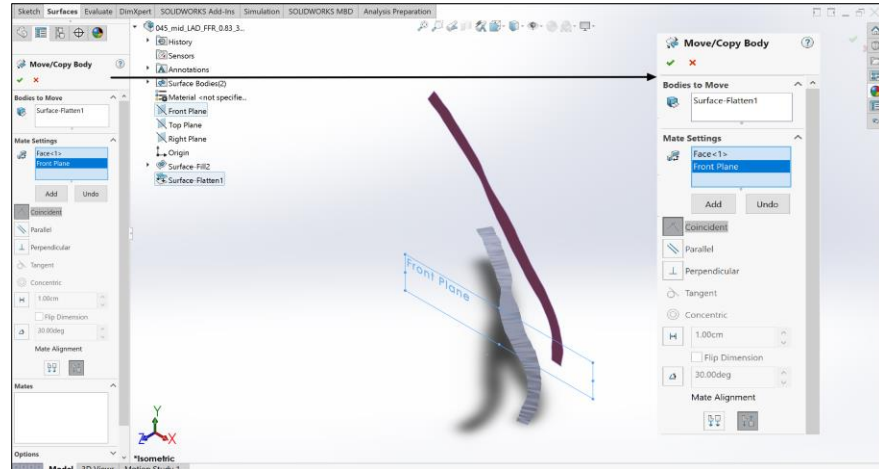


FIGURE 3.15 - Move/Copy Body Pane Magnified and the Two-Dimensional Surface Being Aligned in SolidWorks

Click the green checkmark under the Move/Copy Body pane on the left to confirm the aligning.

- v. Deleting the Three-Dimensional Surface. Two objects are visible at this point, but the remaining three-dimensional surface must be deleted. Opening the Surface Bodies folder in the hierarchy pane, right-click the filled surface and click Delete/Keep Body... to open the Delete/Keep Body... pane. Ensure the Delete/Keep Body... pane shows Delete Bodies under Type and the Bodies to delete box highlighted in blue shows the filled surface. This process is shown in FIGURE 3.16:

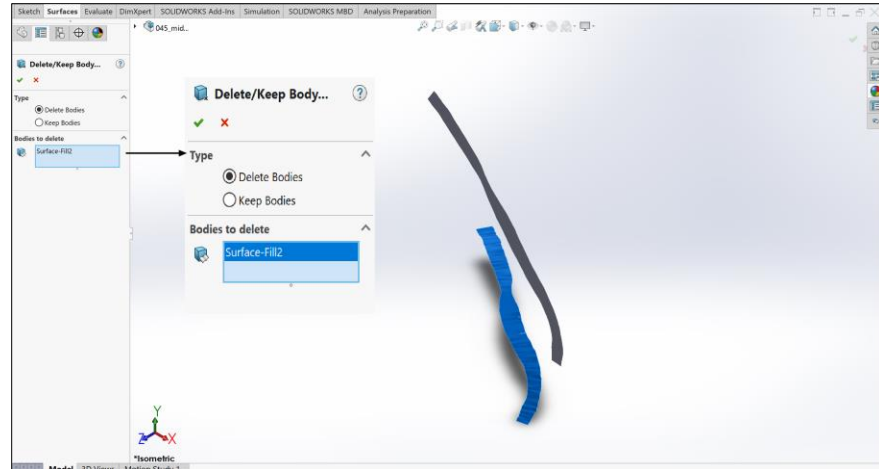


FIGURE 3.16 - Delete/Keep Body... Pane Magnified and the Three-Dimensional Surface Being Deleted in SolidWorks

Click the green checkmark under the Delete/Keep Body... pane on the left to confirm the deletion. Only a two-dimensional slice oriented on the XY-plane remains.

- vi. Saving As a STEP File. The two-dimensional slice must be saved as a STEP file for proper analysis hereafter. Click File → Save As. In the Save As window, ensure the STEP AP203 file format is chosen. Click “Save” in the Save As window to create a two-dimensional STEP file for Slice 1.
- vii. Repeat for Slice 2. Repeat the above steps in the SolidWorks subsection for the three-dimensional Slice 2 STEP file generated from SpaceClaim. As a result, two separate STEP files representing the filled, flattened, and aligned two-dimensional arterial slices have been created and are in position for Meshing treatment.

2. Mesh Generation

The two generated arterial slices were meshed using the software of ANSYS Meshing. The following steps describe how to create a suitable mesh:

a. Preliminary Setup. Workbench and Meshing are used to structure the introductory arrangement of mesh generation.

i. New Fluid Flow (Fluent) Module and Importing the Geometry File. In Workbench, drag a new Fluid Flow (Fluent) module from the Toolbox pane to the Project Schematic pane. This module is added next to the previously inserted Geometry module. FIGURE 3.17 displays the Project Schematic setup:

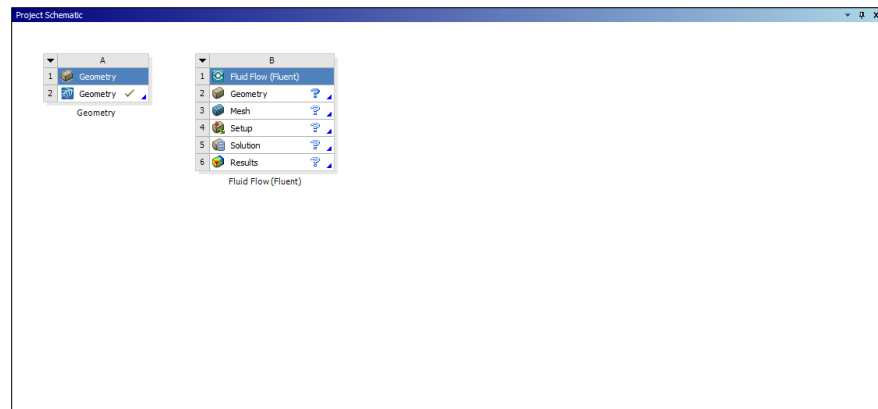


FIGURE 3.17 - Project Schematic Pane with Geometry and Fluid Flow (Fluent) Modules in Workbench

To import the proper geometry, right-click the Geometry cell in the Fluid Flow (Fluent) module and click Import Geometry → Browse... and browse to one of the two-dimensional arterial slice STEP files created in SolidWorks. Click “Open” in the Open window. A green checkmark will display in the Geometry cell to confirm the importing.

ii. Initial Meshing Preferences. Open Meshing by double-clicking the Mesh cell in the Fluid Flow (Fluent) Module. In Meshing, click Mesh from the Outline pane on the left. The Details of “Mesh” pane will display under the Outline pane. In the Details of “Mesh” pane, ensure Fluent is chosen as the Solver Preference under the Defaults group. In the same pane, choose “Proximity and Curvature” for Size Function and “Fine” for Relevance Center under the Sizing group. These preferences are highlighted in FIGURE 3.18:

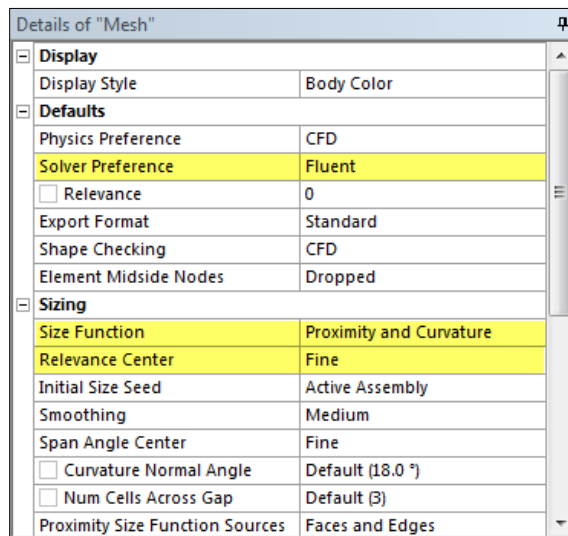


FIGURE 3.18 - Details of “Mesh” Pane Preferences in Meshing

b. Meshing Controls. Controls must be applied to construct a working mesh.

i. Body Sizing. Right-click Mesh from the Outline pane and click Insert.

FIGURE 3.19 displays the Insert controls:

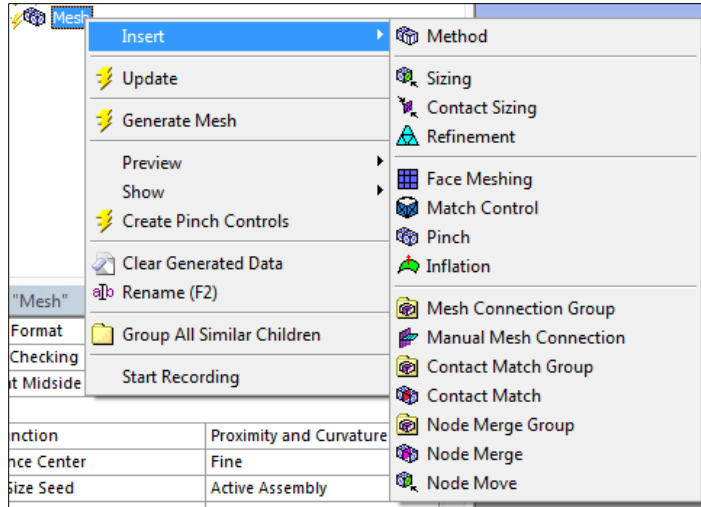


FIGURE 3.19 - Insert Controls in Meshing

Click Sizing. The Details of “Mesh” pane will convert to the Details of “Sizing” - Sizing pane. Geometry under the Scope group will display No Selection. To select the proper geometry, click the green Body tool from the ribbon and select the slice in the Geometry space. The slice will turn green. In the Details of “Sizing” - Sizing pane, click Apply for Geometry under the Scope group. FIGURE 3.20 displays the resulting pane, which converts to “Body Sizing” after clicking Apply:

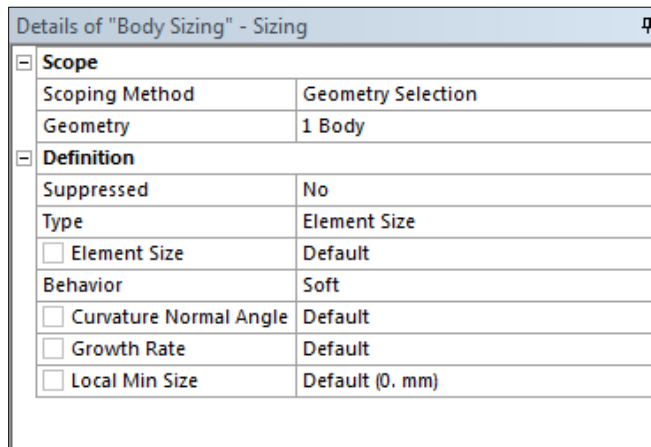


FIGURE 3.20 - Details of “Body Sizing” - Sizing Pane in Meshing

Importantly, Geometry under the Scope group displays “1 Body,” confirming proper selection has been made.

ii. Inflation. Right-click Mesh from the Outline pane again and click Insert. As seen in FIGURE 3.19, click Inflation. Geometry under the Scope group and Boundary under the Definition group will display No Selection. To select the proper geometry, click the green Face tool from the ribbon and select the slice face in the Geometry space. The slice face will turn green. In the Details of “Inflation” - Inflation pane, click Apply for Geometry under the Scope group. In a similar manner, click the green Edge tool from the ribbon and select the two wall edges of the slice in the Geometry space. The two wall edges of the slice will turn green. In the Details of “Inflation” - Inflation pane, click Apply for Boundary under the Definition group. With this, change the number of inflation layers to “10” by toggling to the number for Maximum Layers under the Definition group. FIGURE 3.21 displays the resulting pane:

Details of "Inflation" - Inflation	
Scope	
Scoping Method	Geometry Selection
Geometry	1 Face
Definition	
Suppressed	No
Boundary Scoping Method	Geometry Selection
Boundary	2 Edges
Inflation Option	Smooth Transition
<input type="checkbox"/> Transition Ratio	Default (0.272)
<input type="checkbox"/> Maximum Layers	10
<input type="checkbox"/> Growth Rate	1.2
Inflation Algorithm	Pre

FIGURE 3.21 - Details of “Inflation” - Inflation Pane in Meshing

Importantly, Geometry under the Scope group displays “1 Face,” Boundary under the Definition group displays “2 Edges,” and the Maximum Layers under the Definition group displays 10, confirming proper selections and settings have been made.

iii. Named Selections. For downstream Fluent processing, Named Selections must be applied to the inlet, outlet, wall, and interior of the slice. To define the inlet, begin by clicking the green Edge tool from the ribbon and selecting the larger of the two boundary edges. Right-click and choose Create Named Selection. Name the selection as inlet in the Selection Name window, ensure Apply selected geometry is ticked, and click “OK.” FIGURE 3.22 displays the process of creating a Named Selection for the inlet:

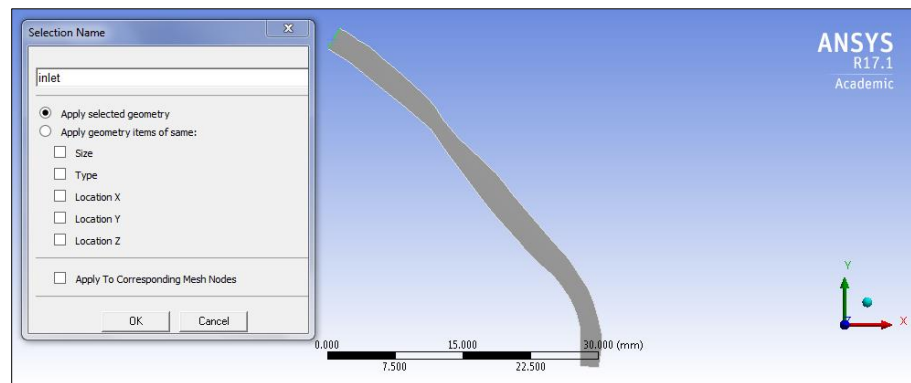


FIGURE 3.22 - Creating a Named Selection for the Inlet in Meshing

Repeat the process for the outlet, wall, and interior. The outlet is the other boundary edge, while the wall is defined by the same wall edges as in the Inflation steps. The interior is the face of the slice, and it is named “artery” for clarity. This, and the remaining distribution of color-coded Named Selections, is shown in FIGURE 3.23:

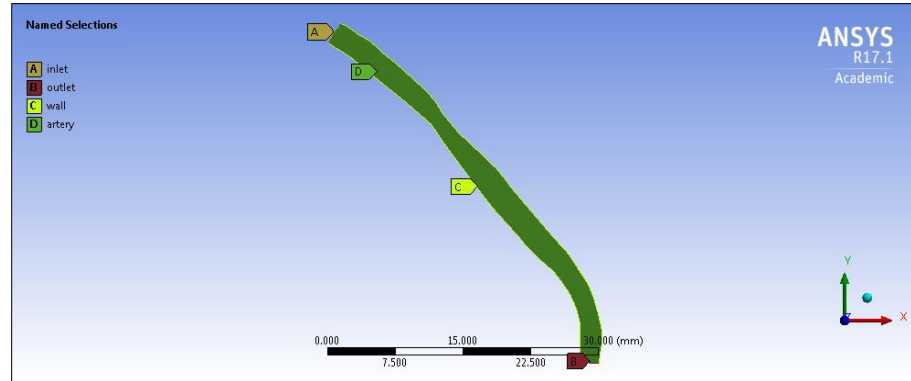


FIGURE 3.23 - Named Selection Distribution in Meshing

c. Processing and Requirements. Proper processing to achieve set mesh requirements must occur to create a final mesh suitable for downstream use.

i. Mesh Construction and Mesh Count. Begin the meshing process by clicking Generate Mesh at the top of the ribbon. After processing, click Show Mesh at the top of the ribbon to display the mesh. Upon inspection, inflation layers line the wall and a mesh has been created, but the mesh count must be checked for acceptable resolution. To begin the check, click Mesh from the Outline pane on the left. The Details of “Mesh” pane will display under the Outline pane. In the Details of “Mesh” pane, review Elements under the Statistics group. This is highlighted in FIGURE 3.24:

Details of "Mesh"	
<input type="checkbox"/> Curvature Normal Angle	Default (18.0 °)
<input type="checkbox"/> Num Cells Across Gap	Default (3)
Proximity Size Function Sources	Faces and Edges
<input type="checkbox"/> Min Size	Default (7.026e-003 mm)
<input type="checkbox"/> Proximity Min Size	Default (7.026e-003 mm)
<input type="checkbox"/> Max Face Size	Default (0.70260 mm)
<input type="checkbox"/> Max Tet Size	Default (1.40520 mm)
<input type="checkbox"/> Growth Rate	Default (1.20)
Automatic Mesh Based Defeaturing	On
<input type="checkbox"/> Defeaturing Tolerance	Default (3.513e-003 mm)
Minimum Edge Length	2.09320 mm
<input checked="" type="checkbox"/> Inflation	
<input checked="" type="checkbox"/> Assembly Meshing	
<input checked="" type="checkbox"/> Advanced	
<input checked="" type="checkbox"/> Statistics	
<input type="checkbox"/> Nodes	1746
<input checked="" type="checkbox"/> Elements	1649
Mesh Metric	None

FIGURE 3.24 - Checking Mesh Count in the Details of “Mesh” Pane in Meshing

The number associated with Elements represents the mesh count. This value should be no less than 20,000. The mesh count is increased by decreasing the Element Size under the Definition section in the Details of “Body Sizing” - Sizing pane, which is seen in FIGURE 3.20. Typically, an Element Size of 0.10 mm will produce a mesh count near 20,000. After changing the Element Size value in FIGURE 3.20, click Generate Mesh again, inspect the mesh using Show Mesh, and check the mesh count in the Details of “Mesh” Pane for a value of at least 20,000.

- ii. Repeat for Slice 2. Repeat the above steps in the Mesh Generation subsection for the other two-dimensional arterial slice STEP file created in SolidWorks. As a result, two separate modules containing the meshed slices have been created and are in position for Fluent treatment.

3. Fluent Case Processing

Blood flow through the two meshed arterial slices was simulated using the software of ANSYS Fluent. The following steps describe how to run a suitable case:

a. Preliminary Setup. Workbench is used to structure the introductory arrangement of Fluent cases.

i. Opening Fluent Launcher and Fluent. In Workbench, double-click the Setup cell in the previously inserted Fluid Flow (Fluent) Module. Fluent Launcher will open. Verify that the default settings restrict 2D for Dimension, and ensure the setting highlighted in FIGURE 3.25 is followed:

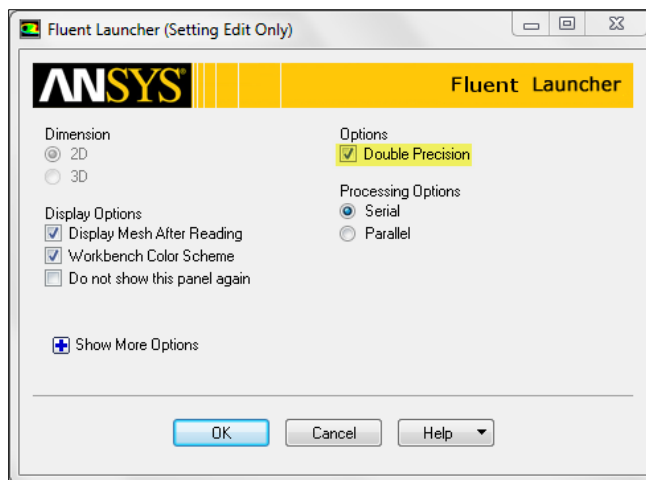


FIGURE 3.25 - Fluent Launcher Window in Workbench

Click “OK” to open Fluent.

b. Setup. The Setup group in the Tree hierarchy arranges the most common system setup tasks.

i. General. Click General in the Tree hierarchy to display the General pane, and ensure the settings highlighted in FIGURE 3.26 are followed:

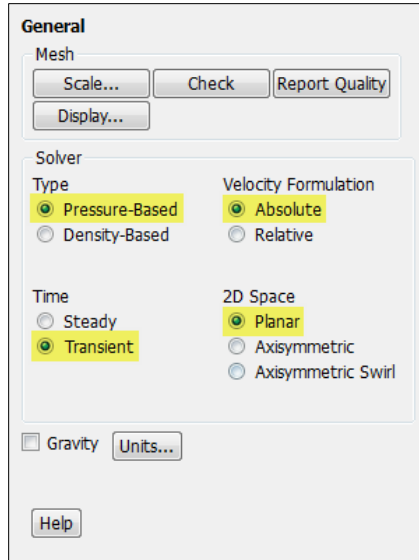


FIGURE 3.26 - General Pane in Fluent

ii. Models. Click Models in the Tree hierarchy to display the Models pane, and select Multiphase - Off. To activate this model, click “Edit...” at the bottom of the Models pane. The Multiphase Model window will open, where the settings highlighted in FIGURE 3.27 should be applied:

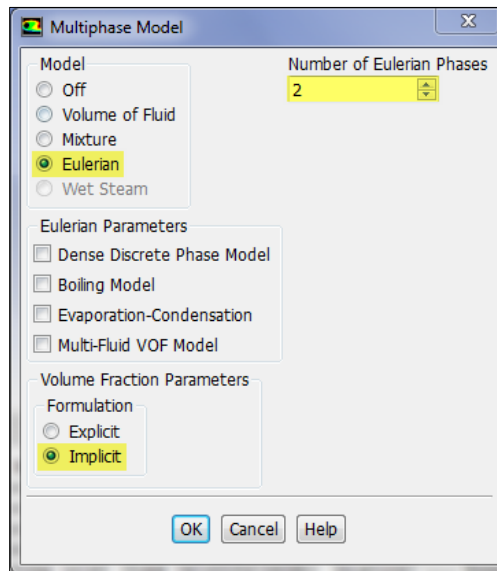


FIGURE 3.27 - Multiphase Model Window in Fluent

Click “OK” to activate the model. In the Models pane, activation is complete if the model displays “Multiphase - Eulerian.” With this, ensure that the Viscous model displays the default “Viscous - Laminar.”

iii. Materials. Click Materials in the Tree hierarchy to display the Materials pane. Default fluid and solid materials of air and aluminum, respectively, will be present. Air will be replaced with the two phases of plasma and red blood cells, while aluminum will be kept unchanged. With Fluid highlighted, click “Create/Edit...” at the bottom of the Materials pane. The Create/Edit Materials window will open, where the settings highlighted in FIGURE 3.28 for plasma should be applied:

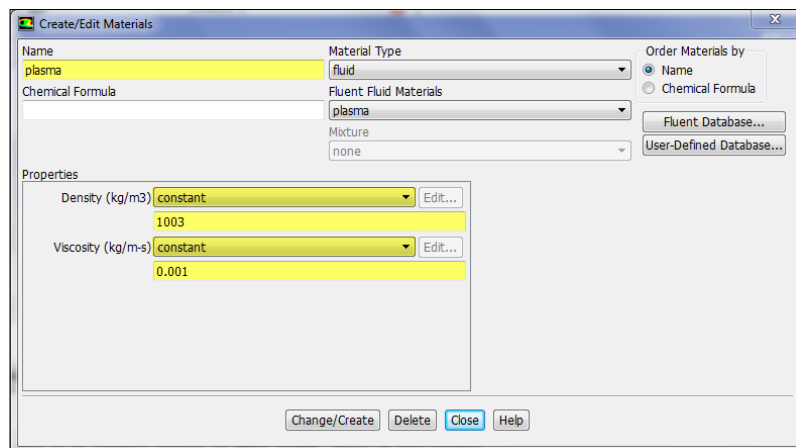


FIGURE 3.28 - Create/Edit Materials Window for Plasma in Fluent

In FIGURE 3.28, a density of $1,003 \text{ kg m}^{-3}$ is used, and a viscosity of $0.001 \text{ kg m}^{-1} \text{ s}^{-1}$ is used. Similar steps may be taken to define red blood cells as a material. For red blood cells, however, a density of $1,096 \text{ kg m}^{-3}$ is used, and viscosity is inserted by changing its drop-down to “user-defined” and clicking “Edit...” to the right of it. The `car_yas_visc` option

is chosen as the viscosity in the User-Defined Functions window, as shown in FIGURE 3.29:

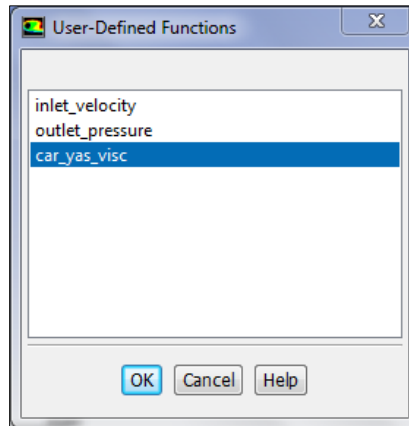


FIGURE 3.29 - User-Defined Functions Window with car_yas_visc

Viscosity Selection for Red Blood Cells in Fluent

Click “OK” to activate the model, and click “Close” in the Create/Edit Materials window. It is noted that the car_yas_visc option will only be available after a user-defined function is interpreted, as in FIGURE 3.33.

- iv. Defining Phases. Phases are defined by clicking List/Show All... above Phases under the Setting Up Physics tab in the ribbon. The Phases window will open, as shown in FIGURE 3.30:

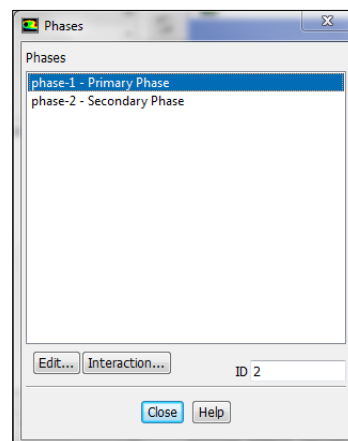


FIGURE 3.30 - Phases Window in Fluent

Ensure the primary (phase-1) and secondary (phase-2) phases are plasma and red blood cells, respectively, by clicking “Edit...” and choosing the proper material from the Phase Material drop-down. Red blood cells require additional settings for phasic definition. As such, enable Granular in the Secondary Phase window to reveal property input. This is shown in FIGURE 3.31, where the highlighted settings should be applied:

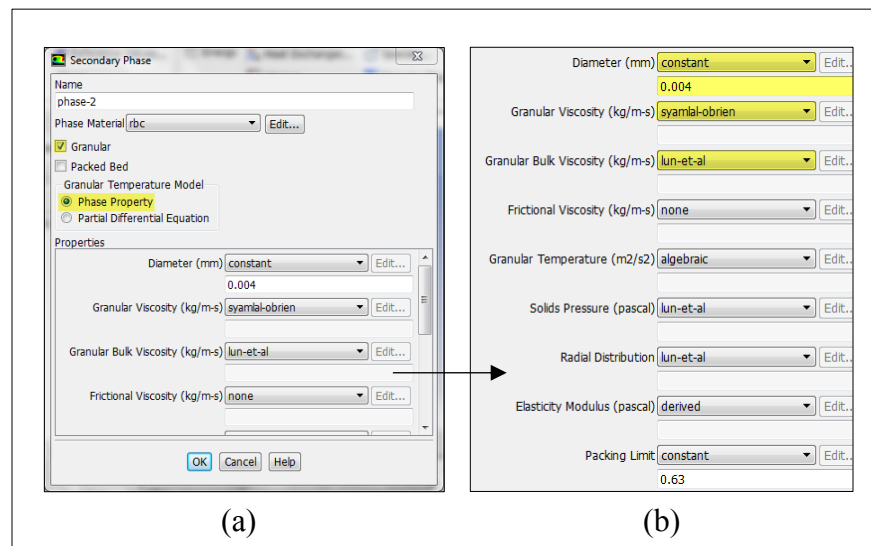


FIGURE 3.31 - Secondary Phase Window in (a) General and with the (b) Granular Properties Magnified in Fluent

Phasic interaction settings are changed by clicking “Interaction...” at the bottom of the Phases window seen in FIGURE 3.30. Interaction changes for virtual mass, lift, collisions, mass, surface tension, and interfacial area are available, but the drag coefficient is the only item in need of modification. Keeping all other interactions default, FIGURE 3.32 displays the highlighted setting to be changed for the drag coefficient:

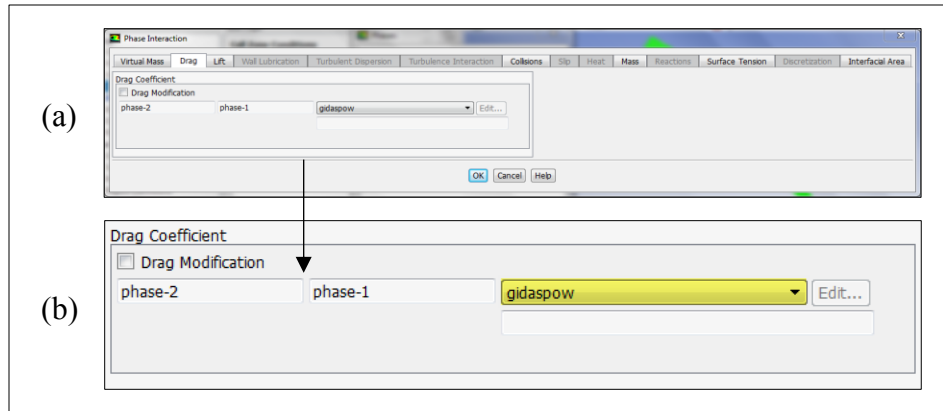


FIGURE 3.32 - Phase Interaction Window in (a) General and with the (b) Drag Coefficient Settings Magnified in Fluent

v. Interpreting a User-Defined Function and Setting User-Defined Scalars.

To permit use of scalars, a user-defined function must first be read by Fluent. Click Functions → Interpreted... above User-Defined under the User-Defined tab in the ribbon. The Interpreted UDFs window will open. Click Browse... and locate the proper source code file. The resulting window is shown in FIGURE 3.33:

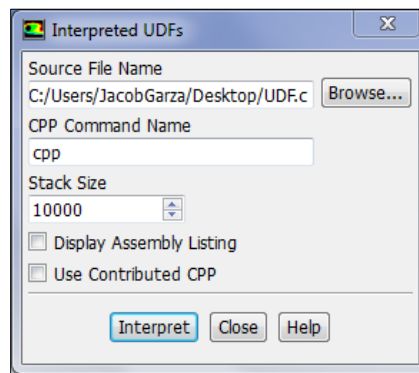


FIGURE 3.33 - Interpreted UDFs Window in Fluent

Click “Interpret” in the Interpreted UDFs window and then click “Close.” With this, scalar definition begins by clicking Scalars... above User-Defined under the User-Defined tab in the ribbon. The User-

Defined Scalars window will open, where the settings highlighted in FIGURE 3.34 should be applied:

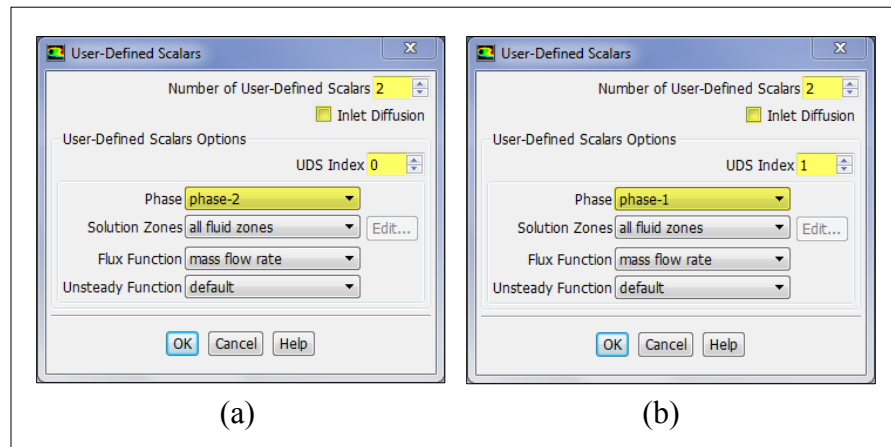


FIGURE 3.34 - User-Defined Scalars Window for (a) Red Blood Cells and (b) Plasma in Fluent

Click “OK” to confirm the addition of the two scalars. Viewing FIGURE 3.34, it is stated that phase-2 now represents red blood cells and Scalar0, while phase-1 now represents plasma and Scalar1.

- vi. Mean Ages of the Phases Using User-Defined Scalars - Scalar0. It is initially noted that this subsection demonstrates the steps necessary for mean age calculation setup with respect to Scalar0, with analogous images of Scalar1 setup displayed in the succeeding subsection. Recognizing this, the material properties of red blood cells must be updated to reflect scalar impact. Reopen the Create/Edit Materials window for red blood cells, which will now include the UDS Diffusivity option highlighted in FIGURE 3.35:

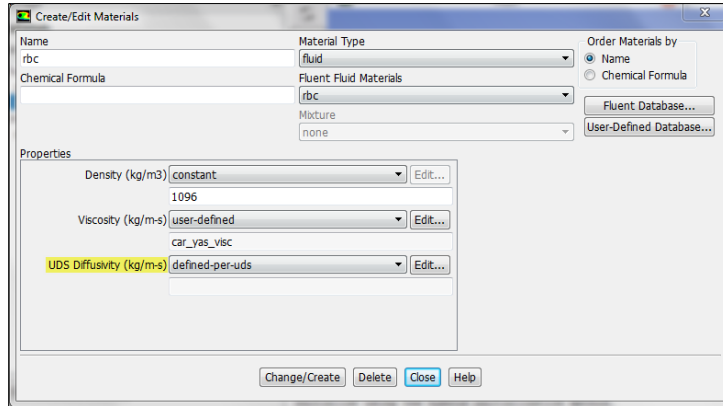


FIGURE 3.35 - Updated Create/Edit Materials Window for Scalar0 in
Fluent

UDS diffusivity is inserted by changing its drop-down to “defined-per-uds” and clicking “Edit...” to the right of it. A coefficient is entered in the UDS Diffusion Coefficients window, as shown highlighted in FIGURE 3.36:

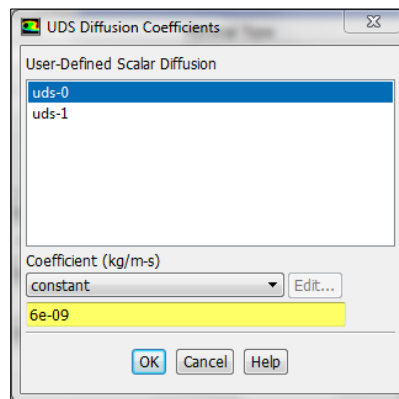


FIGURE 3.36 - UDS Diffusion Coefficients Window for Scalar0 in
Fluent

Click “OK” to confirm the coefficient, and click “Change/Create” and then “Close” in the Create/Edit Materials window. With this, to apply the scalar to the proper zone of geometry, click Cell Zone Conditions in

the Tree hierarchy to display the Cell Zone Conditions pane. With the phase of red blood cells (phase-2) chosen in the Phase drop-down in the pane, click “Edit...” to open the Fluid window. Enable Source Terms and click “Edit...” to the right of User Scalar 0 under the Source Terms tab. This will open the User Scalar 0 sources window. The same magnitude of density for red blood cells used previously (1,096) should be entered as the constant value. This process, with proper settings highlighted, is shown in FIGURE 3.37:

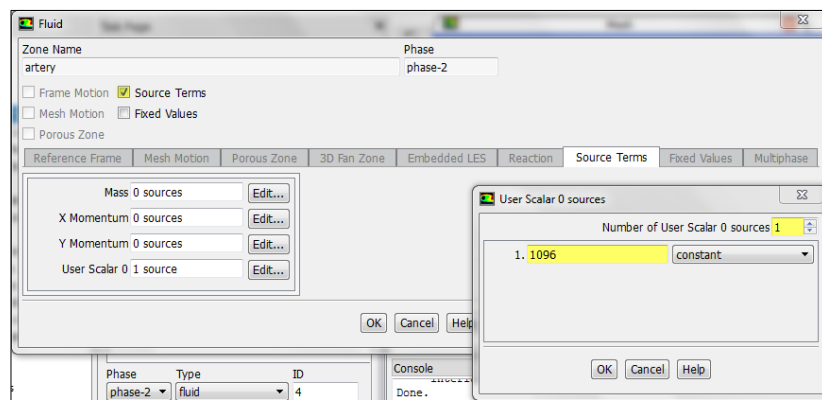


FIGURE 3.37 - Fluid and User Scalar 0 Sources Windows for Scalar0 in
Fluent

Click “OK” in both windows to confirm scalar zone application. Finally, to apply the scalar in the boundary conditions, click Boundary Conditions in the Tree hierarchy to display the Boundary Conditions pane. With phase-2 still chosen in the Phase drop-down in the pane, select the inlet boundary and click “Edit...” to open the Velocity Inlet window. Three tabs of options are available, and the settings to be changed are shown highlighted in FIGURE 3.38:

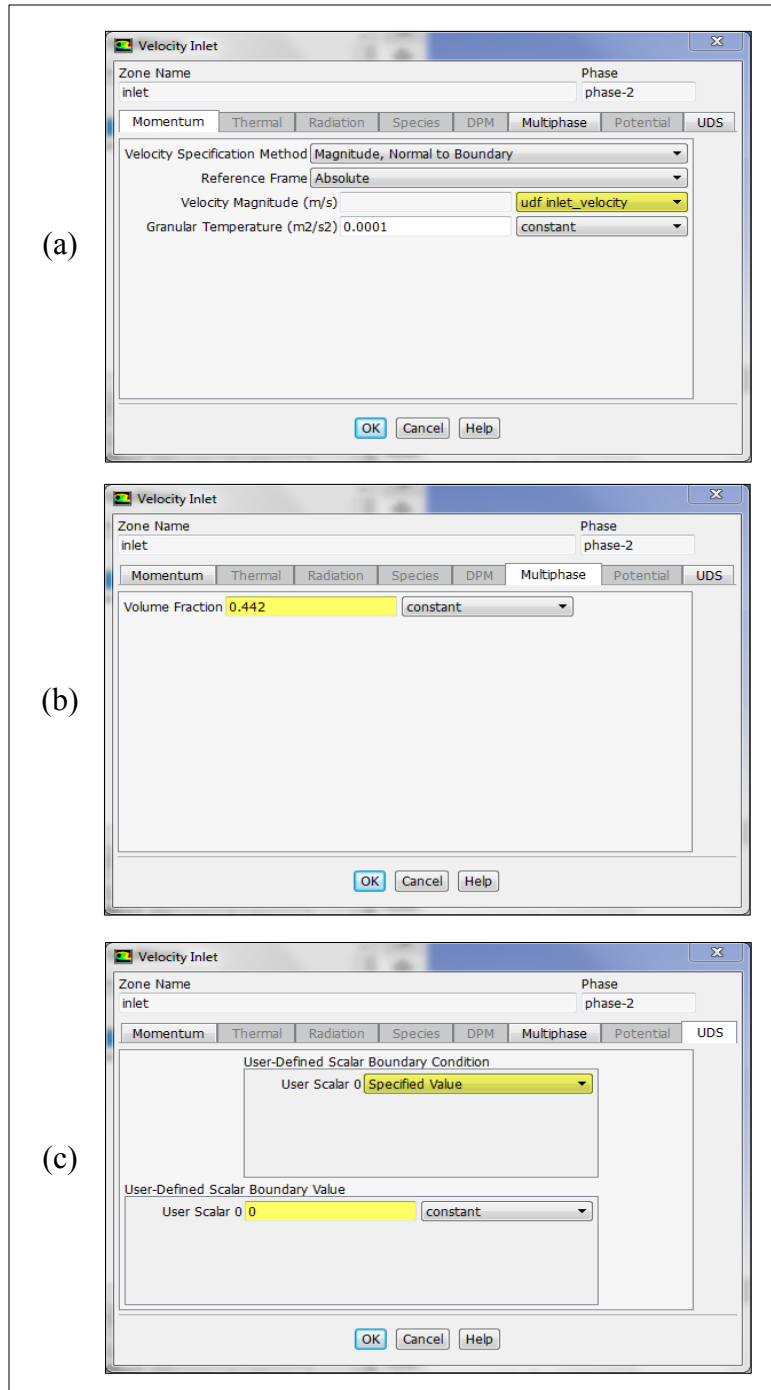


FIGURE 3.38 - Velocity Inlet Window for Scalar0 Displaying (a)

Momentum, (b) Multiphase, and (c) UDS Settings in Fluent

Click “OK” to confirm the inlet boundary condition. With phase-2 still chosen in the Phase drop-down in the Boundary Conditions pane, select

the outlet boundary and click “Edit...” to open the Pressure Outlet window. Two tabs of options are available, and the default settings to ensure are shown in FIGURE 3.39:

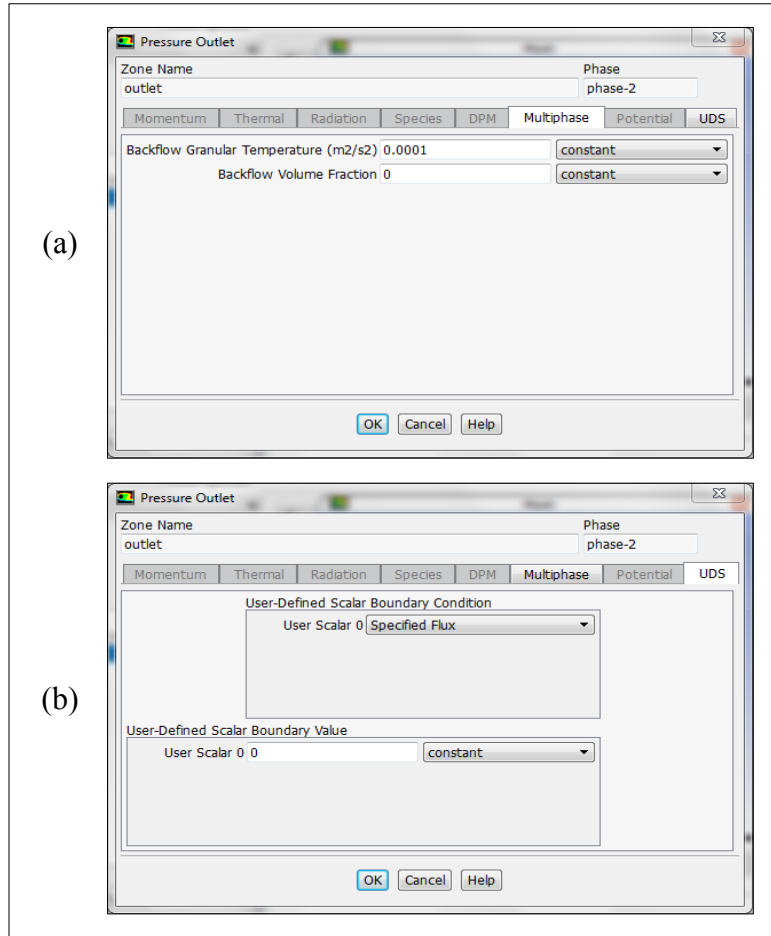


FIGURE 3.39 - Pressure Outlet Window for Scalar0 Displaying (a) Multiphase and (b) UDS Settings in Fluent

Click “OK” to confirm the outlet boundary condition.

- vii. Mean Ages of the Phases Using User-Defined Scalars - Scalar1. While previous steps have defined the scalar for red blood cells, similar steps may be taken for scalar definition of plasma. FIGURES 3.40–44 display Scalar1 analogs of the preceding steps of Scalar0 definition:

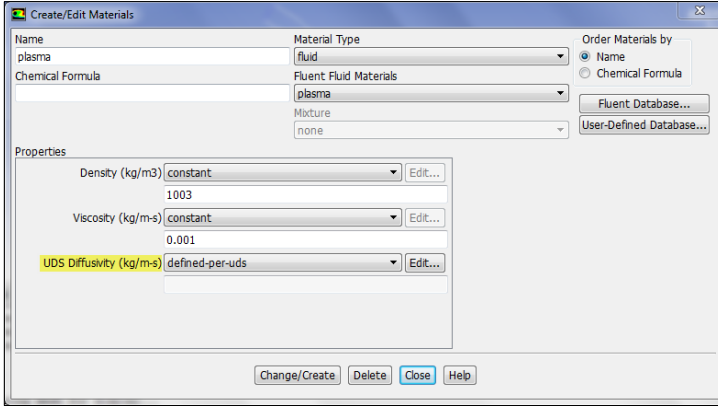


FIGURE 3.40 - Updated Create/Edit Materials Window for Scalar1 in
Fluent

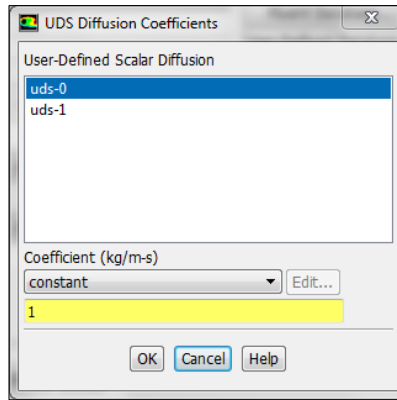


FIGURE 3.41 - UDS Diffusion Coefficients Window for Scalar1 in
Fluent

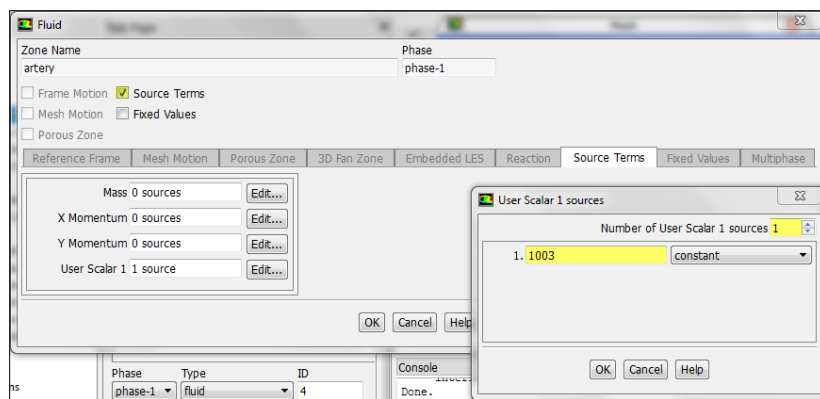


FIGURE 3.42 - Fluid and User Scalar 1 Sources Windows for Scalar1 in
Fluent

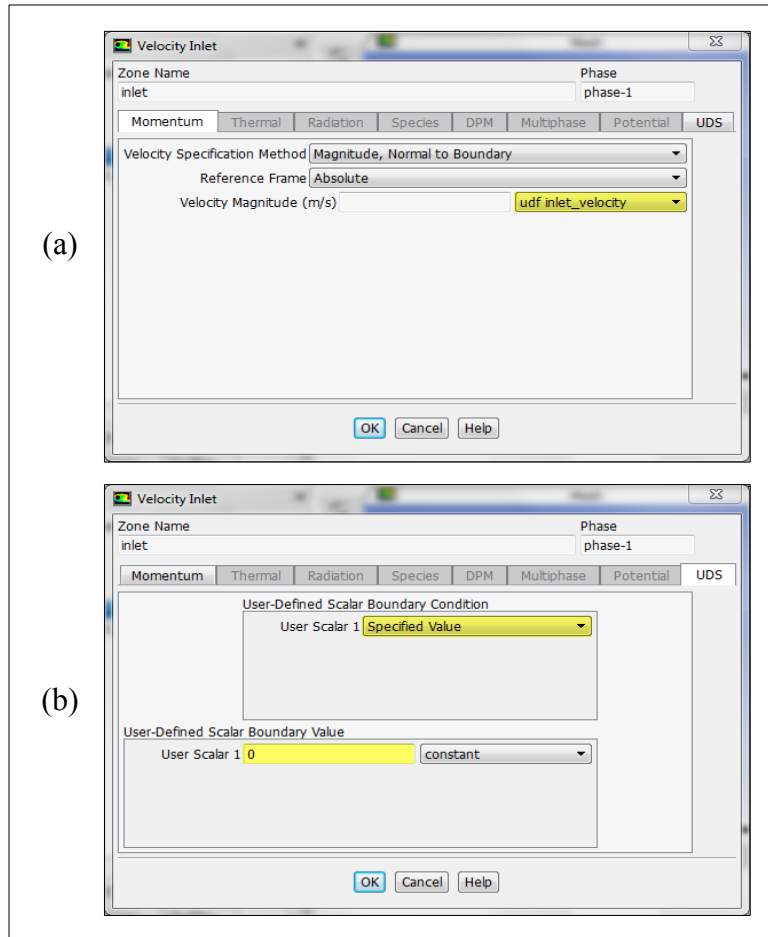


FIGURE 3.43 - Velocity Inlet Window for Scalar1 Displaying (a) Momentum and (b) UDS Settings in Fluent

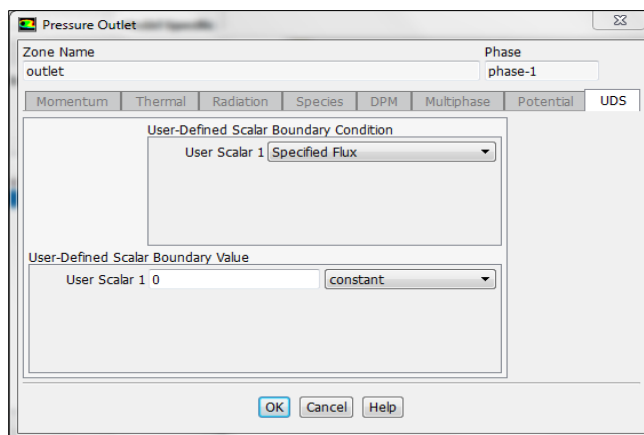


FIGURE 3.44 - Pressure Outlet Window for Scalar1 Displaying UDS Settings in Fluent

c. Solution. The Solution group in the Tree hierarchy arranges solution setup and calculation task direction.

i. Solution Methods. Click Solution Methods in the Tree hierarchy to display the Solution Methods pane, and ensure the settings highlighted in FIGURE 3.45 are followed:

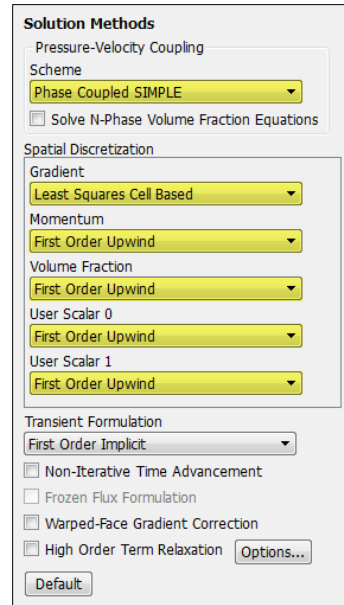


FIGURE 3.45 - Solution Methods Pane in Fluent

ii. Solution Controls. Click Solution Controls in the Tree hierarchy to display the Solution Controls pane, and ensure the settings highlighted in FIGURE 3.46 are followed:

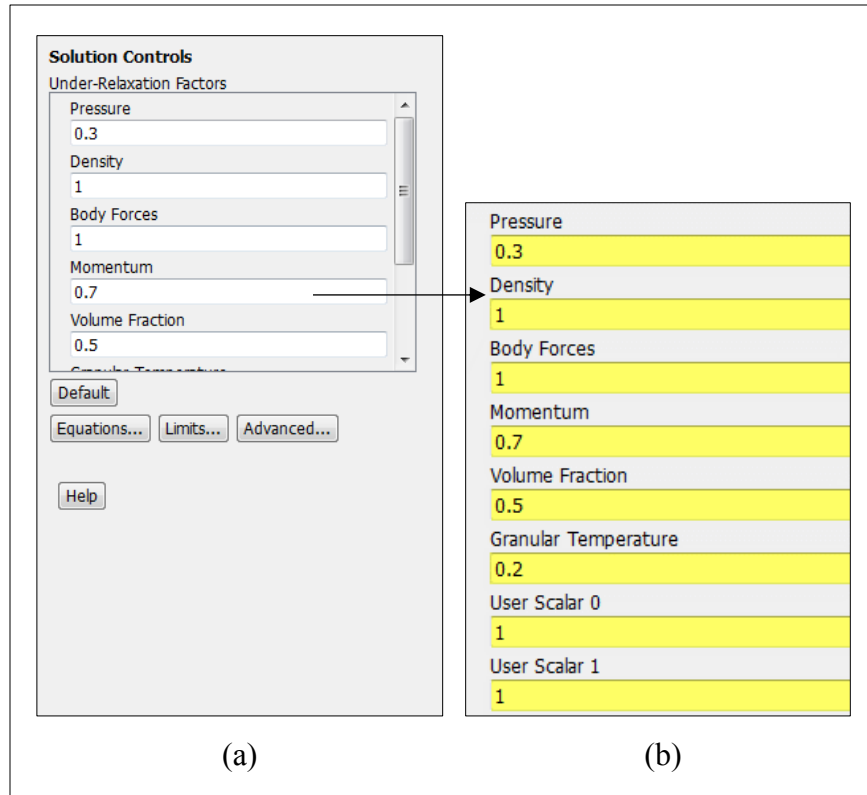


FIGURE 3.46 - Solution Controls Pane in (a) General and with the (b) Under-Relaxation Factors Magnified in Fluent

It is noted that the value of User Scalar 0 shown in FIGURE 3.46(b) may need infrequent reduction if divergence errors emerge. As such, this value may be halved until divergence is mitigated and a solution is calculated.

- iii. Monitors. Click Monitors in the Tree hierarchy to display the Monitors pane. Select Residuals - Print, Plot under Residuals, Statistic and Force Monitors in the pane, and click "Edit..." below it. The Residual Monitors window will open, where the settings highlighted in FIGURE 3.47 should be applied:

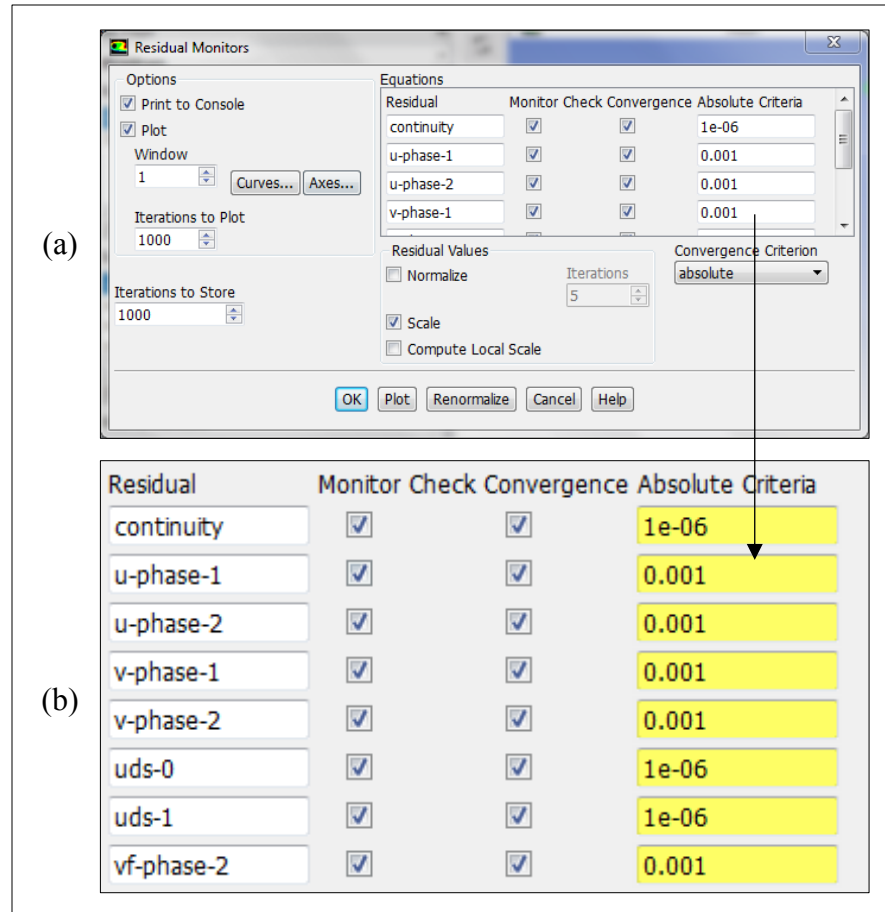


FIGURE 3.47 - Residual Monitors Window in (a) General and with the (b) Equations Magnified in Fluent

Click “OK” to confirm the residual monitor settings.

- iv. Solution Initialization. Click Solution Initialization in the Tree hierarchy to display the Solution Initialization pane. With Hybrid Initialization chosen from the Initialization Methods options, click “Initialize.” Appropriate starting values are generated for necessary system components, but the initial zero values of the scalars must be changed manually to further assist in solution convergence. As such, select Standard Initialization from the Initialization Methods options,

and apply the nonzero values highlighted in FIGURE 3.48 for the scalars:

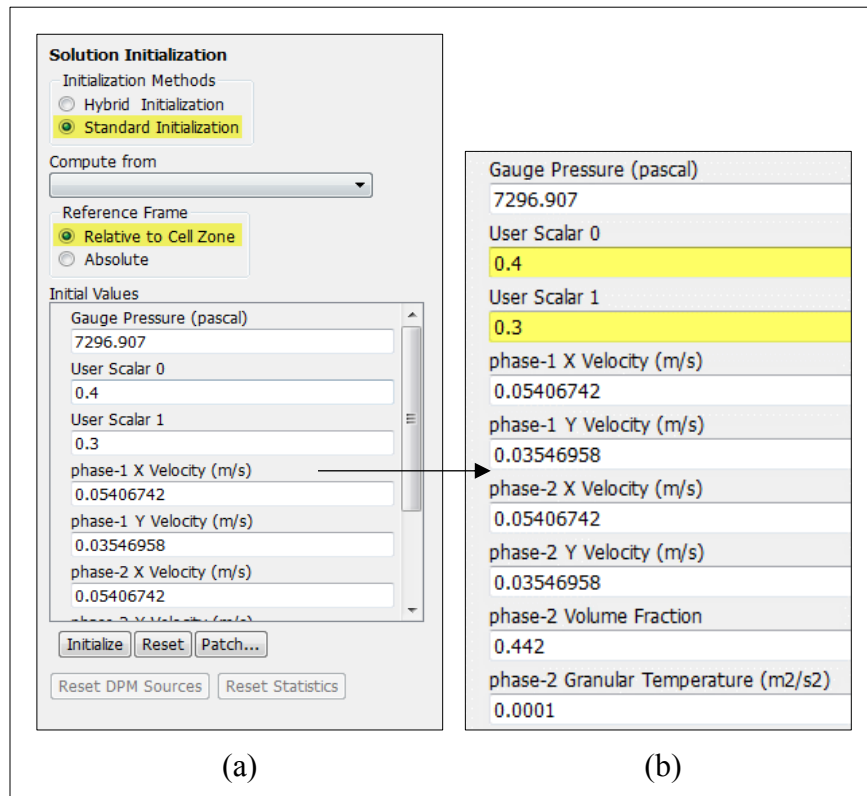


FIGURE 3.48 - Solution Initialization Pane in (a) General and with the (b) Initial Values Magnified in Fluent

Click “Initialize” again to prime the system for solution calculation.

- v. Run Calculation. Click Run Calculation in the Tree hierarchy to display the Run Calculation pane, where the settings highlighted in FIGURE 3.49 should be applied:

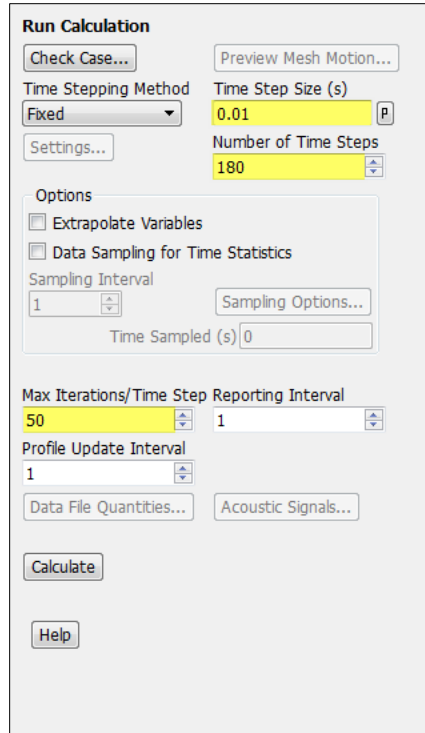


FIGURE 3.49 - Run Calculation Pane in Fluent

Click “Calculate” to begin solution calculation.

IV. RESULTS AND DISCUSSION

A. Scope of Investigated Patient Numbers, Source Renderings, and Created Slices

Results are presented for 10 patient cases, five below and five above the *FFR* threshold of 0.80 reported by Min et al. (2015) as the value below which a cardiologist intervenes with stent placement to prevent ischemia. The 10 patient cases are listed in TABLE 4.1:

TABLE 4.1

VALUES OF *FFR* AND COMPONENTS OF THE ARTERIAL TREE
REPRESENTING THE PATIENT NUMBERS USED IN THIS INVESTIGATION

Patient Number	<i>FFR</i>	Arterial Tree Component
004	0.76	mid left anterior descending
005	0.75	mid right coronary
017	0.72	left anterior descending
019	0.76	posterior descending
041	0.70	proximal left anterior descending
045	0.83	mid left anterior descending
046	0.98	distal right coronary
058	0.98	proximal left circumflex
061	0.97	mid right coronary
075	0.81	mid left anterior descending

The three-dimensional source renderings of low and high *FFR* used for two-dimensional slicing are shown, respectively, in FIGURES 4.1–5 and FIGURES 4.6–10:

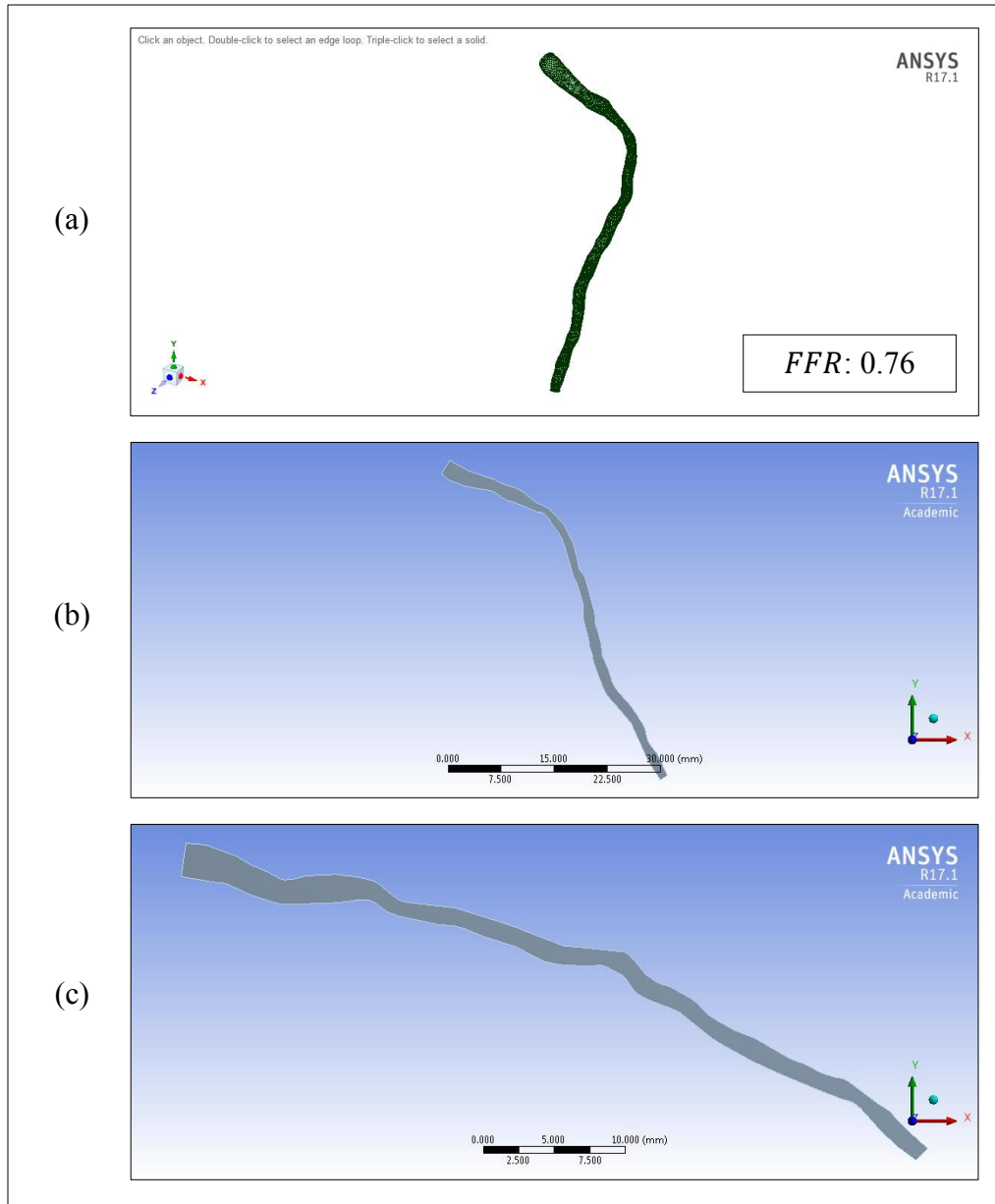


FIGURE 4.1 - Depictions of the (a) Three-Dimensional Source Rendering and Two-Dimensional (b) Slice 1 and (c) Slice 2 for the Artery of Patient 004

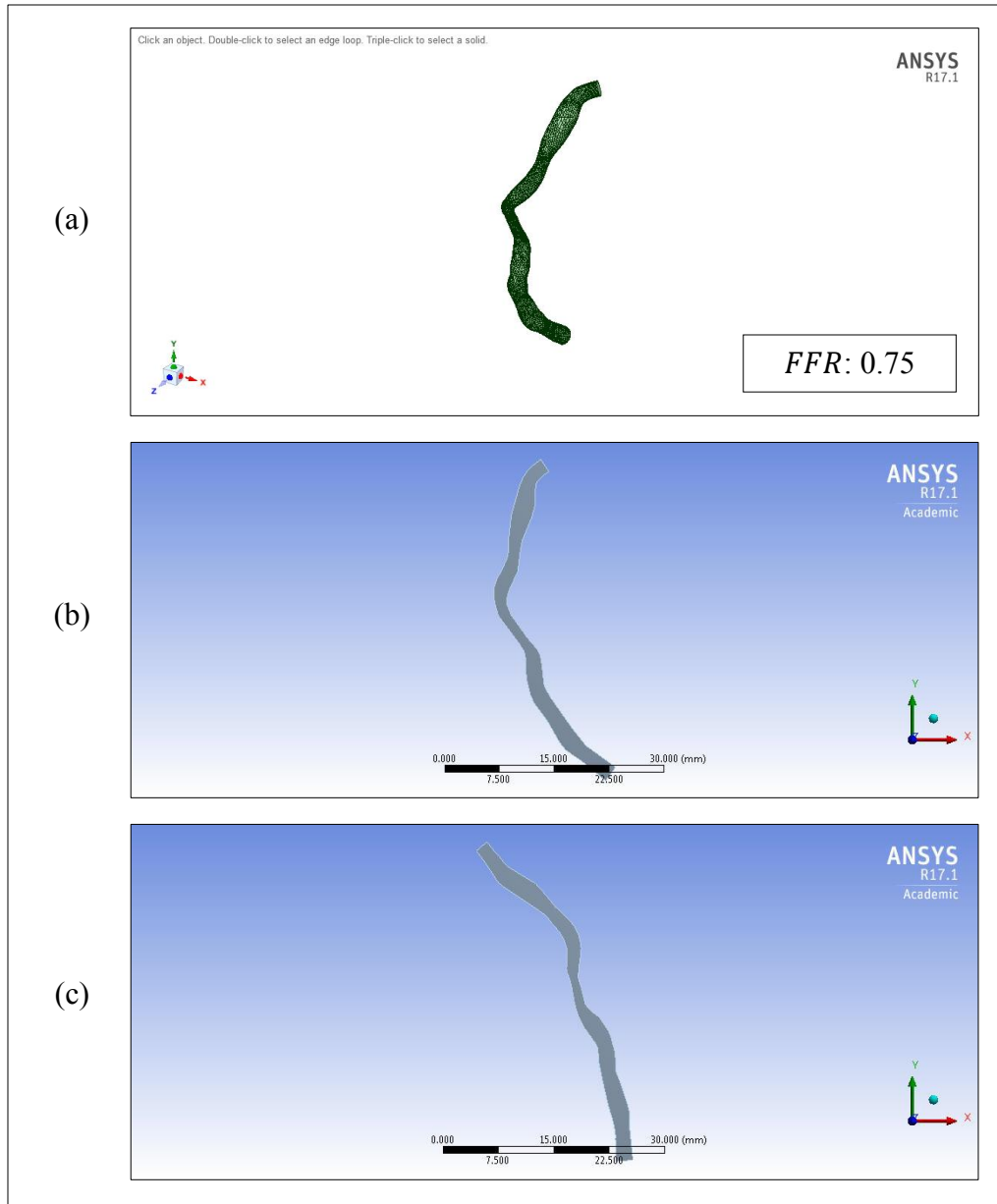


FIGURE 4.2 - Depictions of the (a) Three-Dimensional Source Rendering and Two-Dimensional (b) Slice 1 and (c) Slice 2 for the Artery of Patient 005

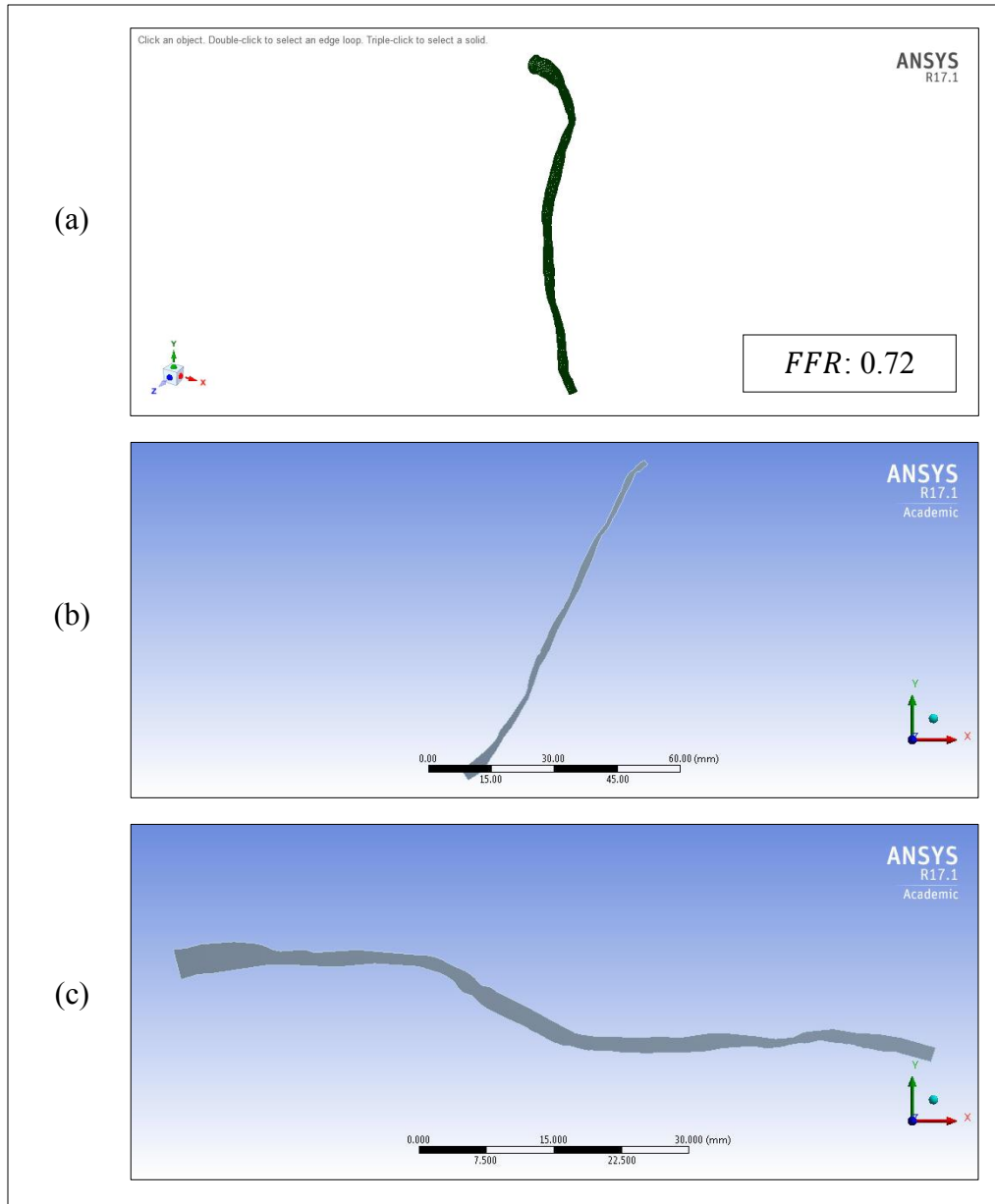


FIGURE 4.3 - Depictions of the (a) Three-Dimensional Source Rendering and Two-Dimensional (b) Slice 1 and (c) Slice 2 for the Artery of Patient 017

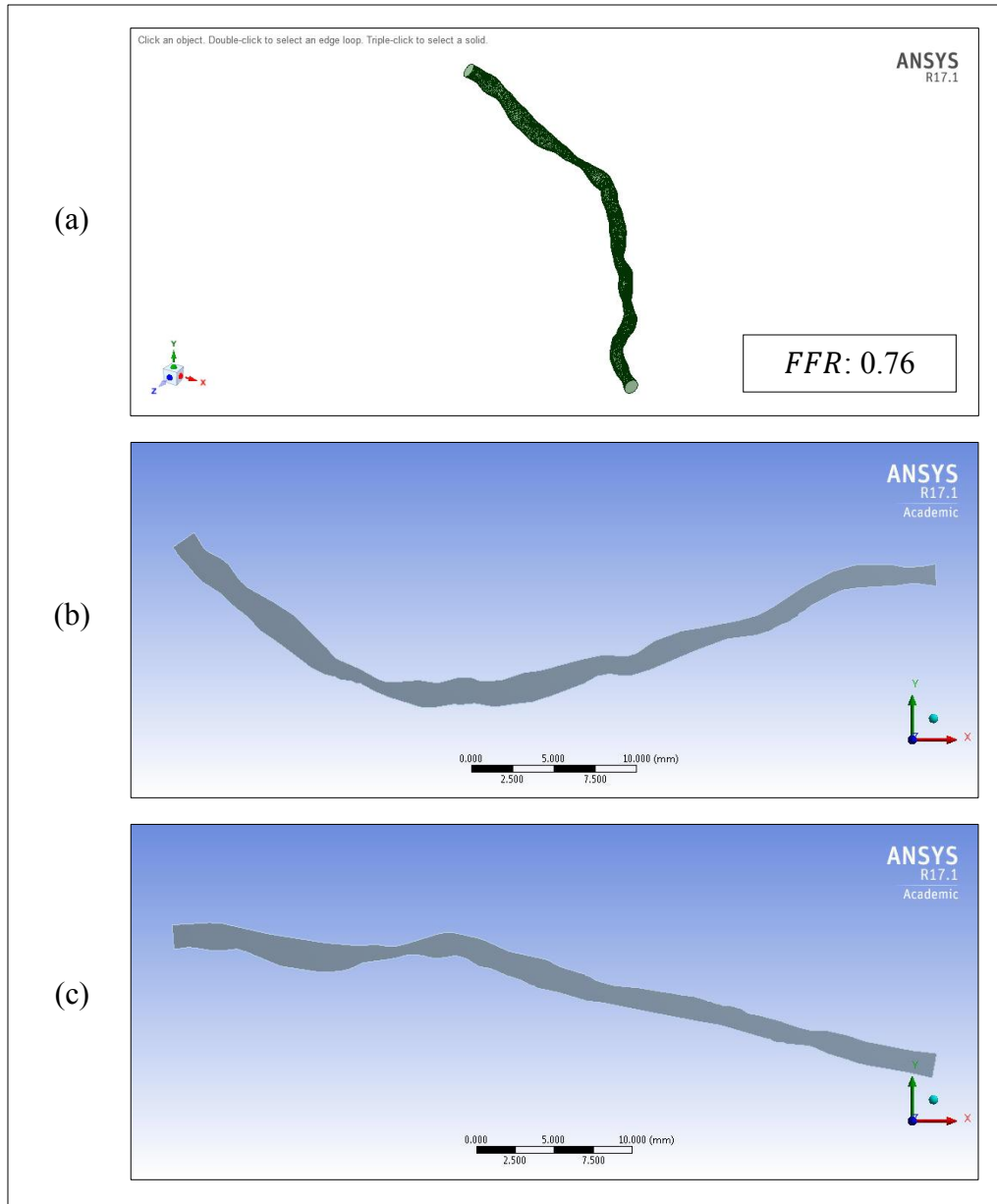


FIGURE 4.4 - Depictions of the (a) Three-Dimensional Source Rendering and Two-Dimensional (b) Slice 1 and (c) Slice 2 for the Artery of Patient 019

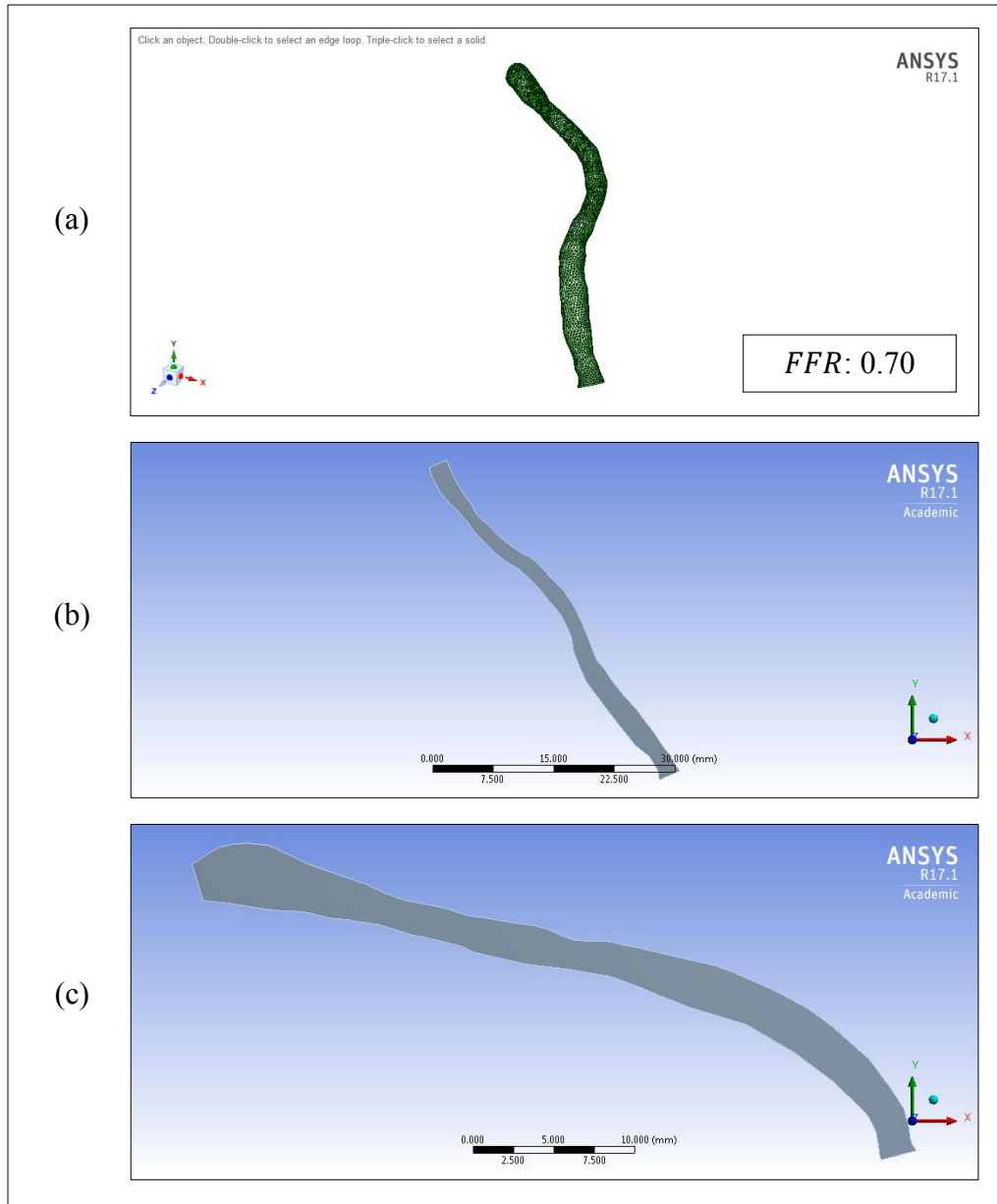


FIGURE 4.5 - Depictions of the (a) Three-Dimensional Source Rendering and Two-Dimensional (b) Slice 1 and (c) Slice 2 for the Artery of Patient 041

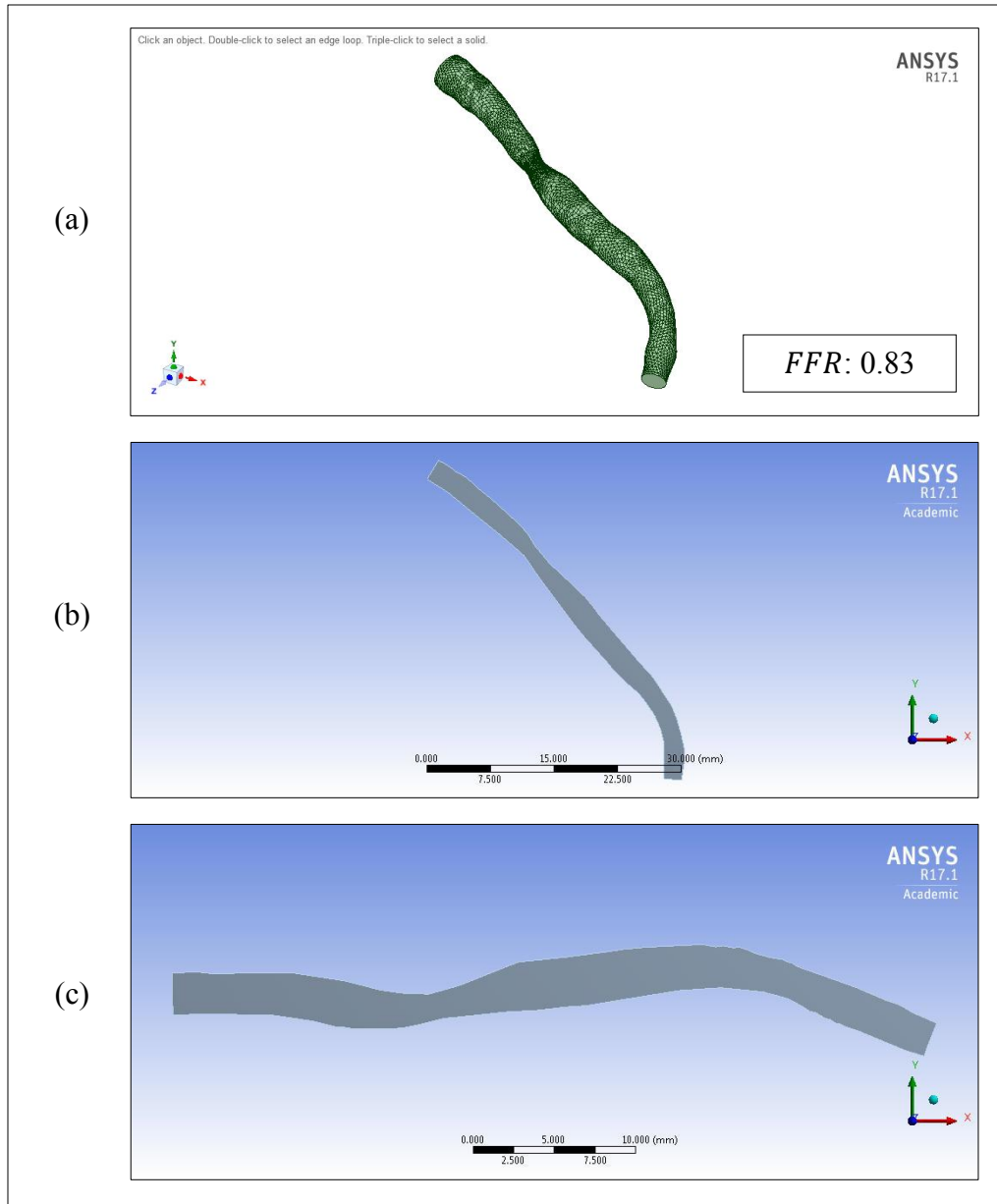


FIGURE 4.6 - Depictions of the (a) Three-Dimensional Source Rendering and Two-Dimensional (b) Slice 1 and (c) Slice 2 for the Artery of Patient 045

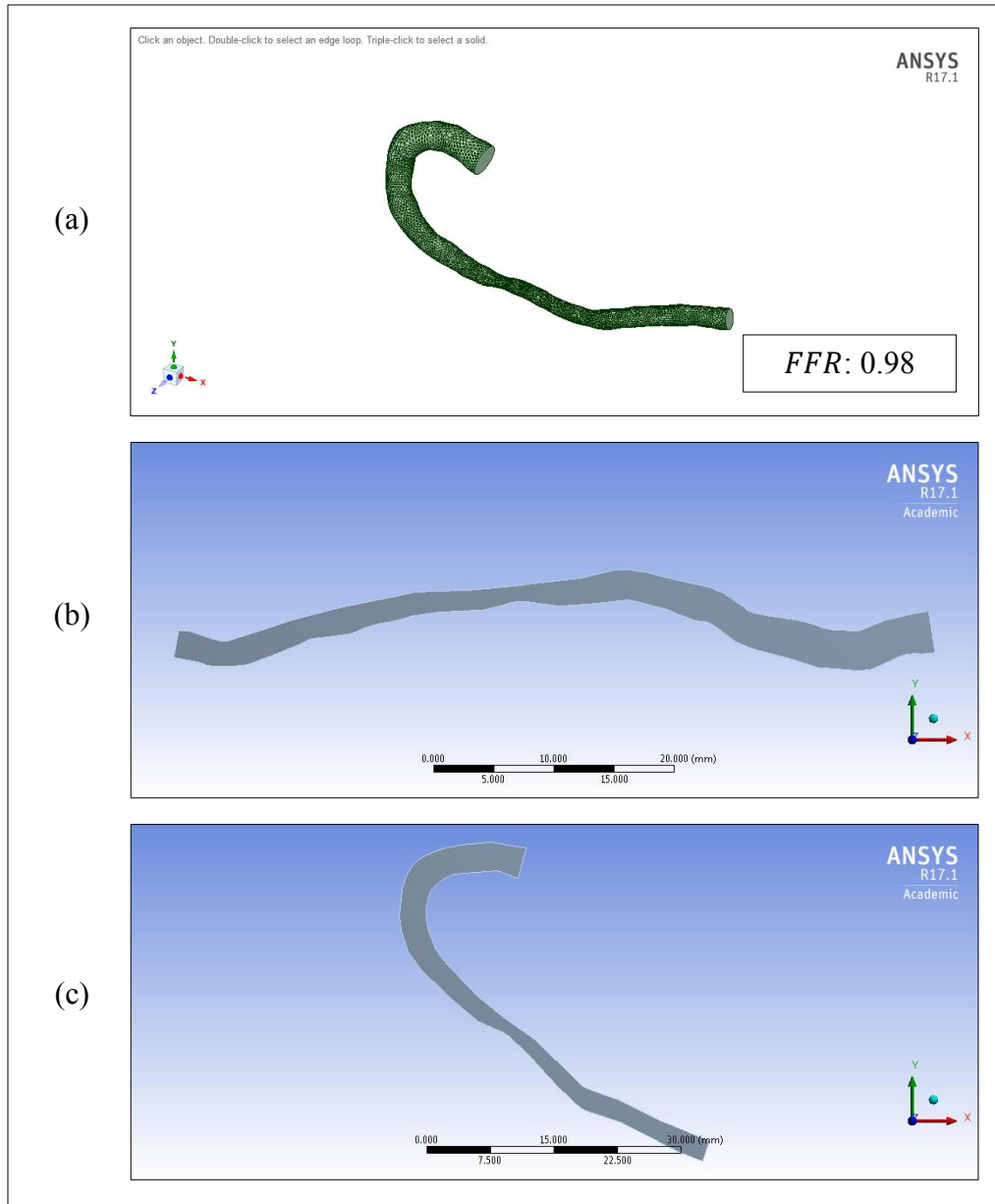


FIGURE 4.7 - Depictions of the (a) Three-Dimensional Source Rendering and Two-Dimensional (b) Slice 1 and (c) Slice 2 for the Artery of Patient 046

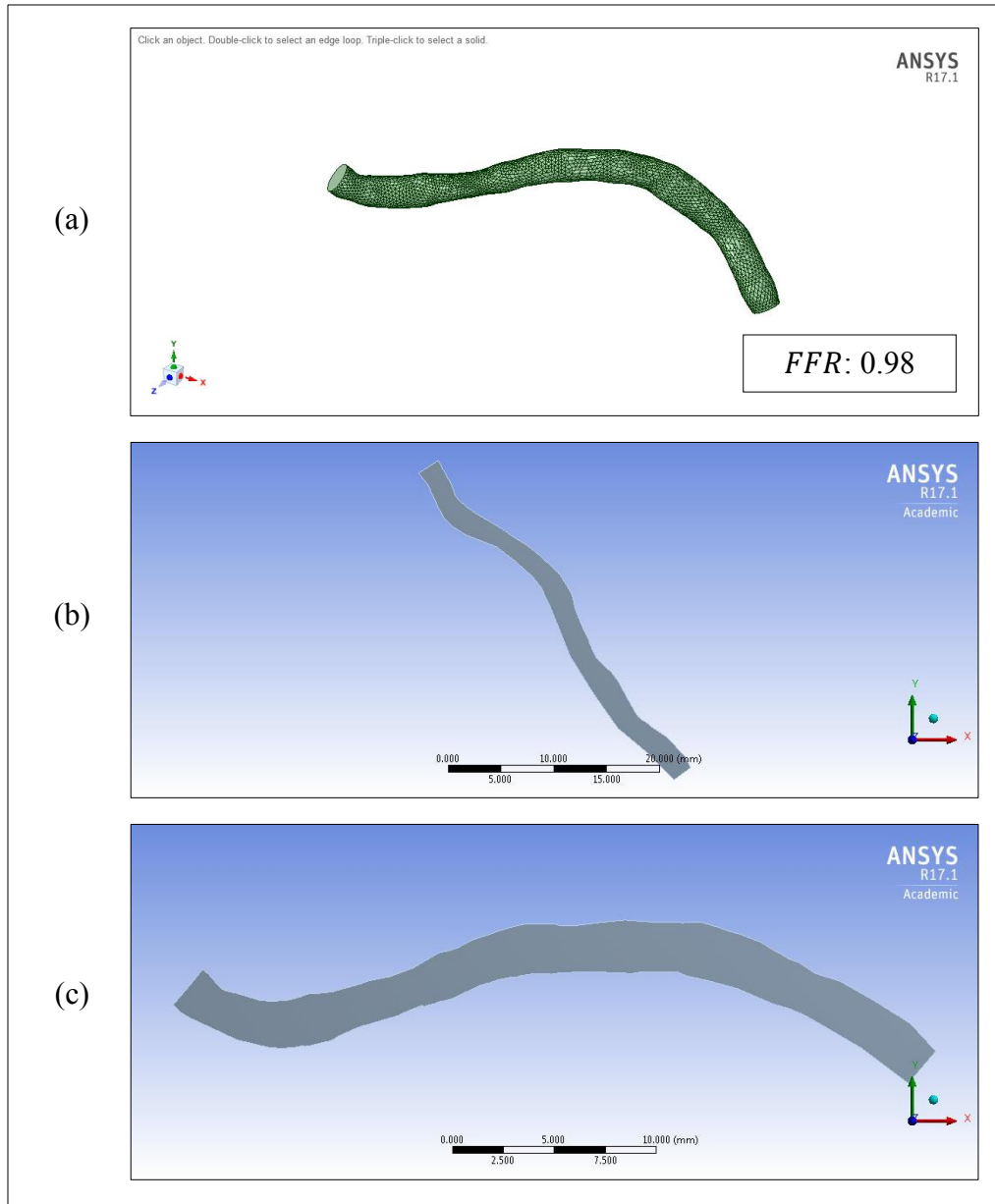


FIGURE 4.8 - Depictions of the (a) Three-Dimensional Source Rendering and Two-Dimensional (b) Slice 1 and (c) Slice 2 for the Artery of Patient 058

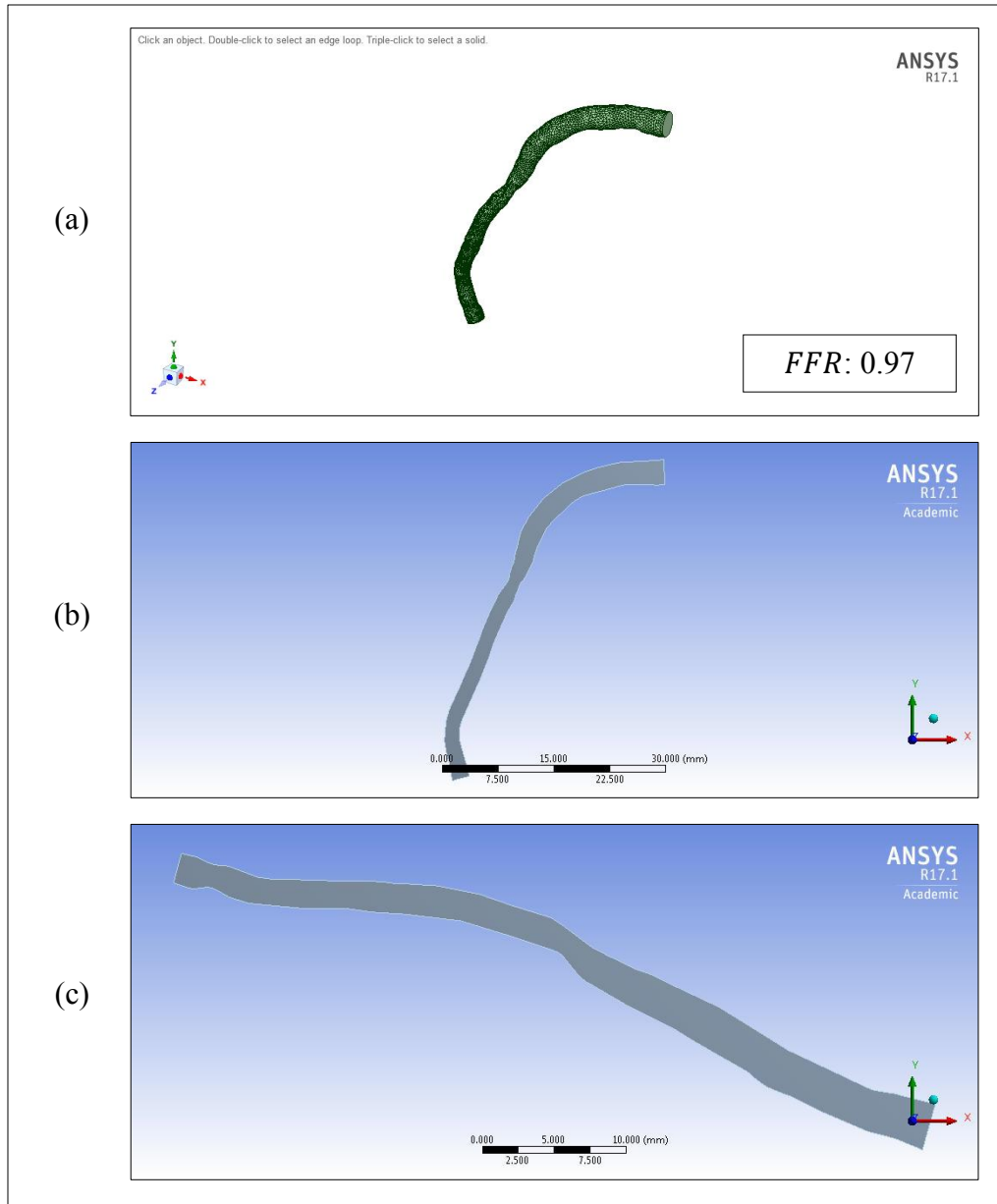


FIGURE 4.9 - Depictions of the (a) Three-Dimensional Source Rendering and Two-Dimensional (b) Slice 1 and (c) Slice 2 for the Artery of Patient 061

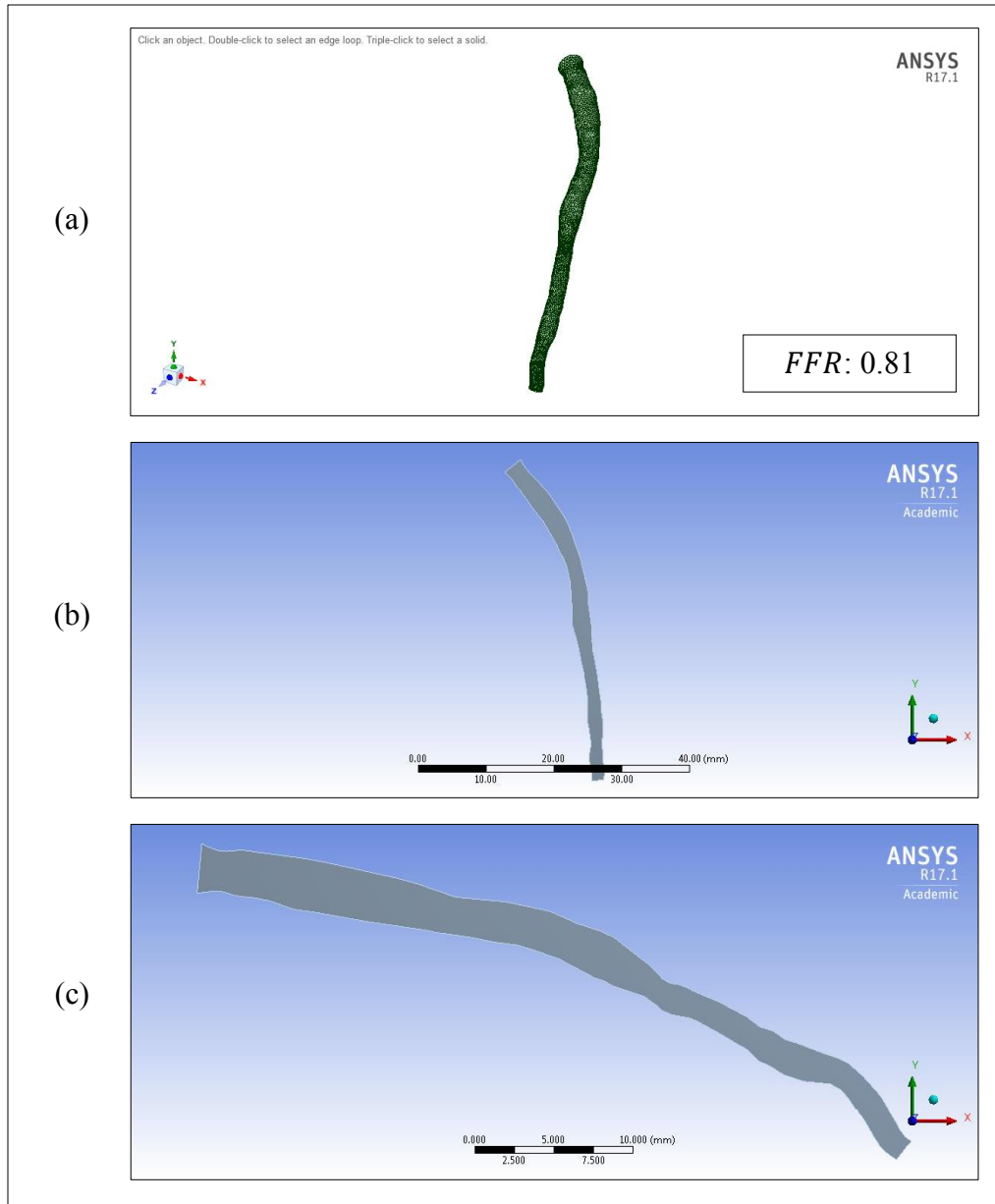


FIGURE 4.10 - Depictions of the (a) Three-Dimensional Source Rendering and Two-Dimensional (b) Slice 1 and (c) Slice 2 for the Artery of Patient 075

Fluent was used to simulate pulsing blood flow in each of the depictions shown in FIGURES 4.1–10 and to calculate the mean ages of the plasma and red blood cell phases using user-defined scalars. With Scalar1 representing plasma and Scalar0 representing red blood cells, it is noted that only Scalar0 results are presented in this section. Since

plasma is believed to behave more as a continuous phase within blood, its flow may be less impacted by a stenosis than the fluid's red blood cells. While red blood cells are not strictly granular, the granular method of modeling used for red blood cells is an attempt to create a simplified model of collision at a constriction within an artery. In using this setup, the red blood cell phase provides mean age data that the continuous, unaffected plasma phase simply cannot. These data are shown in subsequent plots of Scalar0 mean age. For completeness, however, plots of Scalar1 mean age may be seen in APPENDIX II.

B. Fluent Results of the Three-Dimensional Source Renderings

Fluent was used to simulate pulsing blood flow in the three-dimensional source renderings while tracking a user-defined scalar (Scalar0), representing the mean age of red blood cells, over the duration of flow. The plots displayed in this subsection subsequently represent the mean age of red blood cells as a function of elapsed flow time. Plots of Scalar0 mean age typically resemble periodic behavior as a result of the pulsing boundary conditions. Increased peaks of mean age varying from standard periodicity, however, are indicators of stenotic character along the flow path as blood attempts to transport from inlet to outlet but is impeded. In other words, an increase in mean age is attributed to an obstructing stenosis. With this, the plots utilize area-weighted averaging of the scalar value instead of mass-weighted averaging. Mean age itself is a calculation of the average time of all material passing through a given location rather than the average time of all material wherever it may be in the system. As a result, area-weighted average is more relevant than mass-weighted averaging for the three-dimensional source rendering systems.

The five cases of low *FFR* are shown in FIGURES 4.11–15:

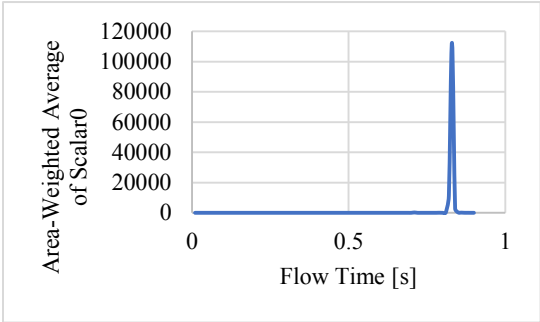


FIGURE 4.11 - Area-Weighted Average of Scalar0 for the Three-Dimensional Source

Rendering of Patient 004

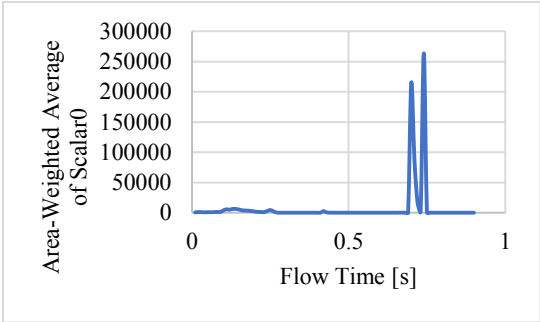


FIGURE 4.12 - Area-Weighted Average of Scalar0 for the Three-Dimensional Source

Rendering of Patient 005

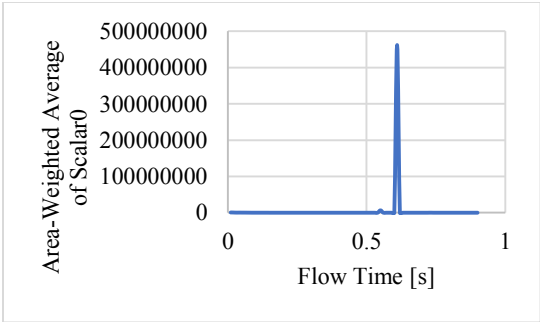


FIGURE 4.13 - Area-Weighted Average of Scalar0 for the Three-Dimensional Source

Rendering of Patient 017

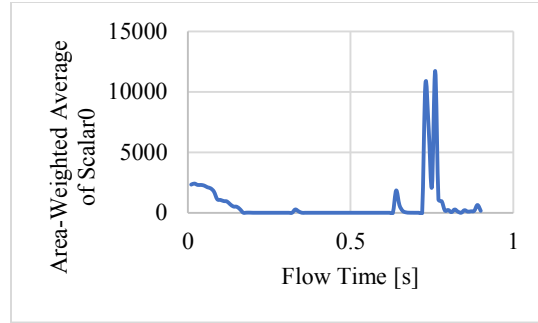


FIGURE 4.14 - Area-Weighted Average of Scalar0 for the Three-Dimensional Source

Rendering of Patient 019

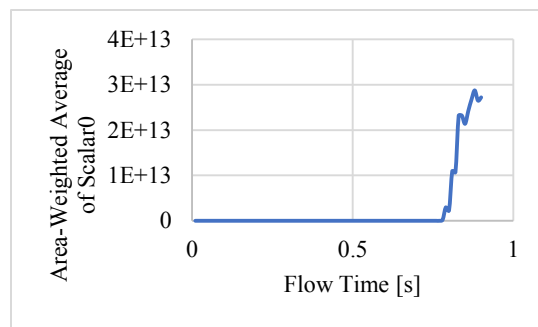


FIGURE 4.15 - Area-Weighted Average of Scalar0 for the Three-Dimensional Source

Rendering of Patient 041

As shown, each of the five low *FFR* source renderings exhibit an increased peak of significantly large magnitude. The appearance of high peaks may be attributed to stenotic character present within a source rendering. With this, patients of lower *FFR* value are observed to provide the highest elevation in peak. This is to say that Patient 041, with its *FFR* value of 0.70, displays the highest peak value, while Patients 004 and 019, with their *FFR* value of 0.76, exhibit the lowest increase in mean age. These results align with the expectations associated with an *FFR* value below 0.80 impacting an artery.

The five cases of high *FFR* are shown in FIGURES 4.16–20:

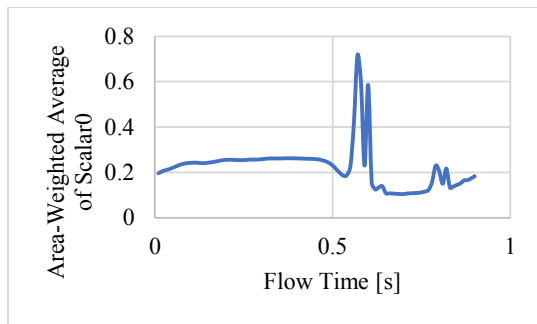


FIGURE 4.16 - Area-Weighted Average of Scalar0 for the Three-Dimensional Source

Rendering of Patient 045

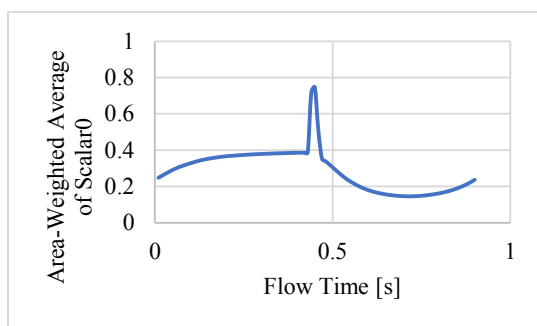


FIGURE 4.17 - Area-Weighted Average of Scalar0 for the Three-Dimensional Source

Rendering of Patient 046

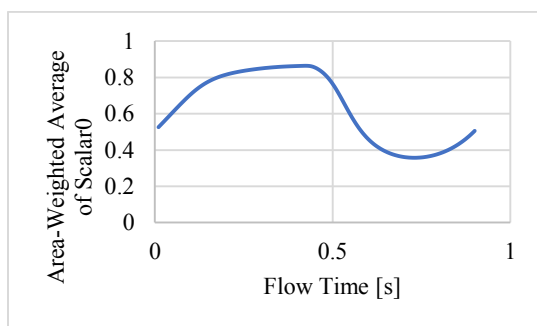


FIGURE 4.18 - Area-Weighted Average of Scalar0 for the Three-Dimensional Source

Rendering of Patient 058

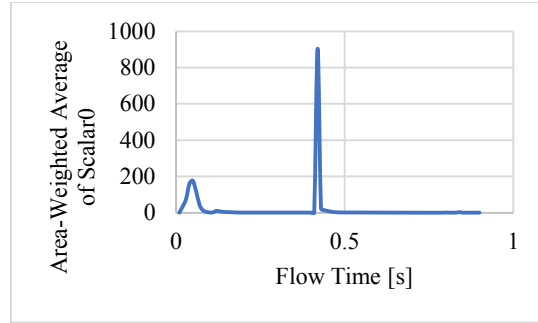


FIGURE 4.19 - Area-Weighted Average of Scalar0 for the Three-Dimensional Source

Rendering of Patient 061

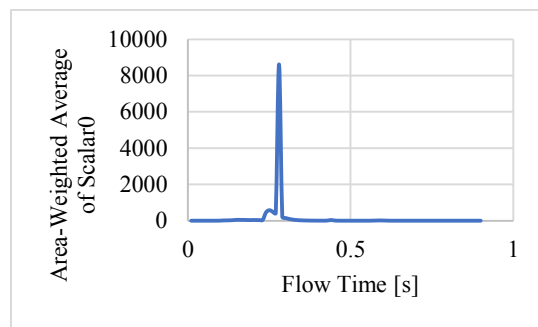


FIGURE 4.20 - Area-Weighted Average of Scalar0 for the Three-Dimensional Source

Rendering of Patient 075

As shown, three of the five high *FFR* source renderings (i.e., those from Patients 045, 046, and 058) exhibit the beginnings of periodicity and/or a slight peak of mean age value. As a whole, these source renderings align with the expectations governed by a high *FFR* value, which are expressed by their generally low mean age values. With this, however, there are increasingly elevated peaks present in the plots for Patients 061 and 075. Nevertheless, these peaks do not reach the same magnitudes of elevation as shown in renderings of low *FFR* value, and these increased peaks of mean age may be attributed to natural features of these particular arteries.

C. Fluent Results of the Two-Dimensional Arterial Slices

1. Plots of Scalar0 Mean Age and Nominal Mean Residence Time Comparison

Fluent was used to simulate pulsing blood flow in the two-dimensional arterial slices while tracking a user-defined scalar (Scalar0), representing the mean age of red blood cells, over the duration of flow. Again, it is stated that increased peaks of mean age varying from standard periodicity are indicators of stenotic character along the flow path as blood attempts to transport from inlet to outlet but is impeded. Succeeding plots with increased peaks of mean age are shaded gold. With this, the plots utilize area-weighted averaging of the scalar value instead of mass-weighted averaging for the same reason explained in the preceding subsection.

The five cases of low *FFR* are shown in FIGURES 4.21–25:

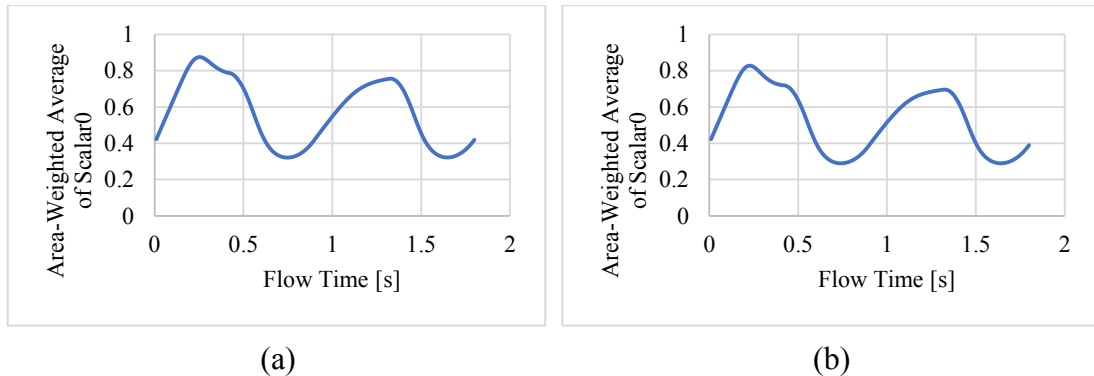
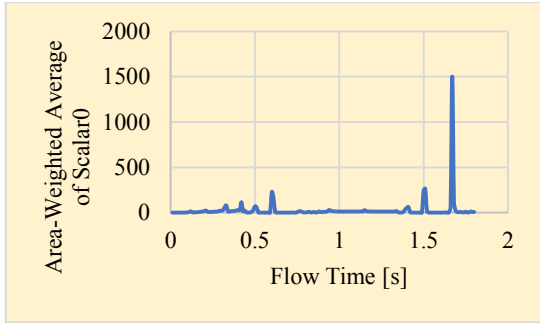
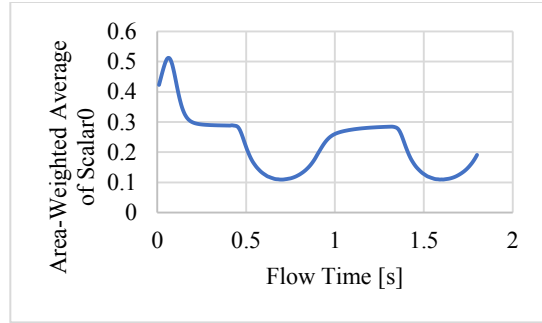


FIGURE 4.21 - Area-Weighted Average of Scalar0 for (a) Slice 1 and (b) Slice 2 of

Patient 004

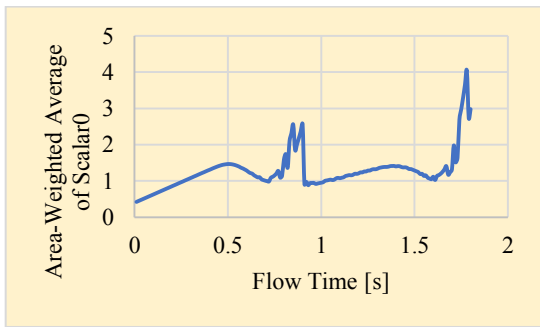


(a)

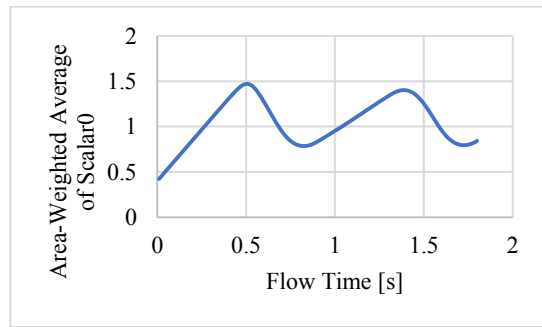


(b)

FIGURE 4.22 - Area-Weighted Average of Scalar0 for (a) Slice 1 and (b) Slice 2 of Patient 005

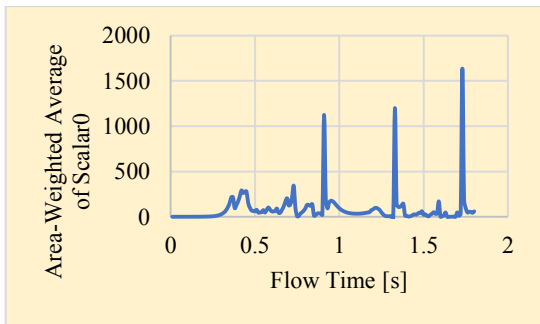


(a)

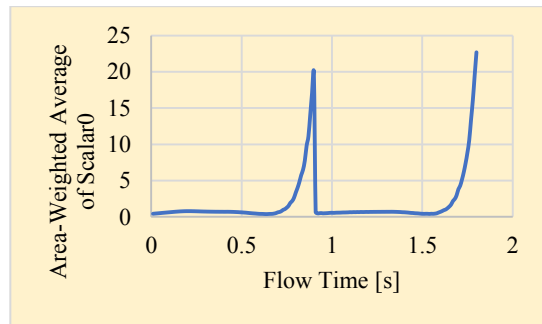


(b)

FIGURE 4.23 - Area-Weighted Average of Scalar0 for (a) Slice 1 and (b) Slice 2 of Patient 017



(a)



(b)

FIGURE 4.24 - Area-Weighted Average of Scalar0 for (a) Slice 1 and (b) Slice 2 of Patient 019

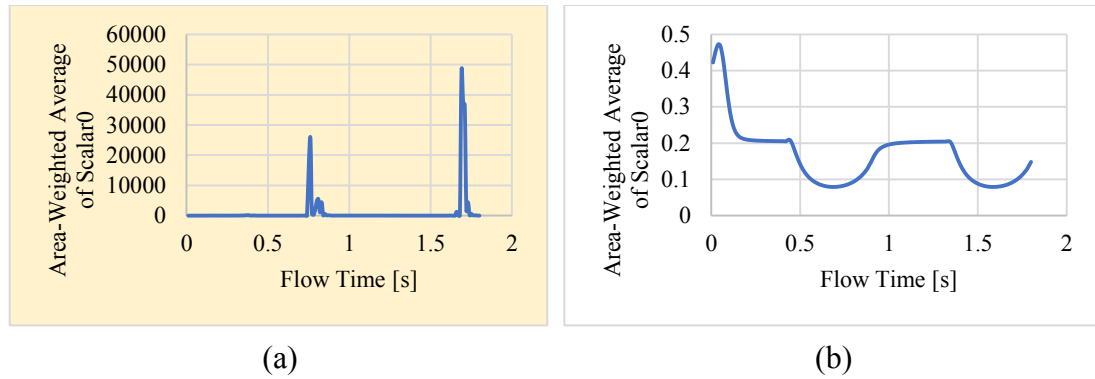
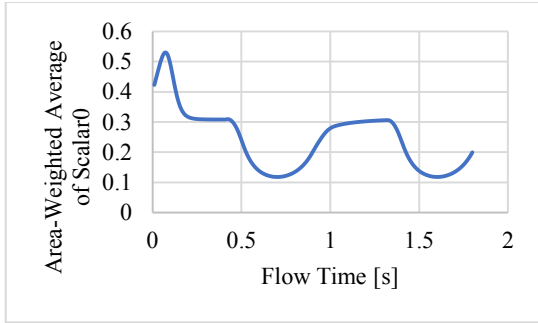


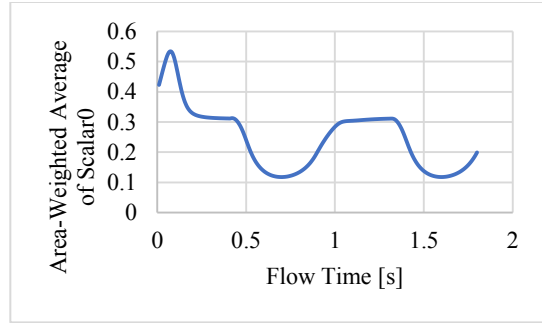
FIGURE 4.25 - Area-Weighted Average of Scalar0 for (a) Slice 1 and (b) Slice 2 of Patient 041

As shown, four out of the five low *FFR* cases contain at least one slice (shaded in gold) with increased peaks of Scalar0 value. Patient 019 saw increased peaks in both arterial slices, while Patients 005, 017, and 041 contained increased peaks in only one of the two slices. The appearance (and non-appearance) of high peaks may be attributed to the arbitrarily chosen planes for slicing. As discussed in EXPERIMENTAL METHODS, splines were used to create orthogonal slices from a given three-dimensional STL file. Only two angles out of 360° were created, leading to the possibility of uncaptured stenotic character within the three-dimensional rendering. Since arteries (and renderings of them) are not perfectly cylindrical, the potential of observing increased peaks in plots of Scalar0 mean age is highly dependent on the angular direction chosen for any sliced plane. The limitation in capturing stenotic character is a possibility in using only two slices, and this idea serves to explain the unexpected slice singularities of constant peak value observed and left unshaded in Patients 004, 005, 017, and 041.

The five cases of high *FFR* are shown in FIGURES 4.26–30:

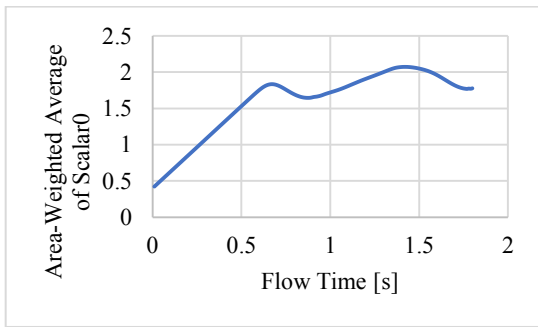


(a)

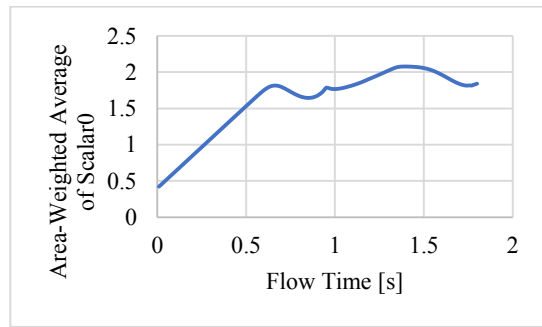


(b)

FIGURE 4.26 - Area-Weighted Average of Scalar0 for (a) Slice 1 and (b) Slice 2 of Patient 045

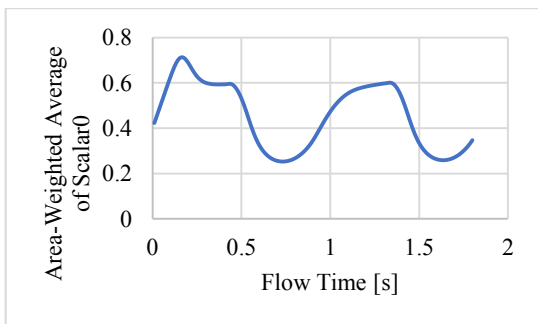


(a)

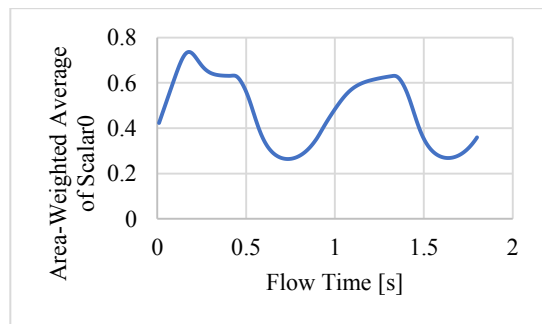


(b)

FIGURE 4.27 - Area-Weighted Average of Scalar0 for (a) Slice 1 and (b) Slice 2 of Patient 046



(a)



(b)

FIGURE 4.28 - Area-Weighted Average of Scalar0 for (a) Slice 1 and (b) Slice 2 of Patient 058

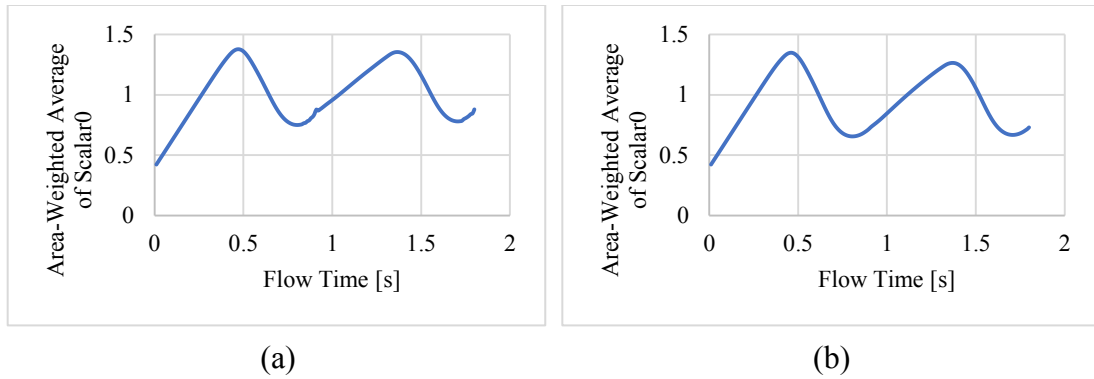


FIGURE 4.29 - Area-Weighted Average of Scalar0 for (a) Slice 1 and (b) Slice 2 of Patient 061

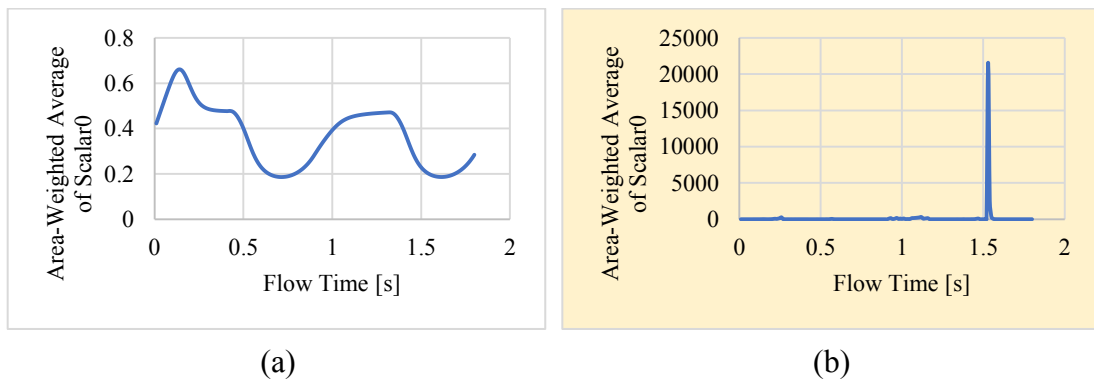


FIGURE 4.30 - Area-Weighted Average of Scalar0 for (a) Slice 1 and (b) Slice 2 of Patient 075

As shown, four out of the five high *FFR* cases resemble periodic functions with a nearly constant peak value. In fact, aside from Slice 2 of Patient 075, all other slices across the five cases demonstrate expected behavior. Slice 2 of Patient 075 outliers the total data set and could be ascribed to natural features of the actual artery that may only be expressed at this one arbitrary angle.

The peak data of the Scalar0 FIGURES may be tabulated to show the significant difference of mean age between low and high values of *FFR*. With this, peak data of the Scalar0 FIGURES may be compared to nominal values representing mean residence

times of blood flow if the geometry were not stenotic. The mean residence times are determined by dividing the volume of the three-dimensional source rendering by the volumetric flow rate governing the flow and dictated by the boundary conditions. The data containing mean age as a function of *FFR* and its comparison to nominal mean residence time are shown in TABLE 4.2:

TABLE 4.2

A COMPARISON OF MEAN AGE VALUES BETWEEN LOW AND HIGH *FFR* AND TO NOMINAL MEAN RESIDENCE TIMES FOR THE TWO-DIMENSIONAL ARTERIAL SLICES

Patient Number	<i>FFR</i>		Nominal Mean Residence Time [s]	Peak Scalar0 (Mean Age)		Percent Difference ($\times 10^{-1}$)	
				Slice 1	Slice 2	Slice 1	Slice 2
004	0.76	"low"	1.4×10^{-1}	8.8×10^{-1}	8.3×10^{-1}	53%	50%
005	0.75		9.1×10^{-2}	1.5×10^3	5.1×10^{-1}	164778%	46%
017	0.72		2.5×10^{-1}	4.0×10^0	1.5×10^0	149%	48%
019	0.76		1.5×10^{-1}	1.6×10^3	2.3×10^1	111225%	1533%
041	0.70		4.9×10^{-2}	4.8×10^4	4.7×10^{-1}	9672560%	86%
045	0.83	"high"	2.7×10^{-1}	5.3×10^{-1}	5.3×10^{-1}	9%	10%
046	0.98		3.3×10^{-1}	2.1×10^0	2.1×10^0	53%	53%
058	0.98		3.5×10^{-1}	7.1×10^{-1}	7.4×10^{-1}	11%	11%
061	0.97		3.0×10^{-1}	1.4×10^0	1.3×10^0	37%	36%
075	0.81		2.2×10^{-2}	6.6×10^{-1}	2.2×10^4	291%	9809017%

TABLE 4.2 may be used to emphasize the difference in mean age between low and high *FFR*. While high *FFR* cases are observed to range in orders of magnitude from tenths to ones, low *FFR* cases generally exhibit a mean age increased by no less than one order of magnitude. Although not always the case (as in Patients 004 and 017), this observation serves to support the notion of mean age increasing as *FFR* decreases. In addition to this, TABLE 4.2 serves to emphasize the difference between mean ages and nominal mean

residence times. The values differ more greatly in cases of low *FFR* than those for cases of high *FFR*, and this is enumerated in the columns of Percent Difference. With this, Slice 1 values for low *FFR* cases are distinctly higher than respective ones for Slice 2, which is evidenced by the increased peaks shown previously in the gold-shaded plots in FIGURES 4.22–25.

The directionality of a slice may have an effect in prompting increased mean age values, so it is noted here that Slice 1 and Slice 2 geometries were typically cut horizontally and vertically, respectively, to the trimetric view given by default in SpaceClaim. An example of this is shown in FIGURE 3.9 in EXPERIMENTAL METHODS. Resulting treatment in SolidWorks provided the slices shown in FIGURE 4.6, where Slice 1 is now oriented in the XY-plane nearly vertically and Slice 2 is now oriented nearly horizontally. This procedure was used for all slice creation, provided that the curvature of the three-dimensional rendering permitted its fulfillment. As shown in FIGURES 4.1–10, most slices follow this orientation scheme, but there are exceptions (such as Patient 019 and Patient 046). In viewing these FIGURES and TABLE 4.2, however, the patients with increased mean age values do not appear to find a correlation with the orientation of the slice. Directly, while Slice 1 geometries are typically vertical and represent the cases where increased peaks in mean age are present, Patient 019 displays increased mean age values while both slices are nearly horizontal.

2. Plots of Velocity Contours

The plots displayed in this subsection represent the computed velocity contours of the red blood cells phase. It is noted that velocity contours of the plasma phase are not shown since they are indistinguishable with the velocity contours of red blood cells. The

range of velocity magnitude gradates from blue to red as velocity increases, and the slice-specific spectrum of the velocity is shown in each of the depictions. The velocity contours for the five cases of low and five cases of high *FFR* are shown, respectively, in FIGURES 4.31–35 and FIGURES 4.36–40:

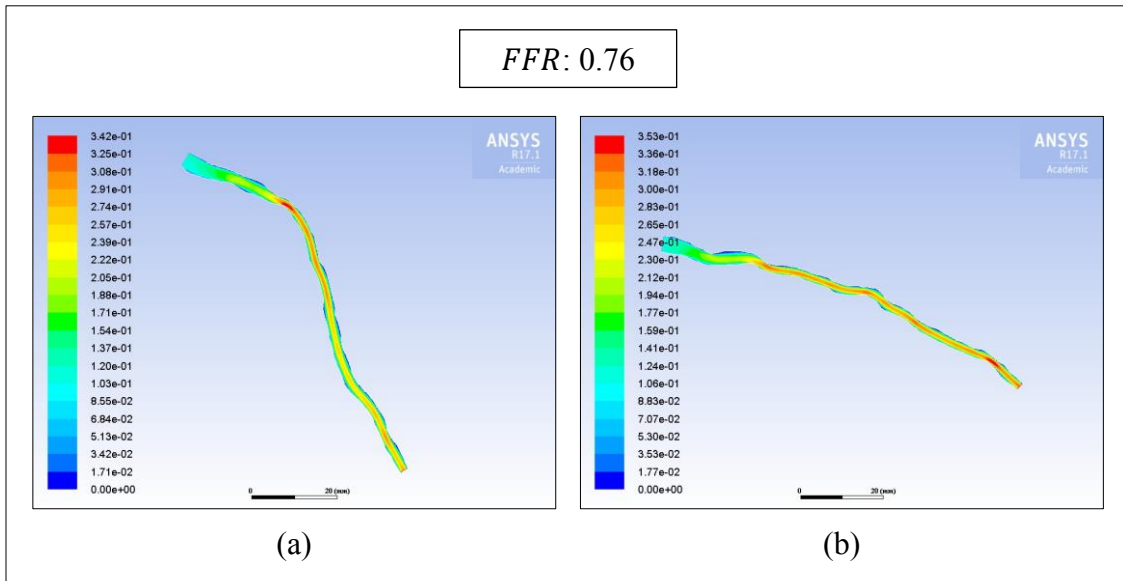


FIGURE 4.31 - Velocity Contours for (a) Slice 1 and (b) Slice 2 of Patient 004

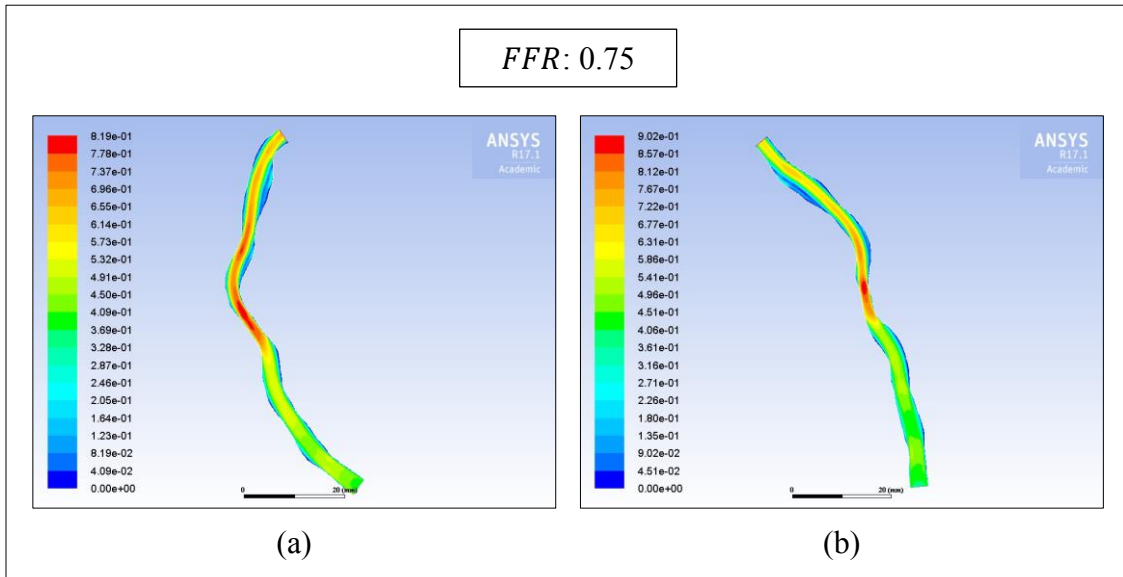


FIGURE 4.32 - Velocity Contours for (a) Slice 1 and (b) Slice 2 of Patient 005

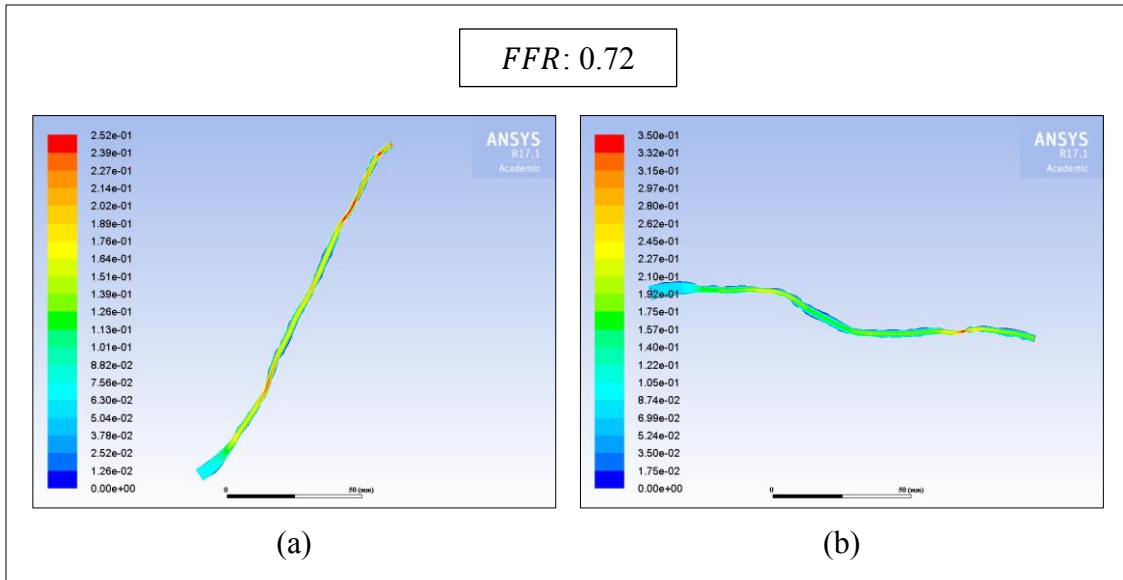


FIGURE 4.33 - Velocity Contours for (a) Slice 1 and (b) Slice 2 of Patient 017

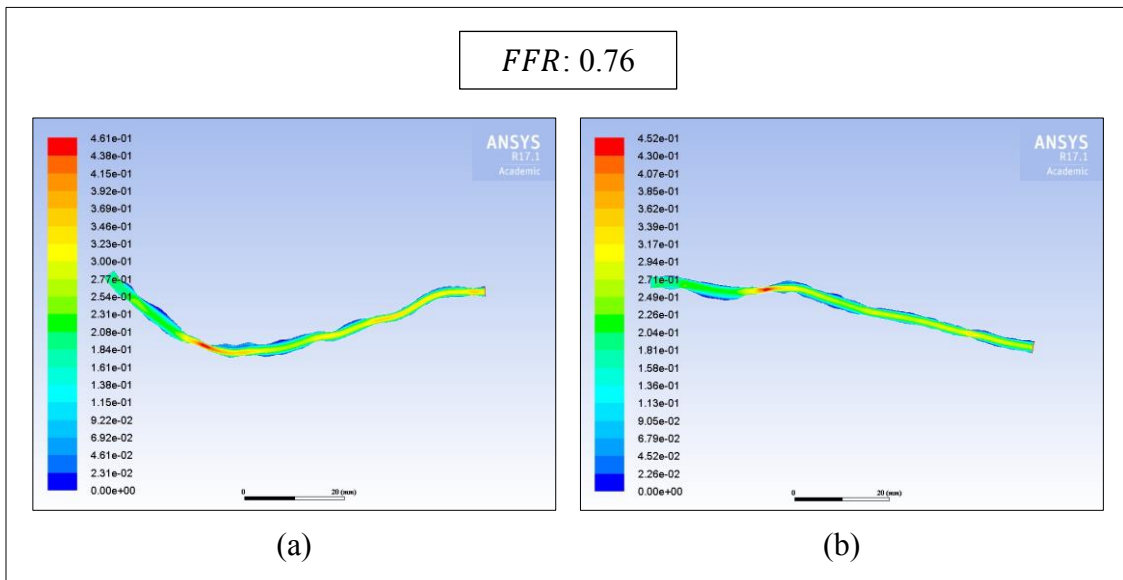


FIGURE 4.34 - Velocity Contours for (a) Slice 1 and (b) Slice 2 of Patient 019

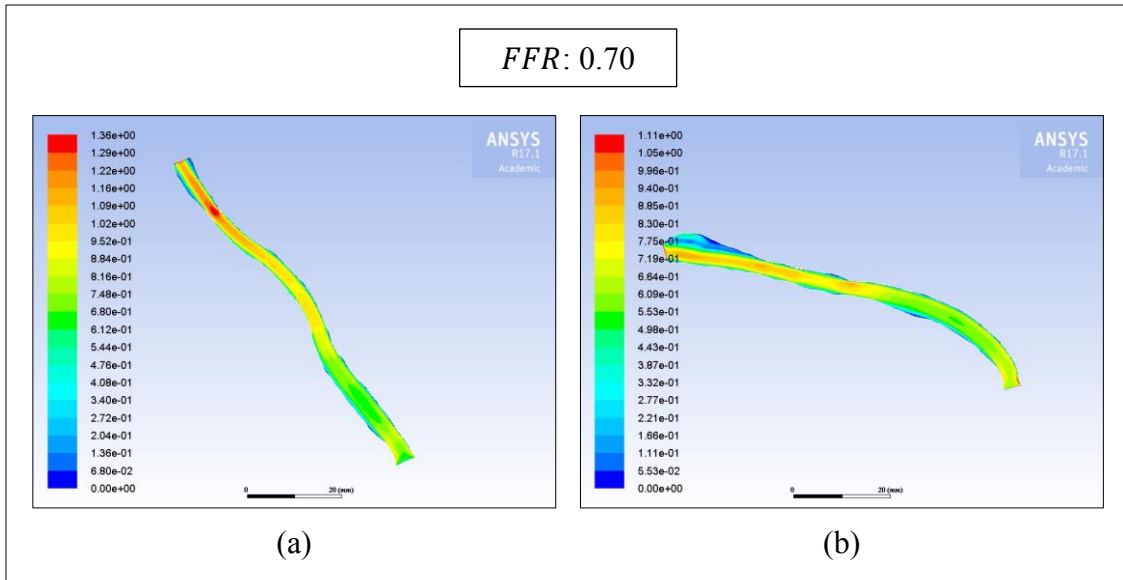


FIGURE 4.35 - Velocity Contours for (a) Slice 1 and (b) Slice 2 of Patient 041

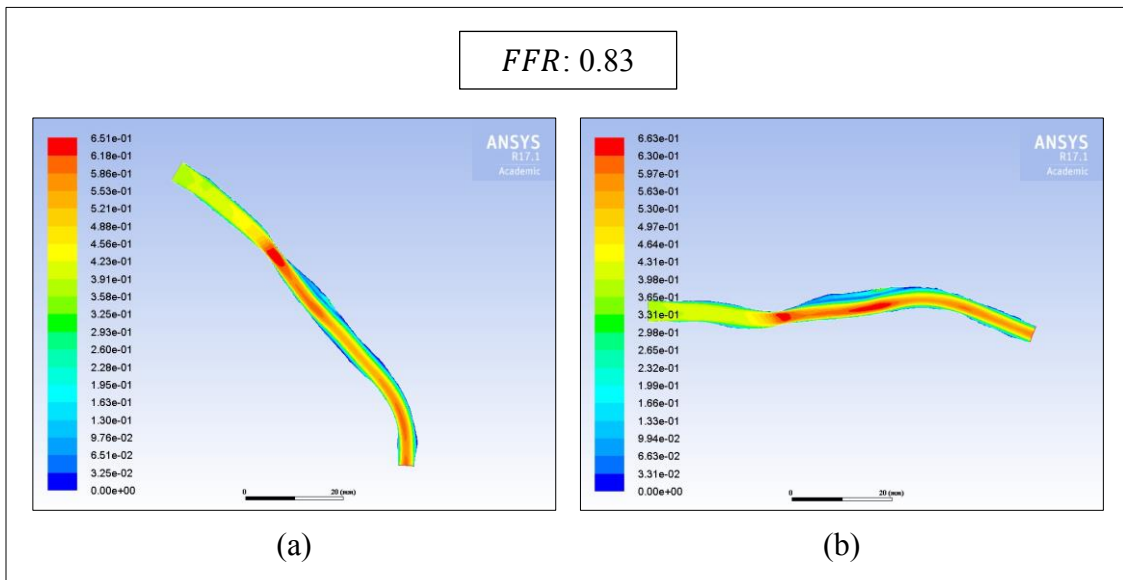


FIGURE 4.36 - Velocity Contours for (a) Slice 1 and (b) Slice 2 of Patient 045

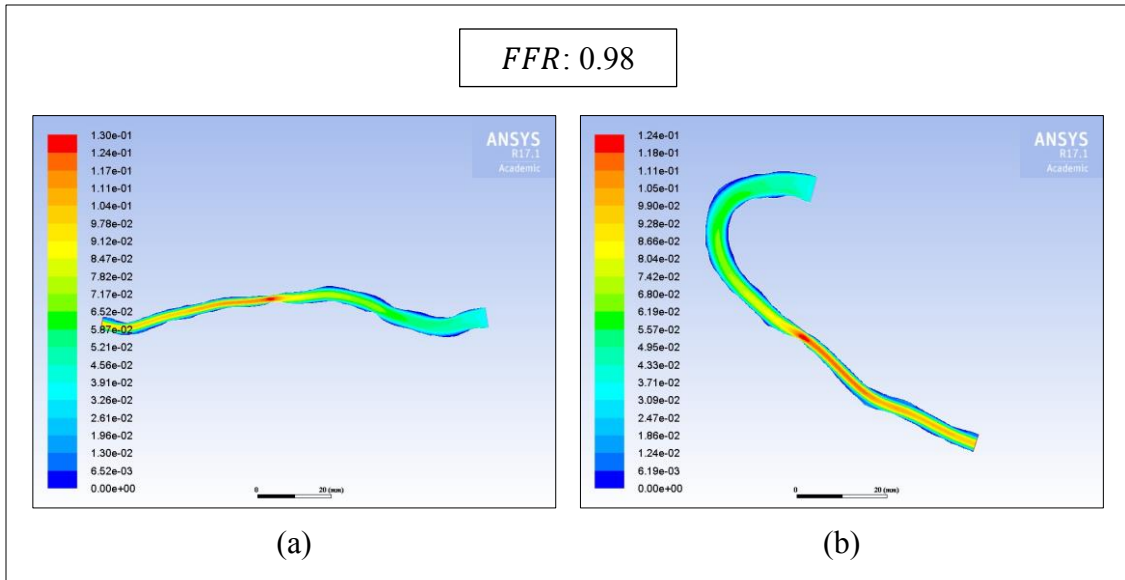


FIGURE 4.37 - Velocity Contours for (a) Slice 1 and (b) Slice 2 of Patient 046

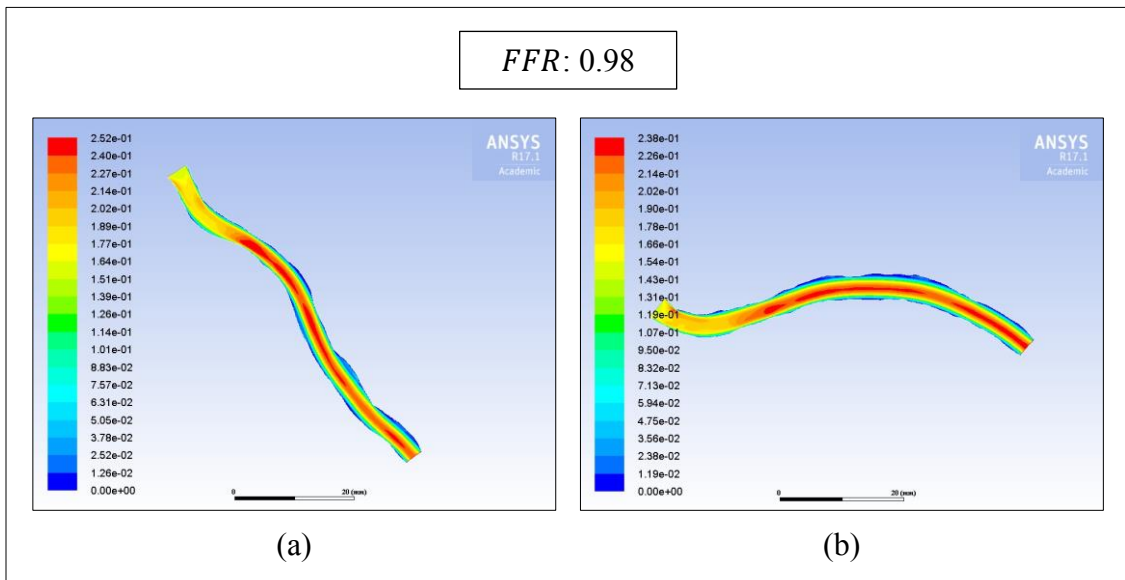


FIGURE 4.38 - Velocity Contours for (a) Slice 1 and (b) Slice 2 of Patient 058

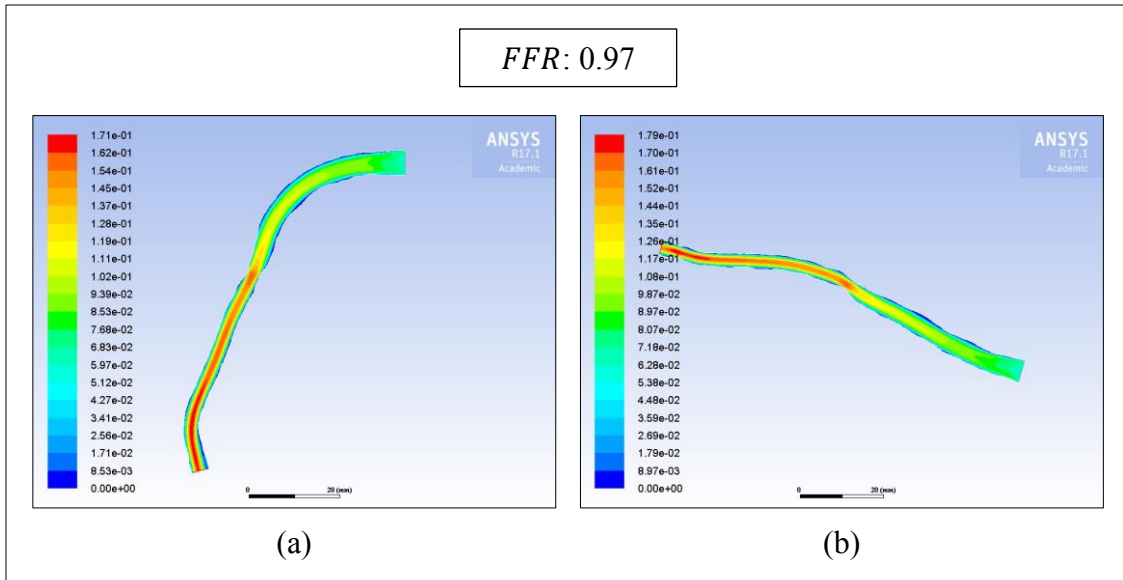


FIGURE 4.39 - Velocity Contours for (a) Slice 1 and (b) Slice 2 of Patient 061

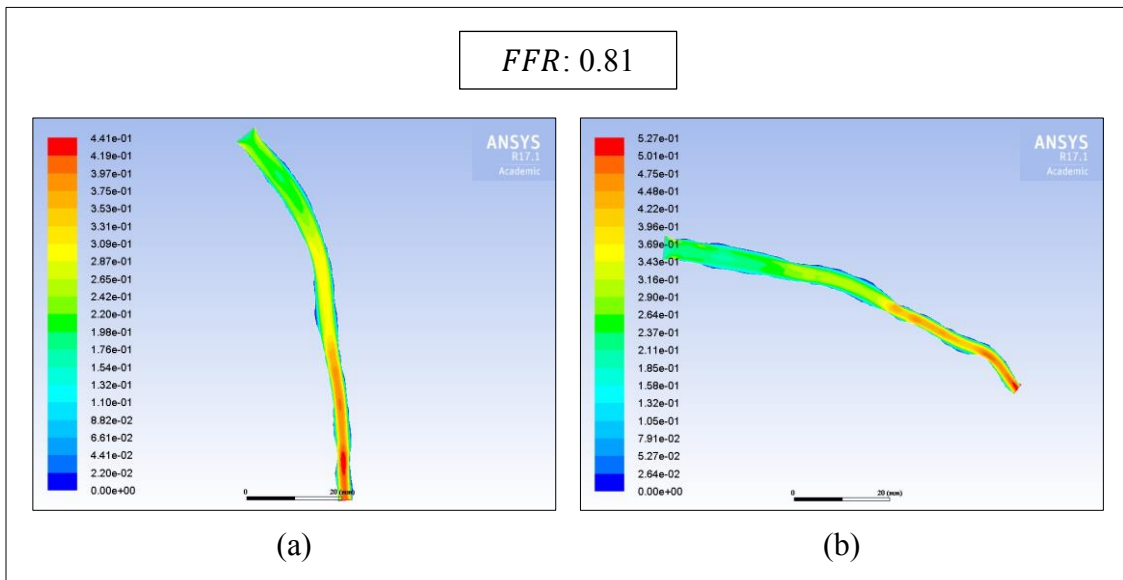


FIGURE 4.40 - Velocity Contours for (a) Slice 1 and (b) Slice 2 of Patient 075

The most observable difference between low and high FFR cases stems from the location and progression of increased regions of velocity magnitude. For most cases of low FFR , regions of red color (high velocity) are confined to discrete spots. Blue/green regions (lower velocity) typically surround these spots, leading to proper representations of actual stenoses. Patient 019 displays contours of this characterization, where distinct

concentrations of increased velocity denote a stenosis and are validated by its plots of Scalar0 mean age (FIGURE 4.24) and TABLE 4.2 to cause an increased mean age. Contrastingly, instead of having discrete sites of increased velocity, most cases of high *FFR* exhibit extended lengths of red color throughout a large portion of the slice. This is attributed to the artery and its slice narrowing naturally along the length of the geometry without the presence of an actual stenosis. Patient 058 exemplifies this behavior, where a developed stretch of red color dominates most of both slices, producing no apparent increase in mean age. This is substantiated by the Scalar0 mean age plots shown in FIGURE 4.28 and the data of TABLE 4.2. From this, it is generalized that contours of slices displaying distinct locations of increased velocity as a result of a stenosis typically influences and dictates an increased mean age value, while those contours with extended, non-stenotic stretches of maximum velocity do not produce an increase in mean age.

D. Three- and Two-Dimensional Comparison of Mean Age

The mean age data from the three- and two-dimensional simulations may be compared in an attempt to determine a relationship between the two spatial approaches. This relationship is sought to determine if reliable results can be obtained that reduces computational runtime. Directly, CFD processing of three-dimensional flow is typified by considerably lengthier calculation runtimes when compared to those of two-dimensional geometries. While three-dimensional calculations often approach a total duration on the order of several hours, two-dimensional processing usually lasts on the order of about 60 minutes, meaning only about 2% of alike runtime is needed. Ultimately, if two-dimensional slicing can produce a similar mean age metric to its three-dimensional source, the more easily-processed, two-dimensional slices may be preferentially chosen

to aid in long-term three-dimensional correlative approaches to *FFR*. To develop the relationship of these spatial approaches, the comparison of the two is efficiently presented by plotting mean age as function of *FFR*. The data required for plotting, now sorting from lowest to highest *FFR* value, are shown in TABLE 4.3:

TABLE 4.3

A COMPARISON OF MEAN AGE VALUES FOR THE THREE-DIMENSIONAL SOURCE RENDERINGS AND THE TWO-DIMENSIONAL ARTERIAL SLICES

Patient Number	<i>FFR</i>		Peak Scalar0 (Mean Age)		
			Source Rendering	Slice 1	Slice 2
041	0.70	"low"	2.9×10^{13}	4.8×10^4	4.7×10^{-1}
017	0.72		4.6×10^8	4.0×10^0	1.5×10^0
005	0.75		2.6×10^5	1.5×10^3	5.1×10^{-1}
004	0.76		1.1×10^5	8.8×10^{-1}	8.3×10^{-1}
019	0.76		1.2×10^4	1.6×10^3	2.3×10^1
075	0.81	"high"	8.6×10^3	6.6×10^{-1}	2.2×10^4
045	0.83		7.2×10^{-1}	5.3×10^{-1}	5.3×10^{-1}
061	0.97		9.0×10^2	1.4×10^0	1.3×10^0
046	0.98		7.5×10^{-1}	2.1×10^0	2.1×10^0
058	0.98		8.6×10^{-1}	7.1×10^{-1}	7.4×10^{-1}

As shown in TABLE 4.3, the mean age values of the slices are contained within a smaller range in comparison to the source rendering values. Notably, however, TABLE 4.3 serves to enumerate the difference in magnitudes between three- and two-dimensional processing of related cases as a result of an increasing *FFR* value. Cases of high *FFR* are typically within one order of magnitude between the source renderings and slices, while, in contrast, cases of low *FFR* retain mean age values of the source renderings that are many orders of magnitude higher than those of the corresponding slices. The significant difference in orders of magnitude between three- and two-dimensional processing of low *FFR* cases may be attributed to the complexity of the source renderings and the

simplicity of the slices. It is believed that important stenotic proceedings onset and captured by the complexity of the full three-dimensional source renderings are not captured by the simplicity of the two-dimensional slices. This is to say that occurrences such as increased red blood cell collisions around a stenosis or an increase in recirculatory eddies distal to a stenosis may be less expressed in the two-dimensional slice systems. As a result, mean ages between the two spatial approaches are quantified by substantial disparity in order of magnitude.

Setting the value of *FFR* as the ordinate and the value of mean age as the abscissa of an ordered pair, the data of TABLE 4.3 may be plotted in order to aid in better visualization. It is noted that while data for Slice 2 are present in TABLE 4.3, they are shown for completeness and are not used for plotting in subsequent FIGURES. The previous subsection established that Slice 2 geometries generally provided no increased peak in mean age, so they are withheld from further discussion. Moreover, it is noted that source rendering data plotting is performed separately from Slice 1 data plotting. The increased magnitudes associated with the source renderings make normalization between its data and Slice 1 data largely ineffectual, so two plots of different scale are created separately and are shown hereafter

The plot correlating mean age and *FFR* for the three-dimensional source renderings is shown in FIGURE 4.41:

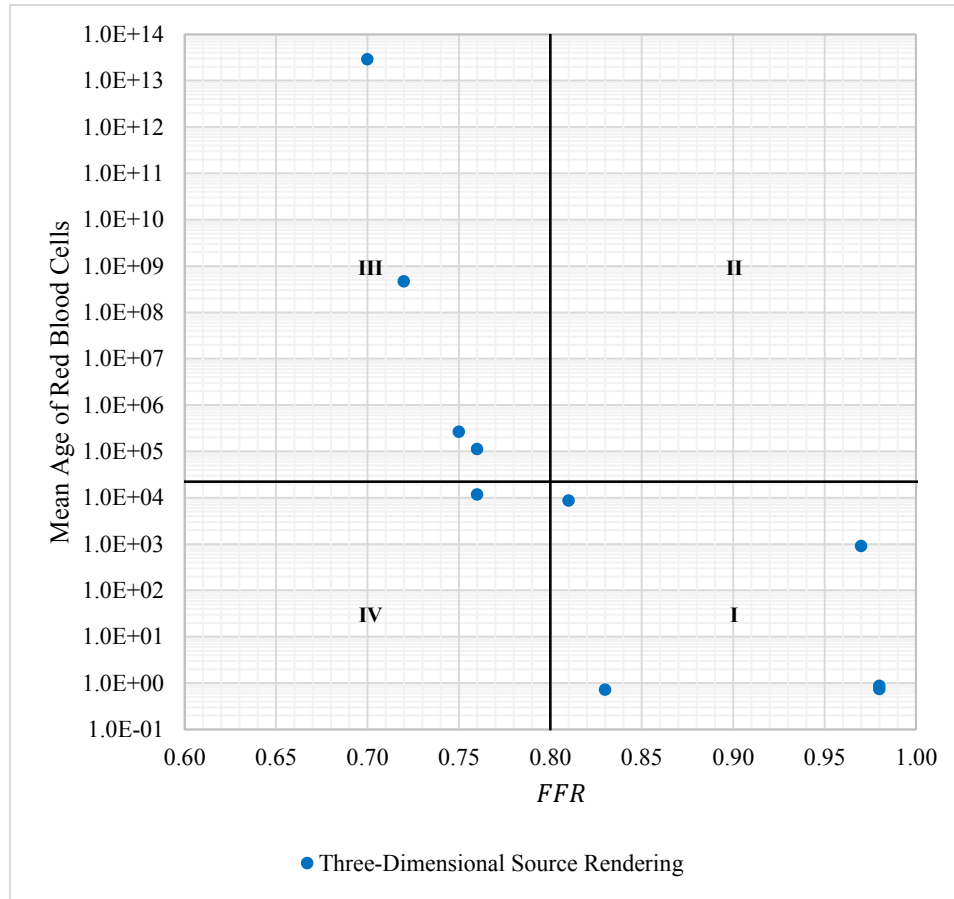


FIGURE 4.41 - Quadrant Plot Correlating the Mean Age of Red Blood Cells with *FFR* for the Three-Dimensional Source Rendering

FIGURE 4.41 utilizes a vertical line at the previously identified *FFR* threshold value of 0.80. It is noted that data points to the left of this line dictate cardiological intervention, while values to the right of this line dictate no intervention. An analogous line of demarcation is needed for the threshold value of mean age. In order to split the plot into quadrants, the threshold value of mean age must be determined so as to maximize the number of data points in the upper left and bottom right portions of the plot. In doing so, the number of patients mean age is able to diagnose accurately will approach that of the ability of *FFR*. In order to properly determine this threshold value, extensive statistical analysis is necessary. In this analysis, traditional and visualization techniques such as

ANOVA and regression are used to test a large set of data to find patterns or trends. Since the 10 three-dimensional simulation results were previously gathered from a large study of 80 patients, the threshold value has been statistically determined, and its value is 2.2×10^4 . As such, a horizontal line is plotted at this value, which is shown in FIGURE 4.41, to further demarcate the data and split the plot into quadrants.

Quadrants I, II, III, and IV of FIGURE 4.41 represent specific regions of importance with regards to mean age and *FFR* as diagnostics. As mentioned previously, maximizing the number of data points in Quadrants I and III is desired so as to bring mean age in close agreement with *FFR*. Data points in Quadrant I accurately predict withholding intervention necessity with low mean age and high *FFR* values, while data points in Quadrant III accurately predict intervention necessity with high mean age and low *FFR* values. In contrast, data points in Quadrants II and IV represent predictive errors in diagnosis and are sought to be minimized. Data points in Quadrant II are false positives that mistakenly suggest cardiological intervention is necessary, while data points in Quadrant IV are false negatives that mistakenly suggest intervention may be withheld. The tabulation of these medical statistics concerning FIGURE 4.41 is shown subsequently with Slice 1 data in TABLE 4.4.

The plot correlating mean age and *FFR* for the two-dimensional geometry of Slice 1 is shown in FIGURE 4.42:

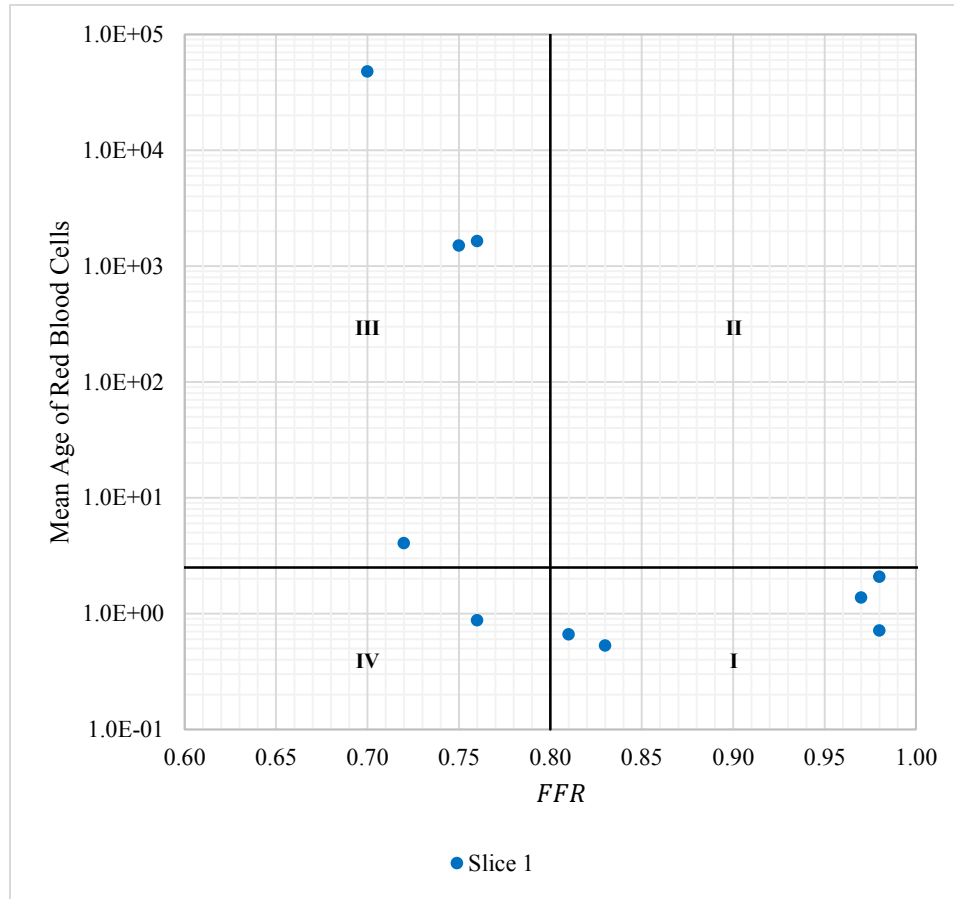


FIGURE 4.42 - Quadrant Plot Correlating the Mean Age of Red Blood Cells with *FFR* for the Two-Dimensional Geometry of Slice 1

Similar to the plot for the three-dimensional source renderings, FIGURE 4.42 utilizes a vertical line at the previously identified *FFR* threshold value of 0.80. Again, the analogous line of demarcation for the correct threshold value of mean age must be determined through statistical analysis. Rigorous tests in statistical analysis ultimately advance beyond the scope of this investigation due to the limited sample size of two-dimensional cases, but an estimation of the threshold value is warranted for demonstrative purposes. Similar to the quadrant plot for the source renderings, it is recognized that the threshold value of mean age must seek to maximize the number of data points in the upper left and bottom right portions of the plot. Therefore, as an

estimate achieving this goal, the threshold of mean age may be arbitrarily chosen as the value of 2.5×10^0 . Directly, a horizontal line is plotted at this value, which is shown in FIGURE 4.42, to further demarcate the data and split the plot into quadrants.

Quadrants I, II, III, and IV of FIGURE 4.42 represent the same medically relevant regions described of FIGURE 4.41 previously. As such, the medical statistics of false positives and false negatives concerning FIGURES 4.41 and 4.42 are shown in TABLE 4.4:

TABLE 4.4

TABULATION OF THE NUMBER OF OCCURRENCES OF PROPER DIAGNOSIS, FALSE POSITIVES, AND FALSE NEGATIVES OBSERVED IN THE QUADRANT PLOTS CORRELATING THE MEAN AGE OF RED BLOOD CELLS AND *FFR*

System	Occurrences of Proper Diagnosis	False Positives	False Negatives
Three-Dimensional Source Rendering	9	0	1
Slice 1	9	0	1

As shown in TABLE 4.4, only one false negative for each spatial approach is present in the data when the statistical and arbitrary threshold values of 2.2×10^4 and 2.5×10^0 are used for the source renderings and Slice 1, respectively. While limited in sample size, false diagnosis is thusly 10% for each system. In literature, virtual approaches to *FFR* using larger sample sizes have shown false diagnostic values of 10–13% (Papafaklis et al., 2014; Tu et al., 2014; Tröbs et al., 2016). In order to maintain the presently competing approach that utilizes multiphase mean age theory, its false diagnostic percentages should not be greater than those of other virtual *FFR* techniques. For the present technique, however, the medical statistics shown in TABLE 4.4 aid in

quantifying similarity between the spatial approaches, and the proper statistical determination of two-dimensional threshold will rely on this comparison in future research developments. It is noted that while both medical statistics represent incongruence with the predictions of *FFR*, the overdiagnosis of cardiological intervention is less problematic than that of underdiagnosing it.

With the data of the quadrant plots shown in full, it is again restated that the line of demarcation denoting the threshold value of mean age for the two-dimensional data was chosen arbitrarily. This value serves as a starting point to demonstrate the feasibility of two-dimensional slicing as a surrogate to equivalently processing a three-dimensional source rendering. As shown in the previous TABLES and FIGURES, two-dimensional slicing bolsters appreciable diagnostic similarity to three-dimensional processing when a subjective mean age threshold has been chosen. These results aid in administering the preliminary determination of two-dimensional slicing as a meritorious technique regarding cardiological context, but at least 80–100 data points are needed to confidently support this claim. Ultimately, with more testing and the employment of proper statistical analysis efforts, the threshold value of mean age related to the arterial slices may be confirmed to strengthen the assertions made of two-dimensional blood flow simulations.

V. CONCLUSIONS

A comparison of stenotic blood flow in two-dimensional arterial slices to flow in their three-dimensional source renderings was executed using CFD and multiphase mean age theory. Useful in present research attempting to unite angiography with a non-invasive stenotic evaluator, a relationship between the three- and two-dimensional approaches was sought to obtain a comparable method of arterial simulation processing that significantly reduces computational runtime. Computer-aided design software packages were used to generate two orthogonal arterial slices from DICOM-derived, three-dimensional STL files of arteries rendered by coronary angiograms. Following mesh generation by the discretization of the domains of the created geometries, CFD software was employed to simulate pulsing blood flow in the geometries and to apply multiphase mean age theory to calculate the mean age of red blood cells using user-defined scalars. Results were presented for five patient cases below and five patient cases above the commonly accepted *FFR* threshold value of 0.80, below which cardiological intervention is prompted for stent placement as a mechanism to avert ischemia.

In tracking the area-weighted average of mean age of red blood cells, plots of mean age throughout the duration of a complete pulse demonstrated peaks with higher orders of magnitude for cases with *FFR* less than 0.80. The two-dimensional arterial slices typically exhibited this behavior in only the vertically-oriented geometries of Slice 1. This was ascribed to the limitation of testing only two angles of a 360° arterial segment, which more than likely eventuated uncaptured stenotic character from the three-dimensional renderings within the ineffectual slice. Nevertheless, it was determined that,

if sliced at a proper angle, two-dimensional slices are able to distinguish between low and high *FFR*.

The increases in mean age for the three-dimensional cases were many orders of magnitude higher than those of the corresponding two-dimensional cases. This was attributed to phenomena near a stenosis—such as red blood cell collisions or distal recirculatory eddies—being less expressed in the simplicity of the two-dimensional arterial slices when compared to the complex character of the full three-dimensional source renderings.

Mean age data from the three- and two-dimensional simulations were compared using quadrant plots to establish the relationship between the two spatial approaches that administers the determination of two-dimensional slicing as a worthy technique regarding cardiological context and computational timeliness. Three-dimensional diagnostic ability was demonstrated by utilizing a statistically analyzed mean age threshold value of 2.2×10^4 , while an arbitrary threshold value (2.5×10^0) demarcating the diagnostic ability for two-dimensional processing was used since limited sample size impeded full statistical treatment to obtain it. While not fully statistically grounded, the arbitrary threshold was used in an analogous manner to that of the *FFR* threshold value of 0.80 to depict the potentiality of slicing as a proxy to equivalently processing a source rendering. As a demonstration, this arbitrary value was utilized to indicate the capacity of proper medical pronouncement, where the medical statistics of false positives and false negatives were largely outweighed by it.

While three-dimensional calculations often approached a total duration on the order of several hours while utilizing parallel computing on 20 processors, two-

dimensional processing required on the order of about 60 minutes on a single processor, which is less than 2% of the required computing power of the three-dimensional cases. Preliminary results indicate two-dimensional processing retains compelling calculation merit and will be well positioned to efficiently detect and assess stenoses non-invasively, provided that it holds up to rigorous statistical analysis.

VI. RECOMMENDATIONS

Foremost, an investment into researching other computer-aided design software should be made in an attempt to simplify and ease the process of generating arterial slices. As presented in EXPERIMENTAL METHODS, slice generation performed in SpaceClaim required a combination of tedious rotating, zooming, panning, and clicking of indiscriminate points along the length of the wall of an artery to create splines that represented three-dimensional arterial outlines. Researching and testing the capabilities of other commercially available software may lead to slice generation that is far more expeditious and aids in ensuring orthogonality of geometry is met. With this, as mentioned in RESULTS AND DISCUSSION, only two angles out of 360° were created, which lent credence to the possibility of stenotic character being uncaptured from the three-dimensional rendering. Ideally, in researching other computer-aided design software, the ability to revolve a single slice within the boundaries of a three-dimensional rendering may be discovered so as to foster swift slice generation and permit the creation of all angles automatically. In doing so, the results of blood flow simulation in all of the angles may be linked to provide conclusions that more closely mirror the baseline outcomes drawn from three-dimensional processing.

Other recommendations stem from the amount of cases tested, statistical analysis, and the meshes used for simulation. Specifically, while 10 cases were analyzed in this investigation, more DICOM-derived, three-dimensional STL files of arteries rendered by coronary angiograms could be provided for slicing treatment in an attempt to increase the repeatability of results, establish better trends, and ultimately further the strength of gathered assertions. Directly, testing at least 80–100 additional cases of varying *FFR*

value—with a concurrent employment of statistical analysis that establishes the proper threshold value of mean age—would serve to confidently govern the determination of two-dimensional slicing as a worthy cardiological technique when compared to alike processing in three-dimensions. Finally, in testing these extra cases, mesh sensitivity analysis could be performed as a way to determine whether increasing the element count of the discretized domain better resolves the flow field and creates improved mean age data.

REFERENCES CITED

- Ambrose, J. A., & Singh, M. (2015). Pathophysiology of coronary artery disease leading to acute coronary syndromes. *F1000Prime Reports*, 7.
- Approaches to Multiphase Modeling. (2006). *ANSYS Fluent 6.3 User's Guide - 23.2.1*.
www.sharcnet.ca/Software/Fluent6/html/ug/node876.htm#sec-mphase-approaches.
- Bhaskaran, R., & Collins, L. (2002). Introduction to CFD basics. *Cornell University-Sibley School of Mechanical and Aerospace Engineering*.
- Cassar, A., Holmes, D. R., Rihal, C. S., & Gersh, B. J. (2009). Chronic coronary artery disease: diagnosis and management. In *Mayo Clinic Proceedings* (Vol. 84, No. 12, pp. 1130-1146). Elsevier.
- Danckwerts, P. V. (1953). Continuous flow systems: distribution of residence times. *Chemical Engineering Science*, 2(1), 1-13.
- Finegold, J. A., Asaria, P., & Francis, D. P. (2012). Mortality from ischaemic heart disease by country, region, and age: statistics from World Health Organisation and United Nations. *International Journal of Cardiology*, 168(2), 934-945.
- Gerber, B. L. (2007). MRI versus CT for the detection of coronary artery disease: current state and future promises. *Current Cardiology Reports*, 9(1), 72-78.
- Gould, K. L., Lipscomb, K., & Hamilton, G. W. (1974). Physiologic basis for assessing critical coronary stenosis: instantaneous flow response and regional distribution during coronary hyperemia as measures of coronary flow reserve. *American Journal of Cardiology*, 33(1), 87-94.
- Hanson, M. A., Fareed, M. T., Argenio, S. L., Agunwamba, A. O., & Hanson, T. R. (2013). Coronary artery disease. *Primary Care: Clinics in Office Practice*, 40(1), 1-16.
- Kim, K. H., Doh, J. H., Koo, B. K., Min, J. K., Erglis, A., Yang, H. M., Park, K. W., & Lee, H. Y. (2014). A novel noninvasive technology for treatment planning using virtual coronary stenting and computed tomography-derived computed fractional flow reserve. *JACC: Cardiovascular Interventions*, 7(1), 72-78.
- Lederman, S. J., Menegus, M. A., & Greenberg, M. A. (1997). Fractional flow reserve. *ACC Current Journal Review*, 6(1), 34-35.
- Liu, M., & Tilton, J. N. (2010). Spatial distributions of mean age and higher moments in steady continuous flows. *AIChE Journal*, 56(10), 2561-2572.

REFERENCES CITED (CONT.)

- Min, J. K., Leipsic, J., Pencina, M. J., Berman, D. S., Koo, B. K., van Mieghem, C., Erglis, A., & Lin, F. Y. (2012). Diagnostic accuracy of fractional flow reserve from anatomic CT angiography. *Jama*, *308*(12), 1237-1245.
- Min, J. K., Taylor, C. A., Achenbach, S., Koo, B. K., Leipsic, J., Nørgaard, B. L., Pijls, N. H., & De Bruyne, B. (2015). Noninvasive fractional flow reserve derived from coronary CT angiography: clinical data and scientific principles. *JACC: Cardiovascular Imaging*, *8*(10), 1209-1222.
- Nørgaard, B. L., Jensen, J. M., & Leipsic, J. (2015). Fractional flow reserve derived from coronary CT angiography in stable coronary disease: a new standard in non-invasive testing?. *European Radiology*, *25*(8), 2282-2290.
- Overview. (2006). *ANSYS Fluent 6.3 User's Guide - 22.1*.
www.sharcnet.ca/Software/Fluent6/html/ug/node806.htm#sec-dpm-approaches.
- Overview of Flow Solvers. (2009). *ANSYS Fluent 12.0 Theory Guide - 18.1*.
www.afs.enea.it/project/neptunius/docs/fluent/html/th/node360.htm.
- Papafaklis, M. I., Muramatsu, T., Ishibashi, Y., Lakkas, L. S., Nakatani, S., Bourantas, C. V., Ligthart, J., & Onuma, Y. (2014). Fast virtual functional assessment of intermediate coronary lesions using routine angiographic data and blood flow simulation in humans: comparison with pressure wire-fractional flow reserve. *EuroIntervention: Journal of EuroPCR in collaboration with the Working Group on Interventional Cardiology of the European Society of Cardiology*, *10*(5), 574-583.
- Pijls, N. H., de Bruyne, B., Peels, K., van der Voort, P. H., Bonnier, H. J., Bartunek, J., & Koolen, J. J. (1996). Measurement of fractional flow reserve to assess the functional severity of coronary-artery stenoses. *New England Journal of Medicine*, *334*(26), 1703-1708.
- Russ, D. C., & Berson, R. E. (2016). Mean age theory in multiphase systems. *Chemical Engineering Science*, *141*, 1-7.
- Sandberg, M. (1981). What is ventilation efficiency?. *Building and Environment*, *16*(2), 123-135.
- Software: CFD Simulation. (2017). *ANSYS Fluent Software: CFD Simulation*. www.ansys.com/Products/Fluids/ANSYS-Fluent.
- Spalding, D. B. (1958). A note on mean residence-times in steady flows of arbitrary xcomplexity. *Chemical Engineering Science*, *9*(1), 74-77.

REFERENCES CITED (CONT.)

- Sun, Z., & Xu, L. (2014). Computational fluid dynamics in coronary artery disease. *Computerized Medical Imaging and Graphics*, 38(8), 651-663.
- Tröbs, M., Achenbach, S., Röther, J., Redel, T., Scheuering, M., Winneberger, D., Klingenberg, K., & Itu, L. (2016). Comparison of fractional flow reserve based on computational fluid dynamics modeling using coronary angiographic vessel morphology versus invasively measured fractional flow reserve. *American Journal of Cardiology*, 117(1), 29-35.
- Tu, S., Barbato, E., Köszegi, Z., Yang, J., Sun, Z., Holm, N. R., Tar, B., & Li, Y. (2014). Fractional flow reserve calculation from 3-dimensional quantitative coronary angiography and TIMI frame count: a fast computer model to quantify the functional significance of moderately obstructed coronary arteries. *JACC: Cardiovascular Interventions*, 7(7), 768-777.

APPENDIX I

SAMPLE SOURCE CODE FOR A UDF FILE

The following source code represents a UDF file that was used to generate pulsing at the boundaries:

```
/*
*****
/*
/* User-Defined Function for Transient Flow in a Channel
/*
/* Fluent 6
/*
/* Author: Frank Kelecy
/* Date: January 2001
/*
/* This function prescribes an oscillating static pressure
/* at the channel exit.
/*
*****
#include "udf.h"

DEFINE_PROFILE(inlet_velocity,th,i)
{
    face_t f;

    double t = (CURRENT_TIME*1.111-floor(CURRENT_TIME*1.111))/1.111;

    begin_f_loop(f, th)
    {
        if(t <= 0.42)F_PROFILE(f, th, i)=0.1; else F_PROFILE(f,th,i) =
0.26*sin(1.58*3.141592654*(t+0.92));
    }
    end_f_loop(f, th)
}

DEFINE_PROFILE(outlet_pressure,th,i)
{
    face_t f;
```

```
double t = (CURRENT_TIME*1.111-floor(CURRENT_TIME*1.111))/1.111;

begin_f_loop(f, th)
{
  if(t <= 0.42)F_PROFILE(f, th, i)
=0.8*18665.13*sin(1.4*3.141592654*(0.8*t+0.1305)); else F_PROFILE(f,th,i) =(-
13400*t+22700)*0.8;
}
end_f_loop(f, th)
}
```

APPENDIX II

PLOTS OF SCALAR1 MEAN AGE

Fluent was used to simulate pulsing blood flow while tracking a user-defined scalar (Scalar1), representing the mean age of plasma, over the duration of flow. Scalar1 data for the three-dimensional source renderings were not reported, so the following plots are for the two-dimensional arterial slices. The five cases of low and five cases of high *FFR* are shown, respectively, in FIGURES A.1–5 and FIGURES A.6–10:

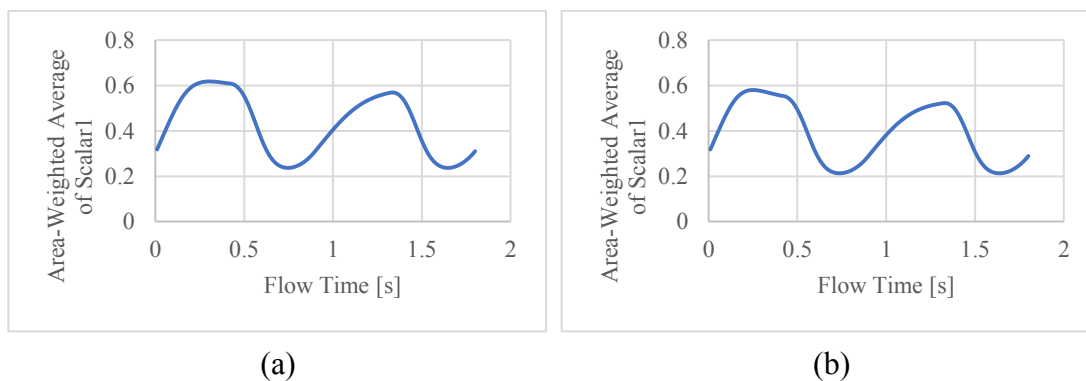


FIGURE A.1 - Area-Weighted Average of Scalar1 for (a) Slice1 and (b) Slice2 of Patient

004

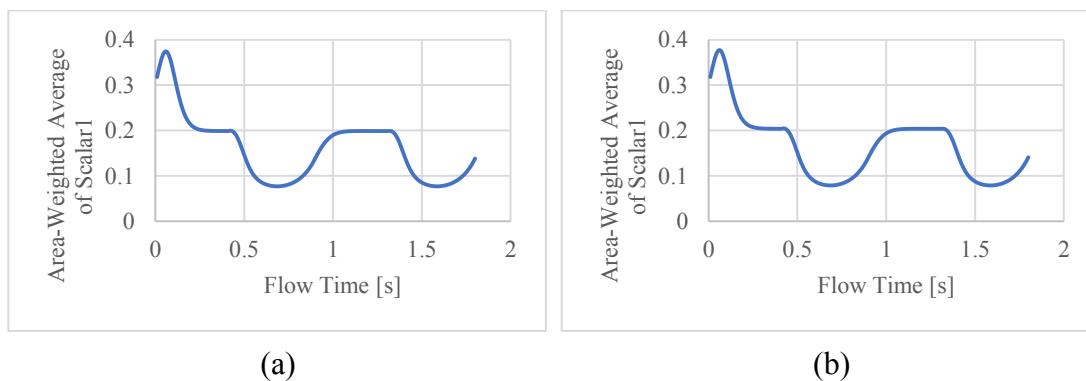
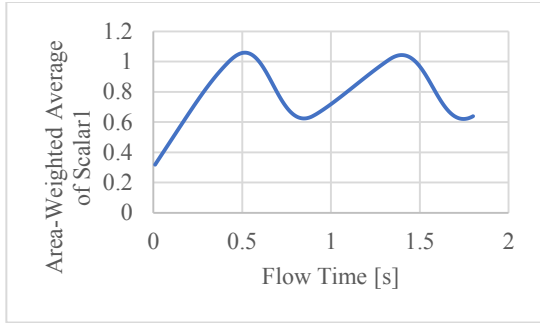
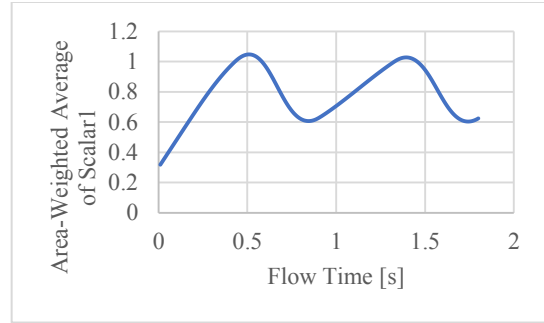


FIGURE A.2 - Area-Weighted Average of Scalar1 for (a) Slice1 and (b) Slice2 of Patient

005



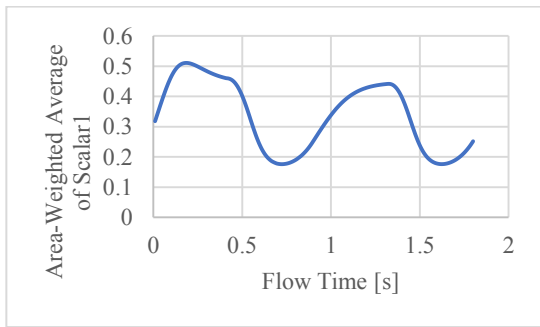
(a)



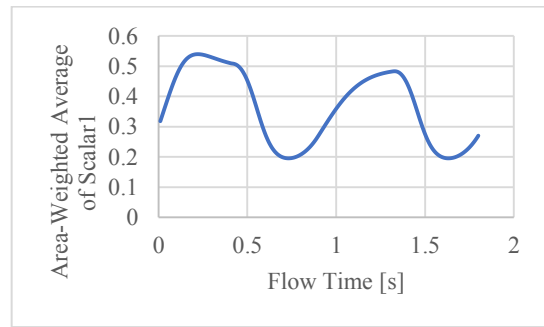
(b)

FIGURE A.3 - Area-Weighted Average of Scalar1 for (a) Slice1 and (b) Slice2 of Patient

017



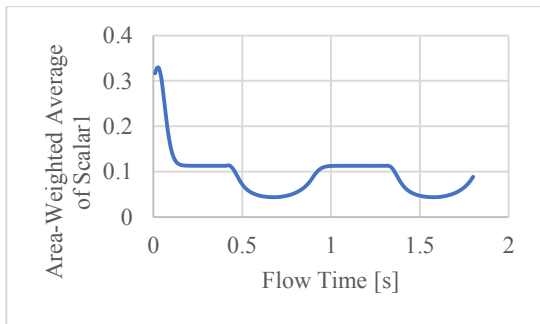
(a)



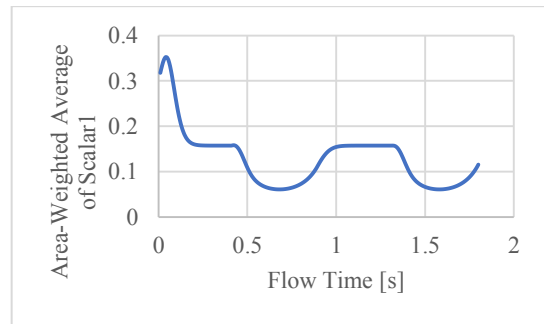
(b)

FIGURE A.4 - Area-Weighted Average of Scalar1 for (a) Slice1 and (b) Slice2 of Patient

019



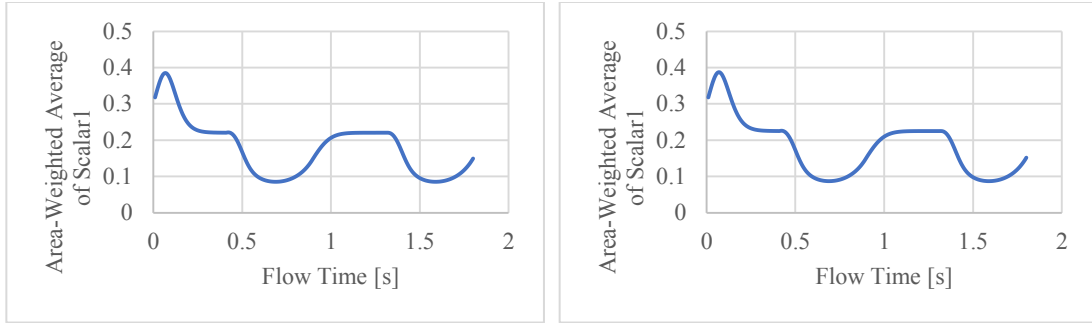
(a)



(b)

FIGURE A.5 - Area-Weighted Average of Scalar1 for (a) Slice1 and (b) Slice2 of Patient

041

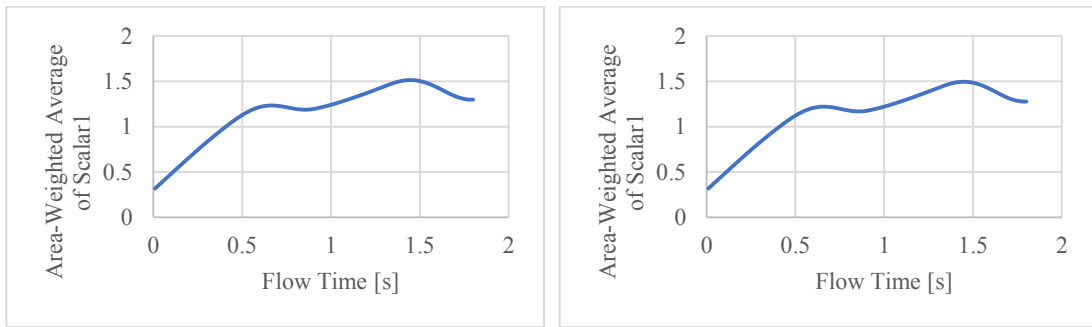


(a)

(b)

FIGURE A.6 - Area-Weighted Average of Scalar1 for (a) Slice1 and (b) Slice2 of Patient

045

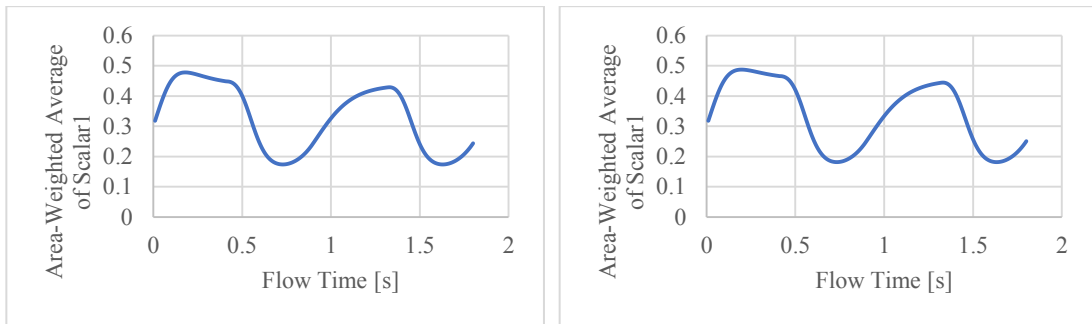


(a)

(b)

FIGURE A.7 - Area-Weighted Average of Scalar1 for (a) Slice1 and (b) Slice2 of Patient

046



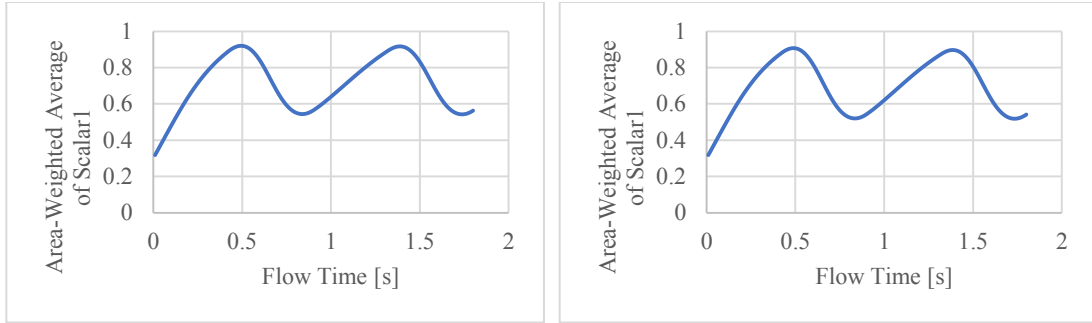
(a)

(b)

FIGURE A.8 - Area-Weighted Average of Scalar1 for (a) Slice1 and (b) Slice2 of Patient

058

117

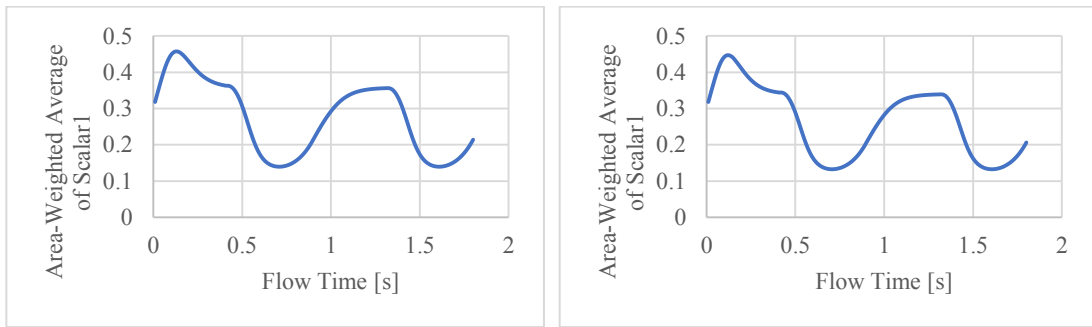


(a)

(b)

FIGURE A.9 - Area-Weighted Average of Scalar1 for (a) Slice1 and (b) Slice2 of Patient

061



(a)

(b)

FIGURE A.10 - Area-Weighted Average of Scalar1 for (a) Slice1 and (b) Slice2 of

Patient 075

VITA

Jacob Scott David Garza was born on May 5, 1995 in Pensacola, Florida. Due to family and military, he moved to Lexington, Kentucky at around age three, spent some summers in San Antonio, Texas, and later moved from Lexington to Boca Raton, Florida at around age thirteen. He moved to Louisville, Kentucky at around age sixteen and enrolled in the University of Louisville to attend the J. B. Speed School of Engineering in the fall of 2013. After completing a bachelor's degree in Chemical Engineering in the spring of 2017, he began graduate school to seek a Master of Engineering degree in Chemical Engineering. During school, he worked at Bemis Company, Inc. in Shelbyville, Kentucky, learning of polymer processing to create flexible food packaging. His interest in computational fluid dynamics, however, was sparked by Dr. Eric Berson and permitted the undertaking of its exploration.